University of Tennessee, Knoxville
TRACE: Tennessee Research and Creative Exchange

Doctoral Dissertations | Graduate School

12-2023

Characterizing the Structure and Radiation Resistance of Weberite-Type Complex Oxides

Igor M. Gussev
University of Tennessee, Knoxville, igussev@vols.utk.edu

Follow this and additional works at: https://trace.tennessee.edu/utk_graddiss

 Part of the Ceramic Materials Commons, and the Nuclear Engineering Commons

Recommended Citation

Gussev, Igor M., "Characterizing the Structure and Radiation Resistance of Weberite-Type Complex Oxides. " PhD diss., University of Tennessee, 2023.
https://trace.tennessee.edu/utk_graddiss/9181

This Dissertation is brought to you for free and open access by the Graduate School at TRACE: Tennessee Research and Creative Exchange. It has been accepted for inclusion in Doctoral Dissertations by an authorized administrator of TRACE: Tennessee Research and Creative Exchange. For more information, please contact trace@utk.edu.

To the Graduate Council:

I am submitting herewith a dissertation written by Igor M. Gussev entitled "Characterizing the Structure and Radiation Resistance of Weberite-Type Complex Oxides." I have examined the final electronic copy of this dissertation for form and content and recommend that it be accepted in partial fulfillment of the requirements for the degree of Doctor of Philosophy, with a major in Nuclear Engineering.

Maik Lang, Major Professor

We have read this dissertation and recommend its acceptance:

Gianguido Baldinozzi, Kurt Sickafus, Steven Zinkle, Christina Trautmann, Matthew Tucker

Accepted for the Council:

Dixie L. Thompson

Vice Provost and Dean of the Graduate School

(Original signatures are on file with official student records.)

Characterizing the Structure and Radiation Resistance of Weberite-Type Complex Oxides

A Dissertation Presented for the

Doctor of Philosophy

Degree

The University of Tennessee, Knoxville

Igor Maximovich Gussev

December 2023

© by Igor Maximovich Gussev, 2023

All Rights Reserved

Acknowledgments

The research described in this dissertation was carried out in collaboration with Matthew Tucker, Rodney Ewing, Michelle Everett, Joerg Neuefeind, Qiang Zhang, Antonio Fuentes, Guido Baldinozzi, Changyong Park, David Sprouster, Daniel Olds and Oliver Dicks. I thank my thesis advisor, Maik Lang, for his guidance and support. I thank my thesis co-advisor, Guido Baldinozzi, for sharing his optimism, wisdom, and support and for a research opportunity at Université Paris-Saclay, which allowed me to focus specifically on the subject of my Ph.D. I specifically thank my colleague Eric O'Quinn for his mentorship and help. I also thank my committee members, Kurt Sickafus, Steven Zinkle, Christina Trautmann, and Matthew Tucker. I have had the pleasure of working with many colleagues and I want to specifically thank Jacob Shamblin, Eric O'Quinn, Raul Palomares, Will Cureton, Jason Behrens, Jessica Bishop, Devon Drey, Roman Sherrod, Ryan Unger, Alex Solomon, John Hirtz, Patrick Huston, Irfan Ibrahim, Cale Overstreet, Cade Abbott, Mason King, Casey Corbridge, Jaccob Minnette, Evan Williams, Marshall McDonnell, Yuenpeng Zhang, Bernadette Cladek, Fuxiang Zhang, Gaëlle Vitali-Derrien, Giulio Cordaro, Francesco Delo, Bryce Mullens, Cassidy Atkinson, Kevin Co, Zhiewey Yuan, Jingue Zou, Long Cheng, Ran Xu, Milad Moazzam, Haoyuan Ma and all other wonderful colleagues at UTK and SPMS. I am forever grateful for the support and encouragement I have received from my parents, Maxim Gussev and Yelena Gusseva, and from my sister, Irina Belinskaya. Finally, I wish to express sincere gratitude to my beloved Dána, whose light has been shining through this endeavor.

Abstract

Weberite-type A_3BO_7 oxides, where A is a trivalent rare earth and B is a pentavalent element like Ta, have been a focus of research due to the discovery of the weberite-type local atomic arrangement in ceramics with a defect-fluorite structure. Earlier studies primarily examined their long-range structures, leaving gaps in understanding their short-range atomic behavior. This thesis investigates various weberite-type tantalates across all structural scales. There has been debate over the long-range structure of Y_3TaO_7, a medium-sized rare earth tantalate oxide, particularly regarding its spacegroup symmetry. This work identifies Y_3TaO_7 as an outlier, with neutron total scattering and DFT calculations indicating the $C222_1$ spacegroup as the most fitting for its structure at both local and long-range levels.

The thesis extends this structural analysis to a series of Ln_3TaO_7 weberite-type oxides. Neutron- and X-ray total scattering experiments reveal these materials' complexity and establish a link between short- and long-range order. It is found that local distortions and the averaging of local atomic domains lead to distinct structural families in weberite-type oxides. A new experimental framework is developed to systematically explore local symmetries and derive accurate local atomic models, using a novel correlated differences approach.

Additionally, the thesis explores the behavior of weberite-type oxides under swift heavy ion radiation, a previously unexamined area. It shows that while the long-range structures of weberite-type and pyrochlore oxides respond similarly to radiation, their short-range local atomic configurations differ post-irradiation, with weberite-type oxides maintaining configurations similar to their non-irradiated state.

In summary, this comprehensive study of weberite-type oxides' structures and radiation resistance emphasizes the importance of local atomic arrangements in understanding complex oxides. It demonstrates that these arrangements significantly affect amorphization resistance. The methodologies and insights gained are applicable to other materials, opening avenues for further research.

Table of Contents

List of Tables

List of Figures

Chapter 1: Introduction

1.1 Context

The availability of energy resources has transformed the course of humanity over the last few centuries. New energy sources were unlocked: fossil fuels, hydropower, nuclear, and other renewable technologies. With the growth in the human population, the energy demand has greatly increased, and to maintain the current sustainable level of energy consumption, energy production must be more efficient. This requires continuous progress in producing, harvesting, and properly distributing energy in a way that does not jeopardize our biosphere. Designing new, often highly sophisticated materials to achieve these goals is a critical component in these endeavors, and research related to energy materials has emerged as a significant field aiming to improve existing technologies and enable new applications. This research is typically interdisciplinary, using results from multiple fields and approaches to provide new insights. In the specific field of nuclear energy, much effort is related to the behavior of materials under intense irradiation within harsh environments, relevant for nuclear fuels, waste forms, and structural materials [1]–[3]. The main objective of this thesis is at the crossroads of materials synthesis, atomic-scale characterization, radiation effects testing, and simulation. Weberite-type oxides were chosen as an important class of materials and ideal model system for studying disordering across a compositional series and evaluating how structural properties such as pre-existing disorder impacts radiation behavior. To fully establish the structure-property relationship in these ceramics, it is essential to understand materials behavior across all structural length scales, from the atomic level to the mesoscale and long-range structure. Combined X-ray and neutron total scattering accompanied by pair distribution function analysis is an optimal analytical tool for this scientific problem. This dissertation will show that the disordering phenomena in weberite-type ceramics are highly

complex and proceed very differently at different structural length scales and also the radiation behavior is complex and depends on the chemical composition and pre-existing local structural distortions.

In most cases, the long-range behavior does not represent the underlying atomic-scale processes. Short-range order and mesoscale atomic arrangements play an important role in these materials and are essential to fully describe the degree of order/disorder and better understand the response to energetic ion irradiation. Comparison with other complex oxides reveals that this is a more general phenomenon of disordered/irradiated materials. A comparison to the well-studied pyrochlore oxides reveals that radiation resistance is a concept that should be expanded beyond the ability to retain crystallinity under irradiation, to include also atomic-scale processes. Further research in this field is important to design more robust energy-related materials with superior resistance to harsh environments.

1.2 Motivation, problem statement

The material system of interest for this dissertation are weberite-type structures. These compounds are part of a broad family of fluorite-related structures with a generic chemical formula A_3BO_7 (A = rare earth, B = pentavalent Ta, Nb, Sb, or others). Such materials have been the subject of intensive research over the past years [4]–[8] because of their ability to accommodate a broad range of cations as well as a large variety of distortions, which can be utilized to tailor their physical properties. However, despite this large body of work, little is known how disordering proceeds in these materials across all length scales. Furthermore, these materials have never been subject to any type of irradiation, and it remains unclear how their radiation response compares to

all other well-studied fluorite-related compounds. The fluorite structure is a very flexible system that shows an outstanding ability to accommodate many types of superstructures and derivatives some of which show exceptional radiation resistance [9]. For example, anion-deficient fluorite-related oxide structures, such as A_3BO_7 weberite-type, $A_2B_2O_7$ weberite, and $A_2B_2O_7$ pyrochlore, maintain closed-packed cation layers as in the parent fluorite structure AO_2. Anion deficiency enables charge compensation and an extended selection of *A*-site and *B*-site cations that yields a range of ordered and disordered phases. As a result, fluorite-related structures are ideal model systems to improve our understanding of structural disorder and establish structure-property relationships particularly with respect to ion irradiation. The choice of A and B cations can control the pre-existing distortions and disorder in these materials, which greatly impacts their radiation response. For example, in the case of well-studied $A_2B_2O_7$ pyrochlore oxides, ordered $Gd_2Ti_2O_7$ pyrochlore is susceptible to ion beam-induced amorphization, while disordered $Gd_2Zr_2O_7$ pyrochlore has superior resistance to amorphization [10], [11]. Previous work has shown that size of both cations and the associated antisite defect energy plays an important role in this response besides other factors [4], [7], [12] . These processes are not yet fully understood, and previous research revealed that atomic-scale processes must be considered. This dissertation focuses on a comprehensive structural analysis of weberite-type oxides across all structural length scales. The aim is to establish a detailed description of how the structure is changing with chemical composition and how the degree of underlying disorder affects the behavior under energetic ion irradiation.

The choice of weberite-type oxides for this thesis is mainly motivated by recent discoveries of a local weberite-type atomic arrangement in the well-studied $A_2B_2O_7$ pyrochlore oxides [13]–[17]. Neutron total scattering revealed that the atomic-scale pyrochlore arrangement changes to a

weberite-type configuration after energetic ion irradiation, independently of whether the long-range structure was lost (amorphization) or modified to a disordered, defect-fluorite structure [13], [18], [19]. This local atomic arrangement was not only observed in irradiated pyrochlore oxides, but also in those that were disordered through synthesis with similar A- and B-site cations (chemical-induced disorder) or after processing with high energy ball milling. This behavior was explained by a set of fundamental chemical rules that require some degree of order at the atomic scale, even if a material was exposed to harsh environments and is fully disordered across the long-range structure [14]. Since weberite-type structural building blocks are observed in irradiated pyrochlores, this could imply that weberite-type oxides might exhibit improved resistance under similar irradiation conditions. However, until now, these materials have never been studied under any type of irradiation.

Recent research on chemically disordered $A_3^{3+}B^{5+}O_7$ weberite-type oxides demonstrated that despite the loss of respective long-range weberite-type order and the formation of a disordered A_3BO_7 defect-fluorite structure, the local atomic configuration cannot maintain mixed atomic sites and adopts a higher-symmetry orthorhombic structure [20]. This large degree of structural heterogeneity in weberite-type oxides is similar to what is observed in the structurally-related pyrochlore oxides [13], [15], [16], [18]. Thus, the same rigorous multi-scale analysis is required with high sensitivity to both cation and anion sublattices.

1.3 Scientific methodology

Condensed matter scientists try to understand how combinations of billions of electrons and nuclei yield certain physical properties. The fundamental challenge is understanding and

explaining the new phenomena resulting from interactions created by ensembles of particles and extracting functions that measure the observed patterns in space and time, to be used to compare experiment and theory. In general, scattering experiments measure correlation functions in a system. X-ray scattering can measure the electron density correlation function, while neutron scattering can measure nuclei correlation functions. Elastic scattering gives equal-time correlation functions, while inelastic scattering gives access to time-dependent correlation functions. Crystallography based on X-ray diffraction technique has been quite successful in describing the long-range structures in minerals, synthetic crystals, and organic compounds. With this approach, any kind of crystal imperfections (defects, disorder, lattice vibrations, etc.) perturb the long-range ordered structure and reduces the intensity of the reciprocal lattice of Bragg reflections. However, this intensity loss at the regular reciprocal lattice positions is recovered in the form of a weak and broad diffuse signal spread over the reciprocal space. In conventional long-range characterization, this diffuse scattering is treated as background and is not subject of further analysis by, for example, Rietveld refinement. In this dissertation, special attention is given to diffuse signal to build structural models for the atomic organization of material systems and to address the crucial question of how local correlations propagate, how the introduction of defects and disorder affects the long-range order and impacts material properties such as radiation resistance.

While X-ray diffraction is a potent technique for studying materials, radiation consisting of neutron beams also stands as an immensely valuable tool in materials research. Neutrons offer significant structural insights, often complementing the information obtained from X-rays. Neutrons interact primarily with atomic nuclei, enabling them to differentiate between low- and high-Z elements such as oxygen and lanthanides. This unique property of neutrons renders them highly sensitive to the ordering of oxygen vacancies, a pivotal piece of information for the

materials under investigation in this dissertation and of critical significance for controlling the material's performance.

1.4 Organization of the thesis

The literature review, background information on the weberite and the weberite type structures are contained in **Chapter 2**. This chapter describes the structural relations between fluorite-derived weberite-like structures and provides a historical overview of methods and approaches used to describe topologically related complex oxides. Experimental methods and necessary instrumentation information for subsequent chapters are provided in **Chapter 3**. **Chapter 4** details the structural characterization of the rare-earth 'precursor' Y_3TaO_7, probably the most studied tantalate compound with a weberite-type structure. The structural characterization was performed using neutron total scattering technique and corroborated by first-principle (DFT) calculations. This published research solved the discrepancy previously reported for this compound in the literature. **Chapter 5** describes a systematic study of a broad compositional series of Ln_3TaO_7 (Ln = Pr, Dy, Tb, Ho, Tm, Yb) weberite-type oxides. Complementary X-ray diffraction and neutron total scattering techniques provided a fundamental understanding of the relations between local atomic and average structural length scales and describe in detail order/disorder phenomena in these weberite-type tantalates. This study also presents a hierarchical method to derive a variety of structural variants from the Brillouin zone to provide necessary localized atomic configurations. A new generalized correlated reliability factor approach (*Gs*) was developed and used with the standard reliability factor (*Rw*) to improve validity tests of local atomic configurations and to determine the most appropriate structural model. These optimized models were then used to quantify local distortions across the compositional series, which are essential to explain the

structural behavior and disordering across all correlation lengths. **Chapter 6** summarizes the research related to the structural response of weberite-type oxides to swift heavy ion irradiation. Ion-beam experiments coupled with X-ray diffraction characterization were used to test the amorphization resistance of weberite-type oxides and its dependence on the A-site (Ln = Pr, Dy, Tb, Y, Yb) and B-site (B = Ta, Nb, Sb) cation substitutions with pyrochlore oxides being used as a benchmark to compare and contrast the results obtained for weberite-type materials. An in-depth analysis using neutron total scattering on a few selected irradiated compounds provided insight into local-, intermediate- and long-range structural responses and revealed that these materials have an exceptional resistance at the atomic level. A general summary of the dissertation and a perspective for future work in areas relevant to this research are covered in **Chapter 7**. Appendix A is at the end of this dissertation and summarizes research not directly related to weberite-type oxides.

1.5 Scientific contributions to the research field

All publications that resulted from undergraduate and graduate work in the Nuclear Engineering Department at The University of Tennessee, Knoxville, and in the Laboratoire Structures, Propriétés et Modélisation des Solides at Centralesupélec, Université Paris-Saclay are listed below.

1. Igor M. Gussev, Eric C. O'Quinn, Matthew Tucker, Rodney C. Ewing, Cale Overstreet, Jörg Neuefeind, Michelle Everett, Qiang Zhang, David Sprouster, Daniel Olds, Gianguido Baldinozzi, Maik Lang. *Systematic study of short- and long-range correlations in RE3TaO7 weberite-type compounds by neutron total scattering and X-ray diffraction.* J Mater Chem A. (2023).

2. Igor M. Gussev, Eric. C. O'Quinn, Mason King, Jörg Neuefeind, Michelle Everett, David Sprouster, Frieder Koch, Gianguido Baldinozzi, Maik Lang, *probing the long- and short-*

range ion-irradiation response of Ln_3BO_7 (B = Ta, Nb, Sb) weberite-type oxides by synchrotron X-ray diffraction and neutron total scattering. (2023, in preparation).

3. Oliver A. Dicks, Igor M. Gussev, Xiaonan Lu, Maik Lang, Kostya Trachenko, *The structure of aluminaborosilicate glasses for nuclear waste encapsulation characterised by neutron diffraction, reverse Monte Carlo and molecular dynamics methods.* (2023, in preparation).

4. Igor M. Gussev, Maik Lang, Gianguido Baldinozzi, *Using correlated residuals to discriminate structural organisation models in real-space refinements.* (2023, in preparation)

5. Alexandre P. Solomon, Eric C. O'Quinn, Gianguido Baldinozzi, Juejing Liu, Igor M. Gussev, Xiaofeng Guo, Joerg Neuefeind, Christina Trautmann, Maik K. Lang. *Atomic-Scale Structure of ZrO2: New Insight into Metastability* (2023, in preparation)

6. John Hirtz, Eric. C. O'Quinn, Igor M. Gussev, Joerg Neuefeind, and Maik Lang, "*Cation Short-Range Ordering of MgAl2O4 and NiAl2O4 Spinel Oxides at High Temperatures via in Situ Neutron Total Scattering*," *Inorg. Chem.*, vol. 61, no. 42, pp. 16822–16830 (2022).

7. Sherrod, Roman, O'Quinn, Eric C., Neuefeind, Joerg, Gussev, Igor M. & Lang, Maik *Comparison of Short-Range Order in Irradiated Dysprosium Titanates*. *npj Mater. Degrad.* 1–7 (2021).

8. Xiaonan Lu, Joelle T. Reiser, Benjamin Parruzot, Lu Deng, Igor M. Gussev, Jörg Neuefeind, Trent R. Graham, Hongshen Liu, Joseph V. Ryan, Seong H. Kim, Nancy Washton, Maik Lang, Jincheng Du, John D. Vienna, *Effects of Al:Si and (Al+Na):Si Ratios on the Properties of the International Simple Glass, Part II: Structural Properties. J. Am. Ceram. Soc.* 104, 183–207 (2021).

9. Maik Lang, Alexandra Navrotsky, Joseph Ryan, Jarrod Crum, Igor Gussev, *et al.*, "*Project 17-13125: The Thermodynamics of Crystallization and Phase-Separation in Melt-Derived Nuclear Waste Forms (Technical report)*, pp. 1–161, (2021).

10. Igor M. Gussev, Eric C. O'Quinn, Gianguido Baldinozzi, Jörg Neuefeind, Rodney C. Ewing, Fuxiang Zhang, Maik Lang, *Local order of orthorhombic weberite-type Y3TaO7 as determined by neutron total scattering and density functional theory calculations.* Acta Mater. (2020).

11. Drey, Devon L., O'Quinn, Eric C., Subramani, Tamilarasan, Lilova, Kristina, Baldinozzi, Gianguido, Gussev, Igor M., Fuentes, Antonio F., Neuefeind, Joerg C., Everett, Michelle, Sprouster, David, Navrotsky, Alexandra, Ewing, Rodney C., Lang, Maik. *Disorder in Ho2Ti2−xZrxO7: pyrochlore to defect fluorite solid solution series*. *RSC Adv.* 10, 34632–34650 (2020).

12. Chung, C.K., Shamblin, J., O'Quinn, E. C., Shelyug, A., Gussev, I., Lang, M., *Navrotsky, A., Thermodynamic and Structural Evolution of Dy2Ti2O7 Pyrochlore after Swift Heavy Ion Irradiation.* Acta Mater. 145:1–26 (2018).

13. E.C. O'Quinn, J. Shamblin, B. Perlov, R.C. Ewing, J. Neuefeind, M. Feygenson, I. Gussev, M. Lang, *Inversion in Mg1– x Nix Al2O4 Spinel: New Insight into Local Structure*, J. Am. Chem. Soc. 139, 10395–10402 (2017).

Chapter 2: Literature Review

2.1 Fluorite structure

Since multiple complex oxide structures will show a close relation to fluorite structure, the general aspects of fluorite and fluorite-derived structures need to be assessed and contextualized. Many materials adopt or are derived from cubic fluorite structure which is isomorphic with fluorite mineral $Ca^{2+}F^{1-}{}_2$. This specific material can be viewed as two interpenetrating sublattices: a cation sublattice consisting of Ca cations occupying close-packed face-centered cubic sites and an anion sublattice in which F anions occupy primitive cubic sites (**Figure 2.1**). These two sublattices form a three-dimensional checkerboard pattern. The fluorite structure can be described by a cubic lattice with two Wyckoff sites (one cation and one anion), described by *Fm-3m* (225) space group with approximately 5.5 Å unit cell dimension. As only two Wyckoff sites are occupied, the polyhedra arrangement is quite simple, with Ca cations occupying centers of CaF_8 cubes. Respectively, each F anion is located at the center of the cationic tetrahedra (Ca_4F). In a similar fashion, the fluorite oxides have an $A^{4+}O^{2-}{}_2$ (sometimes denoted as $A^{4+}{}_4O^{2-}{}_8$) general formula with otherwise identical structure to CaF_2 fluorite: a face-centered cubic cation sublattice and primitive cubic anion sublattice.

The fluorite-derived complex oxides are a broad general term to describe the plethora of structures derived from cubic fluorite by introducing at least two cations, A and B in place of the original fluorite A site. Typically, these cations have different valence states; thus, the oxygen sublattice' occupancy is adjusted according to stoichiometry, and the respective fraction of oxygen vacancy is introduced into previously full oxygen sites, resulting in $A_{4-x}B_xO_{8-y}$ stoichiometry. Certain combinations of cations with certain cation size ratios and charge differences dictate specific topological cation ordering, resulting in different fluorite-derived complex oxides, with

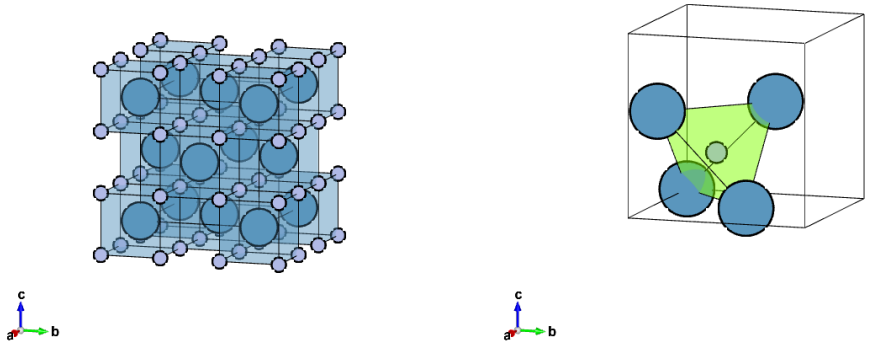

Figure 2.1: (Left) CaF_2 with Fm-3m structure. Light blue spheres are Ca cations, while light purple spheres are F anions. Light blue cubes designate CaF_8 polyhedra. (Right): Ca_4F cationic tetrahedra, shown in the light green shade, black lines designate the cubic unit cell. Ca cations shown are located at the edge and three faces of the cubic unit cell.

their names typically denoting respective stoichiometry and choice of cations, while 1 out of 8 oxygen sites are vacant (O'), yielding $A_{4-x}B_xO_7O'$ stoichiometry. Among the most studied fluorite-derived structures are so-called 3:1:7 or 2:2:7 complex oxides with different respective structures, such as weberite oxides ($A_2B_2O_7$, for example, $Sr_2^{2+}Sb_2^{5+}O_7$), weberite-derivatives called weberite-type oxides (A_3BO_7, for example, $La_3^{3+}Ta^{5+}O_7$ or $Y_3^{3+}Ta^{5+}O_7$) and pyrochlore oxides ($A_2B_2O_7$, for example, $Ho_2^{3+}Ti_2^{4+}O_7$). In case when A and B cations are not significantly different or material undergoes a peculiar synthesis route or environmental exposure that cannot favor a specific topological cation ordering, the so-called defect-fluorite structure can form. Although represented by the same *Fm-3m* space group as regular fluorite, the name implies the random stochiometric occupancy of cations (2:2 or 3:1) and random distributions of 1/8 of oxygen vacancies onto anion sublattice (**Figure 2.2**). Despite the occurrence, the position of oxygen vacancy and specific cation ordering are two crucial components to distinguish different types of complex oxides.

2.2 Weberite structure

Weberite and weberite-type (sometimes called weberite-like) complex oxides are particular class of ceramics owing their name to Theobald Weber who discovered the weberite mineral in Greenland in 1938. In 1944, its crystal structure was determined by Byström [21], who established its structural similarities to the cubic fluorite [9]. The chemical formula of the weberite mineral is Na_2MgAlF_7 while its structure was determined to be *Imma* (74) space group, containing four formula units per unit cell [22]. Analogously weberites are materials isomorphic with the mineral with two major classes of weberites structures: the fluorite weberites ($A_2^{1+}B^{2+}B^{3+}F_7^{1-}$) which have been studied extensively due to their interesting magnetic properties [23] and oxide

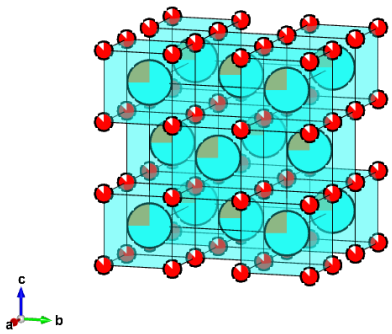

Figure 2.2: A_3BO_7 defect-fluorite structure (*Fm-3m)*. A-site is randomly occupied by two cations in a 3:1 ratio, both shown as larger cyan and brown spheres. The small red/white spheres are oxygen sites, with white segments inside the spheres denoting 7/8 occupancy of the site, i.e., 1/8 of sites being vacant.

weberites ($A_2^{2+}B_2^{5+}O_7^{2-}$ and $A_2^{1+}B_2^{6+}O_7^{2-}$) which have been mainly studied because of their physical properties, such as ferroelectric, dielectric and magnetic properties, photocatalyst splitters, solid fuel cell electrolytes [5], [24]–[29]. In addition, weberite-derived oxides attract attention as host matrices for rare-earth lanthanide ions with luminescent features for technological applications, such as photonic devices, solar cells, and others [8], [30] as well as attractive materials for thermal barrier applications, in particular, high entropy oxides [31], [32]. In general, the weberite and weberite-derived structures are extremely flexible, allowing the adoption of cations with a wide range of oxidation states (from monovalent A^{1+} to hexavalent B^{6+}) and ionic sizes and different anion types (O^{2-} and F^{1-}). These structures adopt multiple cation environments (typically, 6-, 8- or 6-, 7-, 8- coordinated cations) with different stacking motifs and sequences of cation chains.

As was mentioned before, the charge differences and ionic radii of A^{2+} and B^{5+} cations dictate the ordering of cations and anions at specific crystallographic sites in the classical *Imma* weberites. For example, in the weberite structure ($Ca_2Sb_2O_7$, *Imma*), A-site cations (Ca^{2+}) occupy 4d and 4a Wykoff sites (**Figure 2.3**), while B-site cations (Sb^{5+}) occupy 4c and 4b sites. The classical *Imma* weberite structure consists of repeated layers of polyhedra, forming alternating close-packed A_3B and AB_3 Kagome layers parallel to (011) (**Figure 2.4**). Hence, the fundamental unit of weberite is a combination of one A_3B layer and one AB_3 layer, arranged orthorhombically, known as 2*O* weberite. The notation 2*O* signifies two slabs in the unit cell, and "*O*" represents the crystal system (orthorhombic). Oxygen anions occupy 8h, 16j, and 4e Wykoff sites and participate in the formation of CaO_8 distorted cubes and SbO_6 octahedra. (**Table 2.1**). Due to its structural flexibility and ability to accommodate different valence states for cations and anions, the classical weberite structure allows for a wide range of structural alterations. These alterations result in

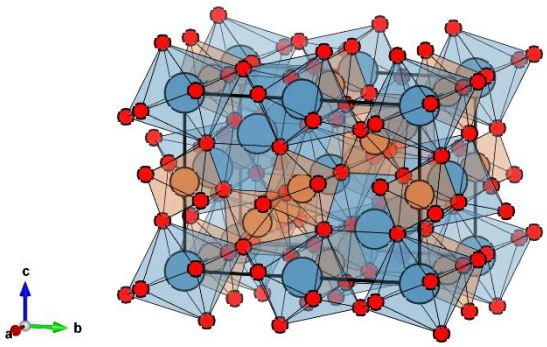

Figure 2.3: $Ca_2Sb_2O_7$ weberite with *Imma* structure. Light blue spheres are Ca cations; brown spheres are Sb cations. Small red spheres are oxygen. A solid black line denotes the respective unit cell.

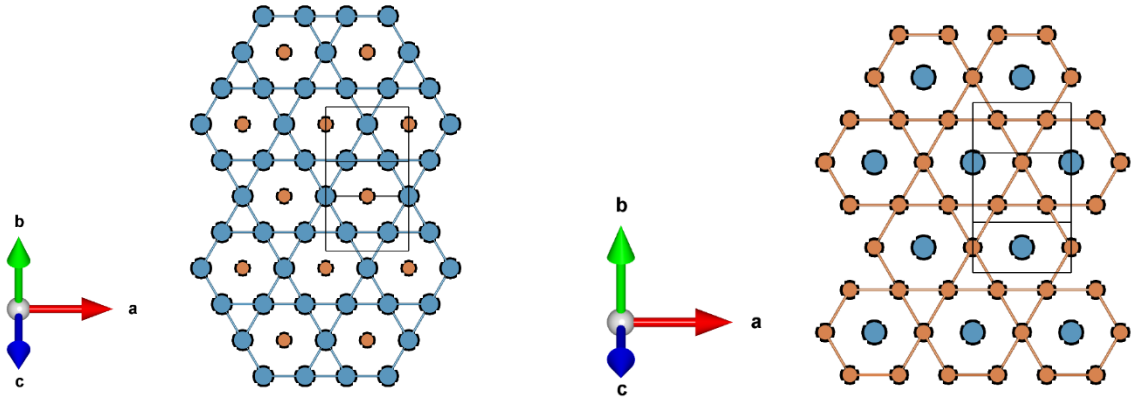

Figure 2.4: (Left) A_3B and (right) AB_3 Kagome layers within $Ca_2Sb_2O_7$ weberite. Light blue spheres are Ca cations, brown spheres are Sb cations. Solid black lines denote respective unit cells.

Table 2.1: Structural information of $Ca_2Sb_2O_7$ *Imma* (74) weberite.

$Ca_2Sb_2O_7$		**a (Å)**	**b (Å)**	**c (Å)**
Imma		7.3015	10.2337	7.4552
Atom	**Wyckoff Site**	**x**	**y**	**z**
Ca1	4d	0.25	0.25	0.75
Ca2	4a	0	0	0
Sb1	4c	0.25	0.25	0.25
Sb2	4b	0	0	0.5
O1	8h	0	0.4063	0.7261
O2	16j	0.2928	0.6171	0.9342
O3	4e	0	0.25	0.1529

significant variations in crystallographic definition, leading to the classification of different weberite oxides, such as 2*M*, 3*T*, 4*M*, 5*M*, 6*M*, 7*T*, 7*M*, and 8*O* Weberite [9], where letter represents the crystal system and the number represents the number of cation layers.

There's an alternative option to view the structure as connected cation chains forming two-dimensional slabs parallel to [100] axis. In the first layer, octahedral chains occupied by B-cations (with coordination number 6) alternate with distorted cubes occupied by A-cations (with coordination number 8), in the [100] direction. (**Figure 2.5**) The second layer consists of alternating octahedra occupied by B-cations and distorted cubes occupied by A-cations. This three-dimensional octahedral network is a key feature of the weberite structure. The first octahedra, located at the 4c Wykoff site, are corner-shared to each other and form octahedral chains parallel to the Ca chains in the [100] direction. At the same time, the 4b Sb octahedra are isolated from each by Ca distorted cubes and linked to the 4c Sb octahedra from other layers to form a three-dimensional octahedral network.

The positioning of anions is affected by the stacking of the cation network. As was mentioned previously, in an ideal fluorite structure, each anion sits at the center of undistorted cationic tetrahedra. As cationic charge differences are introduced in A and B cations, the anion sites are displaced to consider the charge balance. In weberite oxides, A and B cations' arrangement leads to the formation of different cationic tetrahedra: A_3B, A_2B_2, and AB_3. In a formula unit of weberites, there are two A_3B, four A_2B_2, and two A_3B cationic tetrahedra (**Figures 2.6** and **2.7**). Unlike fluorites, not all anions are located inside cationic tetrahedra. For example, in $Ca_2Sb_2O_7$, O1 and O2 are located inside Ca_3Sb and Ca_2Sb_2 tetrahedra. They are displaced compared to the ideal position of fluorite tetrahedra, while O3 is located outside $CaSb_3$ cationic tetrahedra due to a larger charge imbalance between A and B sites (**Figure 2.7**). Instead, the $CaSb_3$ cationic tetrahedra

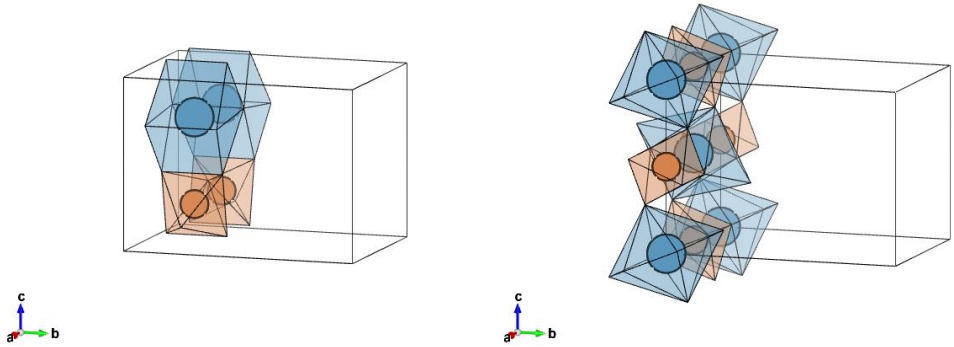

Figure 2.5: (Left): The first CaO_8-SbO_6 layer of weberite structure. SbO_6 and CaO_8 polyhedra forming chains along [100] are visible. (Right): Alternating CaO_8-SbO_6 layer of $Ca_2Sb_2O_7$ weberite with *Imma* structure. In both figures, Light blue spheres are Ca cations, brown spheres are Sb cations. In respective shades are 8-coordinated distorted cubes and 6-coordinated octahedra. Oxygen atoms are not shown.

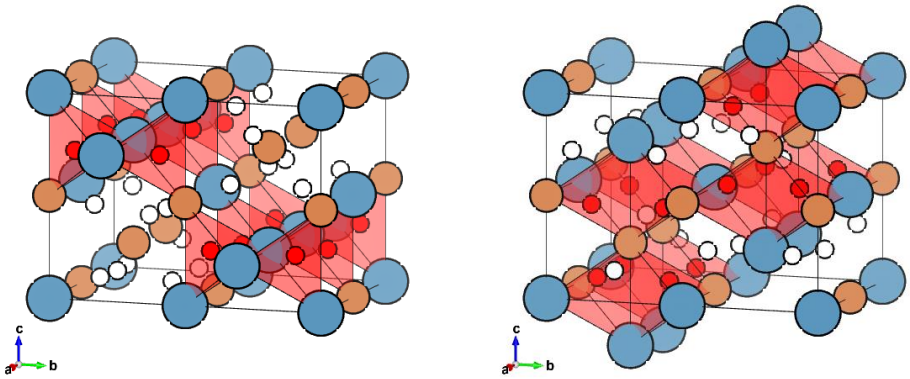

Figure 2.6: (Left): Ca_3Sb cationic tetrahedra. Light blue and brown spheres are Ca and Sb cations, respectively. Small red spheres are O1 anions inside Ca_3Sb tetrahedra (shown in the red shade). Small white spheres are the weberite structure's remaining O2 and O3 anions. (Right): Ca_2Sb_2 cationic tetrahedra. Light blue and brown spheres are Ca and Sb cations, respectively. Small red spheres are O2 anions located inside Ca_2Sb_2 tetrahedra (shown in red shade). Small white spheres are the weberite structure's remaining O1 and O3 anions.

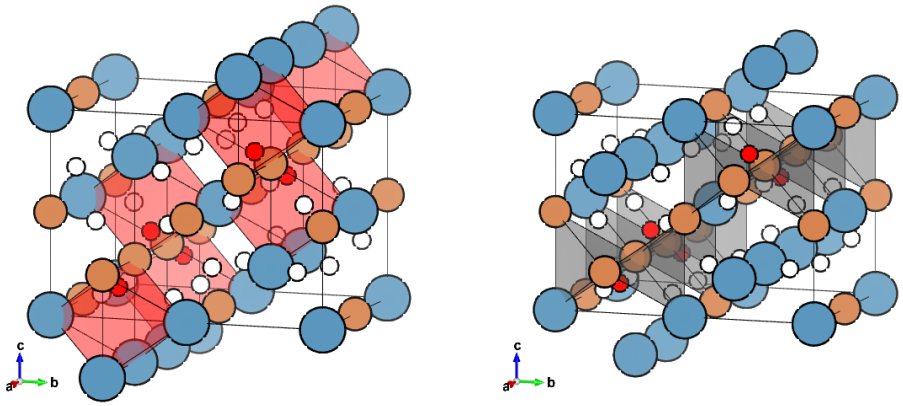

Figure 2.7: (Left): Ca_4Sb_4 cationic octahedra. Light blue and brown spheres are Ca and Sb cations, respectively. Small red spheres are O3 anions inside Ca_4Sb_4 octahedra (shown in red). (Right): Representation of O3 cationic environment using vacancy site. The vacancy is located inside the Ca_3Sb tetrahedra (shown in the grey shade), while the O3 anion is located outside of the tetrahedra and displaced towards the Sb-Sb face of the tetrahedra. The weberite structure's remaining O1 and O2 anions are small white spheres in both images.

are occupied by a vacancy. Alternatively, this arrangement can be imagined as O3 being located inside Ca_4Sb_4. This oversaturated $CaSb_3$ cationic tetrahedra that cannot accommodate the O3 cation leads to some peculiar findings, as $Ca_2Sb_2O_7$ can form a metastable pyrochlore phase [33], in which the motif of A and B cations is different while cation coordination environments are same, but O3 is located inside the cationic tetrahedra. This arrangement irreversibly transforms into a weberite structure upon heating, which can be avoided by substituting F^{1-} anions instead of O^{2-}, for example, $Ca_{1.56}Sb_2O_{6.37}F_{0.44}$ pyrochlore is stable, or by using a combination of monovalent cation (Na^{1+}) and F^{1-} anion, such as in $CaNaSb_2O_6F$ [34], [35].

2.3 Weberite-type structure

The weberite structure can form many polytypes characterized by the same layers of cations but with a different number of slabs in a unit cell and, thus, a different crystal system. Typical weberite is a structure described by an orthorhombic I-centered lattice. The I-centering can be altered by chemically substituting specific cations, such as Cu^{2+} [9], or by introducing two B-site cations, in which the B-2 ion is significantly larger than the B-1 ion, disturbing the three-dimensional octahedral network. This extreme case is a so-called weberite-type structure (sometimes referred to as weberite-like structure), with A_3BO_7 stoichiometry, where A is trivalent rare-earth $RE^{3+,}$ and B is pentavalent (Ta^{5+}, Nb^{5+}, Sb^{5+}, Os^{5+}, Re^{5+}, Ru^{5+}, Mo^{5+}, Ir^{5+}) [5]. In this case, B-2 ions (previously 6-coordinated in *Imma*) are the same as A-ions (previously 8-coordinated in *Imma*) and instead form a 7-coordinated highly distorted cube, and only B-1 ions, 6-coordinated in *Imma* and new structure remain (**Figure 2.8**). The weberite-type structure has an arrangement of BO_6-AO_8 layers, formed by chains of octahedra and distorted cubes, similar to weberite oxides, but the adjacent layer is formed by AO_7-AO_7 layers instead. The name 'weberite-type' results from the

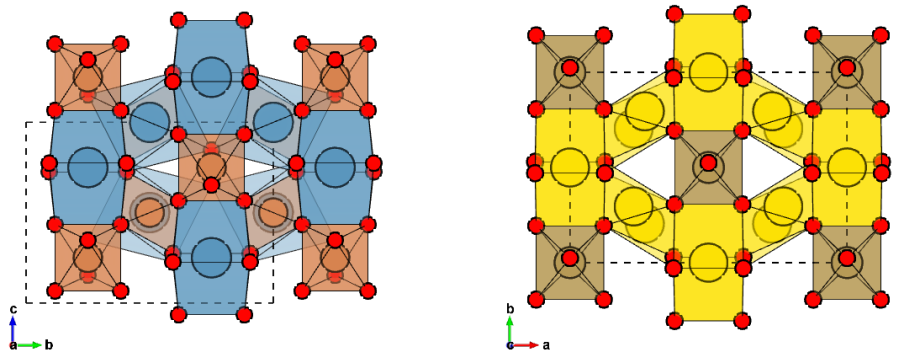

Figure 2.8: (Left): Schematic representation of $Ca_2Sb_2O_7$ *Imma* weberite structure shown parallel to (011). Bigger light blue and brown spheres are Ca^{2+} and Sb^{5+} cations, while small red spheres are oxygen anions. The dashed black lines are individual unit cells. The structure is shifted for ease of visualization. (Right): Schematic representation of Ln_3TaO_7 *Cmcm* weberite-type structure. Bigger yellow and brown spheres are Ln^{3+} and Ta^{5+} cations. Small red spheres are O anions.

structure not maintaining the three-dimensional BO_6 octahedral network (as half of B cations are replaced with A) as in weberite but still having a similar arrangement of BO_6-AO_8 layers. Historically, weberite-type oxides have been reported as La_3NbO_7-type structures, although they possess many different orthorhombic structures, typically C- or P-centered [28], [36], [37]. Common structural trends are emerging in ordered weberite-type oxides: 6-coordinated B-site cations form rigid TaO6 octahedra while A-site cations are placed in two distinct polyhedra: AO_8 and AO_7 distorted cubes, where in the latter, one of the oxygen anions is replaced with a vacancy. BO_6 polyhedra share two corners and form chains projected along [001], while AO_8 distorted cubes share edges and form chains along [001]. These two parallel chains form a layer parallel to the (100) plane. AO_7 cubes also form chains parallel to [001] and form a second layer in between layers of BO_6 and AO_8. (**Figure 2.9**). The weberite-type structures are characterized by the direction of the tilt of BO_6 octahedra and ionic radii of cations which constrain the c-lattice parameter. These impose geometrical constraints on other polyhedra, resulting in distortions in most weberite-type compounds. The magnitudes of these distortions are determined by the respective ionic radii of A- and B-site cations as well as by electronegativity and polarizability of cations [28], [36]. This explains why there are several structural families of weberite-type oxides with a plethora of spacegroups proposed: the structural motifs are similar, while the specific details, such as tilts and distortions of polyhedra chains, the specific positions of oxygen and vacancy sites as well as atomic-level distortions might be more intricate.

Allpress et al. conducted a comprehensive study using X-ray diffraction and selected-area electron diffraction (SAED) experiments[5], [36], [38], [39], and proposed three distinct structure types for weberite-type oxides with varying chemical compositions. The final symmetry of these structures was found to be influenced by the size of the A-site lanthanide cation, as trivalent lanthanides

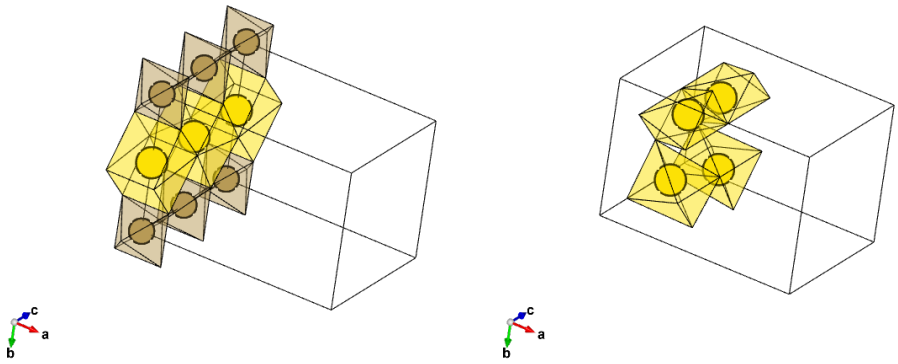

Figure 2.9: (Left): TaO_6-LnO_6 layer or Ln_3TaO_7 weberite-type with *Cmcm* structure. TaO_6 and LnO_8 chains along [001] are visible. (Right): The second LnO_7-LnO_7 layer of the weberite-type structure. In both figures, yellow spheres are Ln cations, and brown spheres are Ta cations. In respective brown and yellow shades are 6-coordinated octahedra and 7- and 8-coordinated distorted cubes. Oxygen atoms are not shown.

show a monotonic contraction of the ionic radius with increasing atomic number.

X-ray diffraction experiments, sometimes aided by SAED, were utilized to assign the *Cmcm* space group (63) to tantalate compounds with larger lanthanides (e.g., La_3TaO_7, La_3NbO_7, La_3SbO_7, and Nd_3NbO_7), *C222₁* (20) to lanthanides with intermediate-sized ionic radius (e.g., Gd_3TaO_7, Gd_3NbO_7, and Ho_3TaO_7), and *Fm-3m* (225) to compounds with smaller lanthanide cations (e.g., Er_3NbO_7 and Er_3TaO_7). In the latter case of the smaller lanthanide compounds, no supercell diffraction maxima are observed, and their diffraction patterns correspond to a disordered structure resembling defect-fluorite, with randomly distributed anion vacancies and random cation occupancy across the available sites [36].

Moreover, the weberite-type oxides between different structure types at phase boundaries can exhibit distinct structures depending on the thermal history and temperature conditions during data collection [5]. For instance, Wakeshima et al. reported that compounds with intermediate-sized cations, such as Ho_3TaO_7, exhibit *C222₁* symmetry after prolonged annealing at 1673 K or *Fm-3m* symmetry after annealing at 1973 K [5]. Similarly, Nd_3TaO_7 displays two polymorphs at room temperature, a mixture of *Cmcm* and *C222₁* phases, which transform into a single *C222₁* phase at higher temperatures [5], [36]. Interestingly, these phase transitions, belonging to either first- or second-order phase transitions, can also be induced by cooling down the weberite-type oxides to cryogenic temperatures, which in turn can induce changes in magnetic or other properties [40], [41]. Following these seminal studies, other research groups have investigated the structures of several weberite-type oxides, mostly categorized under the initially assigned *C222₁* space group (intermediate-sized lanthanides, e.g., Sm_3TaO_7 – Ho_3TaO_7 and Y_3TaO_7), although alternative structural models have been proposed at times [39]. The motivation for this reassessment arose from previously unnoticed weak diffraction maxima, which were difficult to detect in XRD

patterns obtained from laboratory diffractometers but did not conform to the selection rules of the $C222_1$ symmetry. Different space groups with mutually incompatible selection rules, such as Cmcm (or an alternative *Ccmm*, 63), $C222_1$ (20), *Cmmm* (65), *Amm2* (38), *Cmm2* (35), and *C222* (21), were suggested for some of these compounds [5], [36], [38], [39]. The multitude of proposed space groups can be attributed to the significant uncertainties in refinements due to weak and overlapping peaks in the powder diffraction data.

Although the weberite-type structure is complex, it is constrained by the orthorhombic c-lattice parameter, which depends on the size and tilt of the octahedra. This, in turn, imposes geometric constraints on the other polyhedra, resulting in distortions in most weberite-type compounds. All the structural models proposed in the literature for orthorhombic weberite-type compounds exhibit the same polyhedra arrangements with specific distortions, differing mainly in the orientation of the tilt axis of the BO_6 octahedra. The *Cmcm* structures have a [010] tilt system, while the *Ccmm* (or $C222_1$) structures have a [100] tilt system. This allocation of tilt systems and resulting spacegroups also allies to other weberite-type oxides, for example, weberite-type oxides based on Nb^{5+} show a similar number of structural families, [42], [42]–[44] with *Pnma* spacegroup allocation replacing the centrosymmetric *Cmcm* of large lanthanides.

In weberite-type tantalate oxides, the difference in charge between the two cations (Ln^{+3} and Ta^{+5}) can promote long-range order, with both cations and anions occupying specific crystallographic sites. This defines a unique bonding environment resulting in a repeating configuration of four coordination polyhedra: (i) an octahedron formed by the pentavalent Ta cation, (ii) and (iii) two sevenfold-coordinated polyhedra occupied by the rare-earth or lanthanide cations, typically arranged in the form of a mono-capped octahedral configuration, and (iv) an eightfold-coordinated distorted cube occupied by the lanthanide cation. As one moves across the

Ln3+ series from Pr to Yb, the size of the lanthanide ions contracts, affecting the tilt and deformation modes of the more rigid Ta-octahedron, thereby leading to structural changes in the other three more flexible Ln-polyhedra. In the case of the smallest lanthanide cations, these changes eventually result in a loss of long-range order, causing the folding of the orthorhombic weberite-type structure into a disordered structure resembling defect-fluorite. In this disordered structure, the two cations randomly occupy a shared cation site, while the oxygen vacancies are statistically distributed among the anion sites. However, recent findings on weberite-type oxides with the defect-fluorite structure [20], [45] and structurally related pyrochlore oxides suggest that short-range ordered correlations persist within these disordered compounds, distinct from the average long-range structure [13], [15], [17], [18], [46]. In contrast, ordered weberite-type Ln_3TaO_7 oxides exhibit small distortions [45] with respect to the parent fluorite structure, resulting in an orthorhombic lattice with pseudo-tetragonal characteristics.

In a similar manner to weberite oxides, the A and B cations' arrangement leads to the formation of different cationic tetrahedra: A_3B, A_2B_2, and A_4 (**Figures 2.10** and **2.11**). Similarly, unlike fluorites, and due to the large charge imbalance of B-rich tetrahedra, not all anions are located inside cationic tetrahedra; specifically, O3 is located outside the A_2B_2 tetrahedra and is displaced from the B-B face of tetrahedra (**Figure 2.11**). These cationic polyhedra arrangements persist in all ordered weberite-type oxides and differ slightly based on the material's structural model.

The utilization of families of structural models to describe the weberite-type oxides, specifically *Cmcm* or *Pnma*, *Ccmm* or $C222_1$, and *Fm-3m*, can be understood through the introduction of a prototypical 'parent' structure. This structure, devoid of tilt systems and displacive distortions, adopts a C-centered configuration with a *Cmmm* (65) symmetry. Importantly, its c-

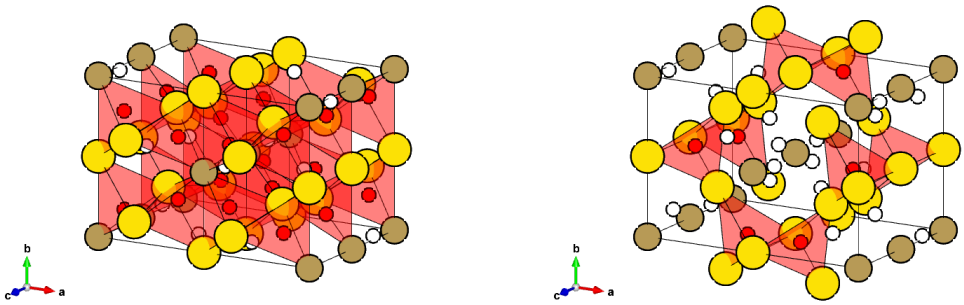

Figure 2.10: (Right): A_3B cation tetrahedra centered on O1 atom. Large brown and yellow spheres are Ta and Ln cations. Red spheres are O1 anions inside A_3B tetrahedra, shown in red shade. Small white spheres are the weberite-type structure's remaining O2 and O3 anions. (Left): A_2B_2 cationic tetrahedra with center on O2 atom. Large brown and yellow spheres are Ta and Ln cations. Red spheres are O2 anions inside A_2B_2 tetrahedra, shown in red shade. Small white spheres are the weberite-type structure's remaining O1 and O3 anions.

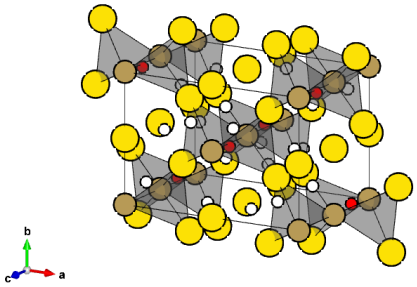

Figure 2.11: A_2B_2 cation tetrahedra with center on anion vacancy site, shown in gray shade. Large brown and yellow spheres are Ta and Ln cations. The O3 anions are shown as small red spheres and are displaced from the center of the tetrahedra. Small white spheres are the weberite-type structure's remaining O1 and O2 anions.

lattice parameter is halved when compared to the C-centered weberite-type configurations, adhering to the relationship $a_P = a_W$, $b_P = b_W$, and $c_P = ½c_W$ (**Figure 2.12**). The structural models for niobates and tantalates with the weberite-type structure are derived by analyzing the mechanical instabilities associated with the irreducible representations at the Y (*Pnma*), T (*Imma*), and Z (*Cmcm*) points in the centered orthorhombic Brillouin zone of the prototype weberite-type structure. Notably, for the Ta-centric compounds presented in this manuscript, a systematic derivation is possible when considering the Z-point irreducible representations. Conversely, Nb-centric compounds are accessible via Y-point representation. The most symmetric structural models, belonging to eight irreducible Z-point representations, are characterized by four centrosymmetric space groups, each with two distinct origins: Z1+, Z2- correspond to *Cmmm* (65); Z2+, Z1- correspond to *Cccm* (66); Z3+, Z4- correspond to *Cmcm* (63); and Z4+, Z3- are described by *Ccmm* (63) space groups. The symmetries of these space groups can be further reduced, depending on specific peaks in diffraction patterns that offer supporting evidence. For instance, removing the inversion center in either *Ccmm* or *Cmcm* produces the $C222_1$ symmetry in the respective reference orientation. Moreover, the loss of the primary symmetry operator, combined with a shift in the unit cell, leads to the transition from a C-centered *Cmcm* to a P-centered *Pnma* space group. The distinguishing factors of these space groups are characteristic supercell peaks which assist in identifying the optimal model for a particular compound when evident in high-resolution diffraction data.

2.4 Weberite-type motif in disordered pyrochlore oxides

Recently Shamblin *et al.* [17] performed neutron total scattering experiments to investigate a set of pristine and irradiated ordered ($Ho_2Ti_2O_7$) and disordered "defect-fluorite" ($Ho_2Zr_2O_7$)

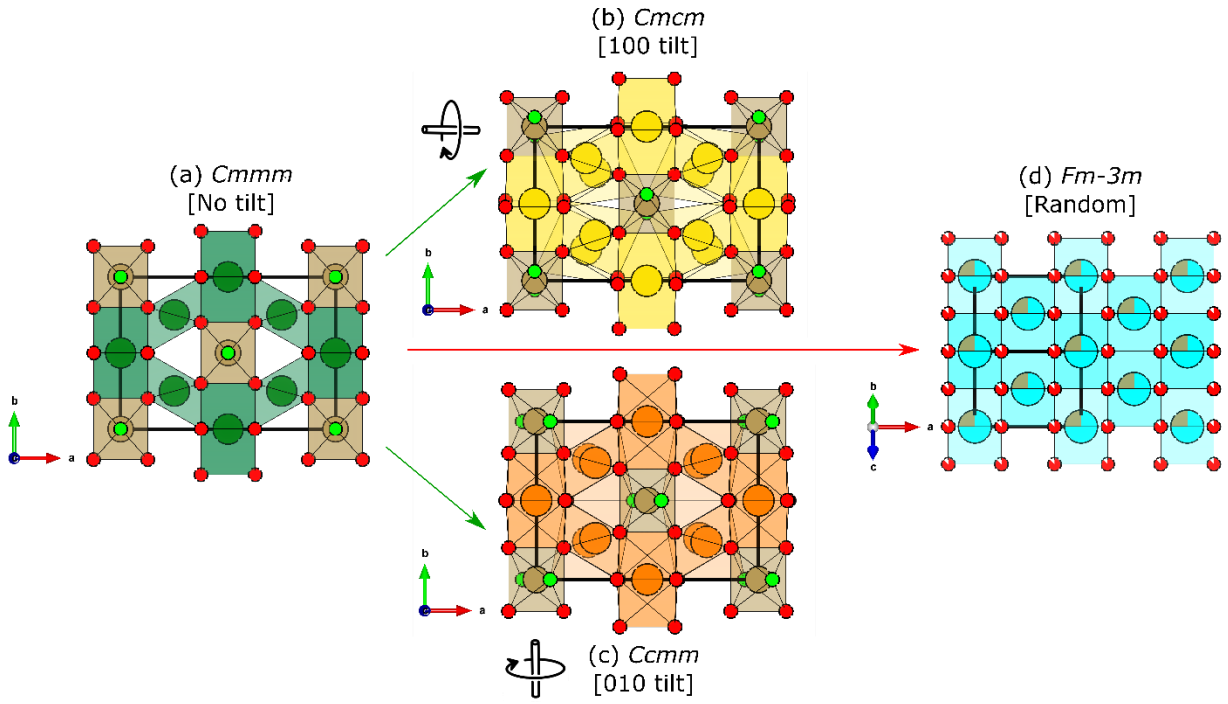

Figure 2.12: Relations among the three structural families of A_3TaO_7 weberite-type oxides. (*a*) single layer *Cmmm* prototype structure with no tilt system (*b*) *Cmcm* with [100] tilt, (*c*) *Ccmm* with [010] tilts and defect-fluorite *Fm-3m* with no tilt and random cation/anion ocupancy. Figure is reproduced from ref [45].

pyrochlore oxides to gain an insight into the so-called local structure. The pair distribution analysis of Fourier-transformed total scattering data has revealed that the local structure of disordered pyrochlore oxides cannot be successfully described by defect-fluorite atomic arrangement and is better modeled using a higher symmetry orthorhombic model. This orthorhombic model was derived from so-called weberite-type structures [20] and possesses a high level of local ordering: it contains ordered oxygen vacancies, specific cubic and octahedral sites occupied by B and A cations as well as the layer of seven-coordinated octahedral sites with mixed occupancy. This discovery has been re-emphasized [15], establishing that chemical doping in the solid solution series of ordered-to-disordered pyrochlores ($Ho_2Ti_{2-x}Zr_xO_7$) yields a different effect across different structural length scales. It has been shown that the introduction of a chemical dopant, in this case, Zr, dictates the formation of a local weberite-type phase, which progresses linearly with the Zr doping level. Finally, O'Quinn, *et al.* formulated the necessity to extend Pauling rules [14] for disordered materials and showed an underlying mechanism dictating the local pyrochlore to weberite-type structural transformation. All these studies had sparked an increasing interest in so-called weberite-type structures, which are both related to the structures formed under disordering conditions in pyrochlores and to the structurally modified well-studied weberite oxides.

It is interesting to consider that stoichiometrically-related $A_2B_2O_7$ pyrochlore structure is more closely related to fluorite structure than $A_2B_2O_7$ weberite since pyrochlore structure preserves all of the anions inside cation tetrahedra, whereas specific anion site in weberite structure (so-called X3 anion, located at *4e* Wykoff site) is located outside the cation tetrahedra which results in the vacant center for two AB_3 tetrahedra [9], [35]. For certain compounds, the metastable $A_2^{2+}B_2^{5+}O_7$ pyrochlore-like phase is observed and can be stabilized upon heating [33] or by F^{1-} anion doping [34], [35]. In the case of stable weberites, the formation of $A_2^{2+}B_2^{5+}O_7$ weberite and

not $A_2B_2O_7$ pyrochlore phase is dictated by an increased variance of accepted A and B cation radii as well as their A-O and B-O bond ionicity.

Chapter 3: Experimental Methods

Parts of this chapter are reproduced with permission from: *Igor M. Gussev, Eric C. O'Quinn, Gianguido Baldinozzi, Jörg Neuefeind, Rodney C. Ewing, Fuxiang Zhang, and Maik Lang, "Local order of orthorhombic weberite-type Y_3TaO_7 as determined by neutron total scattering and density functional theory calculations☆," Acta Mater., vol. 196, pp. 704–709, 2020, doi: 10.1016/j.actamat.2020.07.005.* [46] and *Igor M. Gussev, Eric C. O'Quinn, Matthew Tucker, Rodney C. Ewing, Cale Overstreet, Jörg Neuefeind, Michelle Everett, Qiang Zhang, David Sprouster, Daniel Olds, Gianguido Baldinozzi, Maik Lang, "Systematic study of short- and long-range correlations in RE_3TaO_7 weberite-type compounds by neutron total scattering and X-ray diffraction," J. Mater. Chem. A, pp. 8886–8903, 2023, doi: 10.1039/d3ta01042b.* [45]

3.1 Sample synthesis

Polycrystalline powders of A_3BO_7 (where A = Pr, Tb, Dy, Ho, Tm, Yb, Y; B = Ta, Nb, or Sb) were synthesized using a solid-state reaction process. Powders of tantalum, praseodymium, terbium, dysprosium, yttrium, holmium, thulium, and ytterbium oxides with a purity of 99.9998% were used as reactant materials. These powders were preheated in air at 1000 K for 12 hours to eliminate moisture. Subsequently, they were mixed, ground, and pressed into pellets (**Figure 3.1**) The resulting pellets were then heated in an air environment at 1200 K for 48 hours. Subsequently, they were ground again, repressed into pellets, and subjected to further heating in air at temperatures ranging from 1600 K to 1673 K for 156 hours. This procedure involved several intermediate regrinding steps. In the case of the A_3BO_7 polymorphs, an ordered orthorhombic weberite-type Ho_3TaO_7 was obtained by annealing at a maximum temperature of 1673 K. In

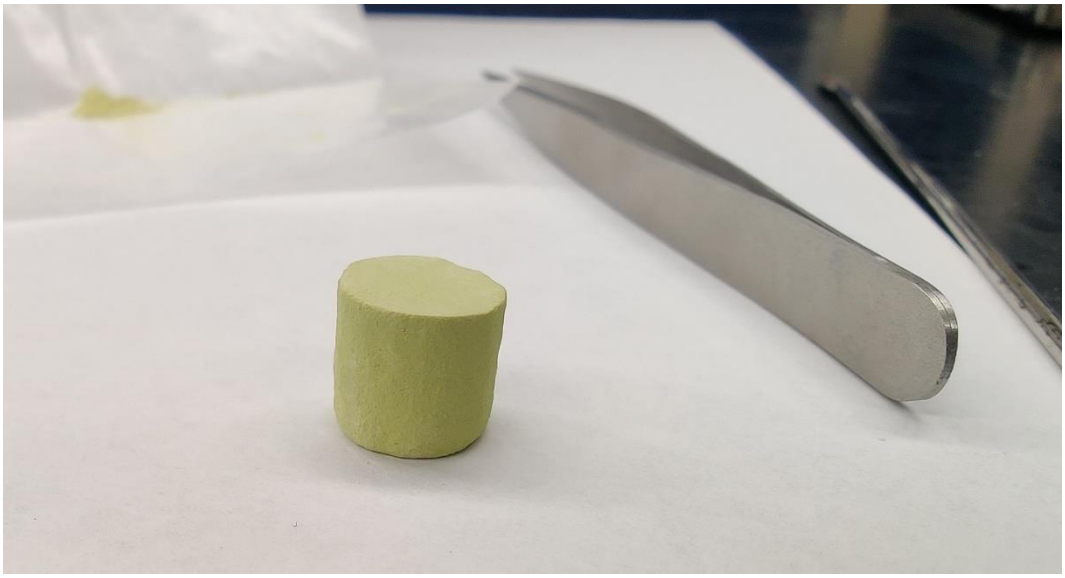

Figure 3.1: A picture of approximately 10g pellet of Pr_3TaO_7 weberite-type oxide.

contrast, a disordered, defect-fluorite-type Ho_3TaO_7 was prepared by annealing at a maximum temperature of 1973 K.

3.2 Swift Heavy Ion Irradiation

High-energy ion beams available at ion accelerator facilities, such as the GSI Helmholtz Center for Heavy Ion Research, are crucial components to achieve a sufficient amount of homogeneously irradiated sample mass (20-100 mg) necessary for Neutron and X-ray total scattering characterization techniques. To produce complex oxide materials disordered by swift heavy ions, the optimal sample geometry must be carefully constructed to isolate and investigate the effect of electronic energy loss. In particular, for each specific ion energy, the sample thickness must be optimized to ensure uniform energy deposition. The SRIM software package was used to determine the average dE/dx electronic energy loss and effective penetration depth (**Figure 3.2**).

There are two sample holder geometries used: (*i*) a larger-mass geometry optimized for one fluence point but yielding mass of irradiated sample necessary for neutron and X-ray total scattering experiments, and (*ii*) a lower-mass geometry optimized for providing X-ray diffraction measurements on irradiation series with multiple fluence points. The details regarding structural characterization methods of powders irradiated in these two geometries will be provided in the subsequent sections. In the first case, approximately 100 mg of each composition was subdivided among 9 specially made holders, with powder compacted into cylindrical indentations 50-75 μm deep and 1 cm in diameter, machined into each thin aluminum holders using a hydraulic press to a pressure of 25 MPa. (**Figure 3.3a**). These sample holders were then wrapped in 7 mm thick aluminum foil (**Figure 3.3b**). Nine holders were then mounted on a 5 × 5 cm aluminum plate (**Figure 3.3c**). All samples were irradiated with 8.6 MeV/n ^{197}Au ions (~1.69 GeV before the

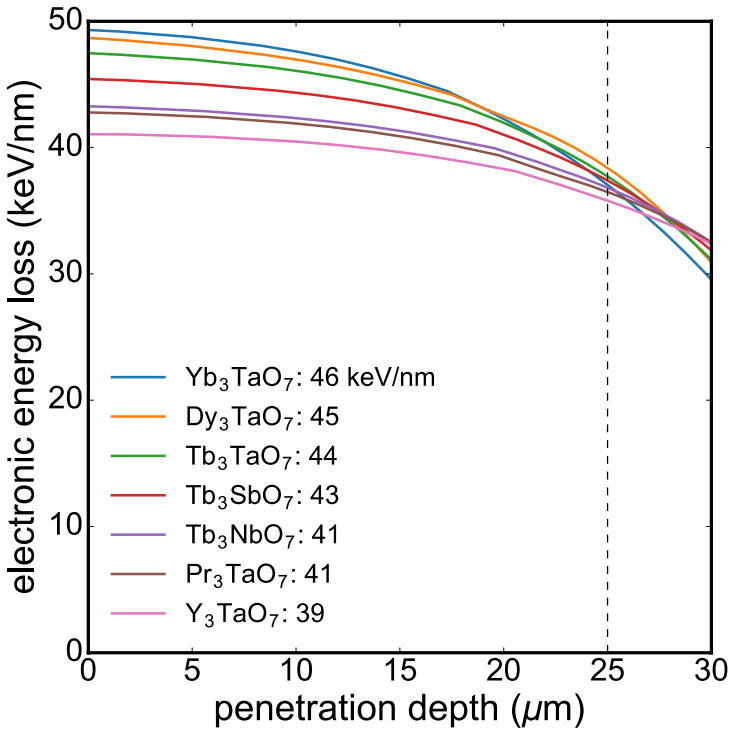

Figure 3.2: Energy loss profiles of 946 MeV ^{197}Au ions in the weberite-type compositions studied here as calculated with SRIM. Dashed vertical line denotes typical sample depth in the holder. The number given in the legend indicates the mean energy loss throughout the thickness of the sample. In all cases, the electronic energy loss (shown as colored lines) is over two orders of magnitude larger than the nuclear energy loss (not shown) throughout the sample volume.

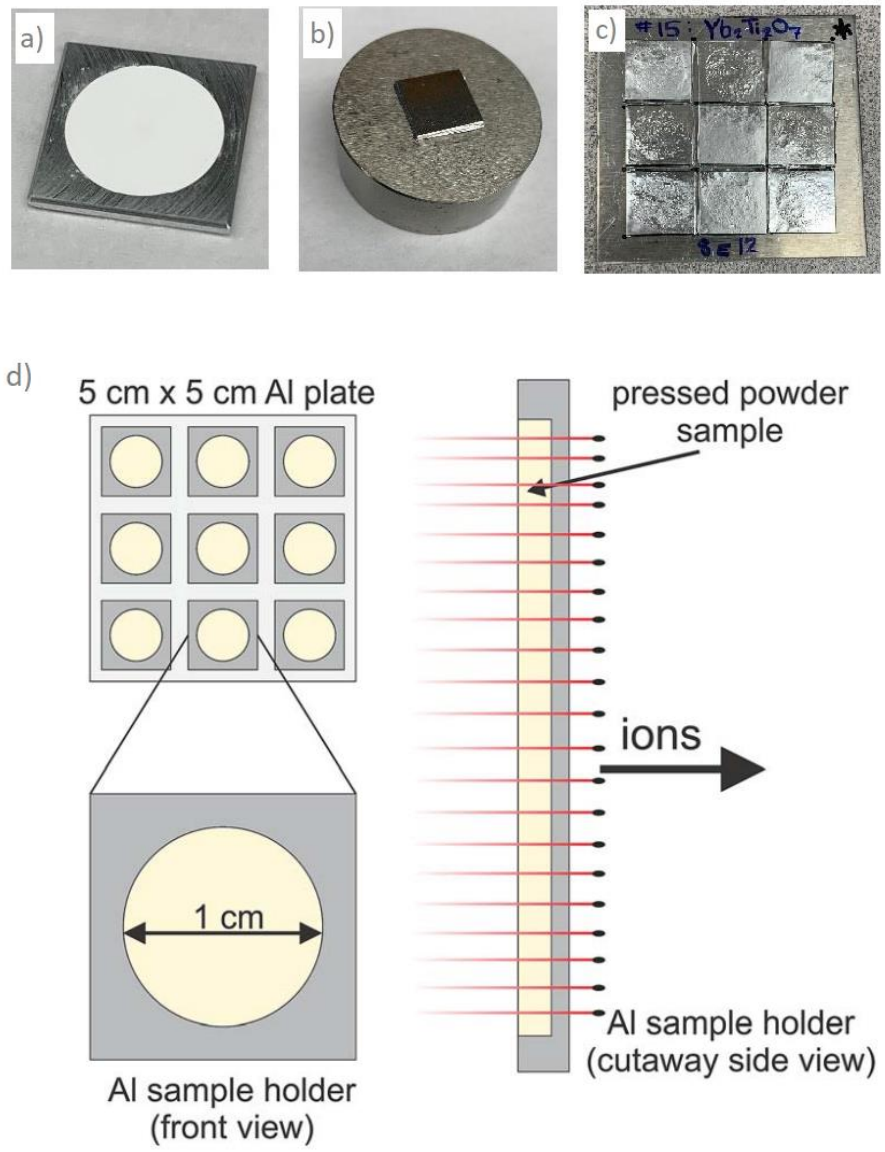

Figure 3.3: Sample holders used for larger mass ion irradiation experiments. (a) Powder sample is spread into cylindrical indentation of aluminum holder. (b) individual aluminum holder is covered in aluminum foil. (c) set of nine aluminum holders are mounted on 5×5 cm aluminum plate. (d) schematics of sample geometry for irradiation. Image taken from ref [47].

aluminum foil, 1.47 GeV when ions reach the sample) at the beamline X0 of the UNILAC accelerator at the GSI (**Figure 3.3d**). A broadly defocused beam was used to irradiate samples at room temperature to fluences up to 8×10^{12} ions/cm^2. After irradiation, the remaining sample was carefully scraped from the aluminum holders and placed into the respective sample containers for total scattering experiments. These irradiated samples are then characterized along with pristine reference samples using X-ray and neutron total scattering techniques.

In the case of the second irradiation geometry, a series of 9 samples was irradiated at the GSI with $^{197}Au^{28+}$ ions using the M3 beamline of the UNILAC. All samples were irradiated with a kinetic energy of 946 MeV (4.6 MeV/u). The powders were pressed into 100 µm diameter holes in molybdenum sample holders of 25 µm thickness. The sample thickness was also corrected for the limited packing fraction of the polycrystalline powders [47], [48], which was assumed to be 60% based on previous studies that assessed the maximum sample densities of similar ceramic materials achieved under similar cold, uniaxial pressing [47]. First, the electronic energy loss was calculated using the theoretical density in SRIM [49]; theoretical densities were used because the ions deposit their energy within single grains of theoretical density, but not in the voids between them. Afterward, the projected penetration depth was corrected to include the 60% packing fraction. This effective penetration depth of the ions after density correction was well beyond 30 µm and thus the sample thickness. The limited thickness of the samples ensured complete penetration of the ion and relative constant energy loss, dE/dx (**Figure 3.2**). Seven holes were filled for a given target fluence, providing multiple samples for statistical purposes and redundancy in case of sample loss. All materials were simultaneously irradiated *in vacuo* at the M3 beamline at approximately 300 K with an ion flux of ~2×10^9 ions cm^{-2} s^{-1} until the following target fluence values were achieved: 1×10^{11}, 3×10^{11}, 5×10^{11}, 8×10^{11}, 1×10^{12}, 3×10^{12}, 5×10^{12}, 8×10^{12}, 1×10^{13},

and 3×10^{13} ions/cm^{-2}. An aluminum frame with an effective irradiation window of 1 x 1 cm^2 [50] was used to fix the molybdenum sample holders for each fluence step and the beam-spot size utilized was 1.25 x 1.25 cm^2. The samples of this fluence series were after irradiation characterized by synchrotron-based XRD experiments (**Figure 3.4**).

3.3 High-Energy synchrotron X-ray diffraction

Synchrotron X-ray diffraction (SXRD) was performed on A_3BO_7 samples at the Pair Distribution Function beamline (28-ID-1) of the National synchrotron Light Source-II (NSLS-II) at Brookhaven National Laboratory (BNL) as well at 16-BM-D high-pressure collaborative access team (HPCAT) beamline at Argonne National Lab (APS) (**Figure 3.5**). In the first case, all sample powders were placed in an airtight Kapton tube sample container with a 1 mm diameter and 0.6 μm wall thickness with plastic stoppers on both ends. These containers were mounted on a custom-made holder system, allowing vertical movement in the beam to homogenize the powder diffraction intensity and minimize potential texture effects. Additionally, a LaB_6 calibration standard and an identical empty sample container were mounted on the same holder to provide calibration data and subtract the Kapton background intensity. In the latter case, the samples were measured in their original irradiation holders along with the CeO_2 calibration standard. The X-ray diffraction data were acquired with an exposition time of 1 minute with a photon energy of 74.47 keV (λ of 0.1665 Å) for 28-ID-1 and with an energy of 30 keV (λ of 0.4133 Å) for 16-BM-D. The X-ray powder diffraction data were acquired as 2D diffractograms using the Perkin Elmer XRD 1621 detector (NSLS-II) and MAR detector (APS) and converted to 1D diffraction profiles using Dioptas [51] (**Figure 3.6**).

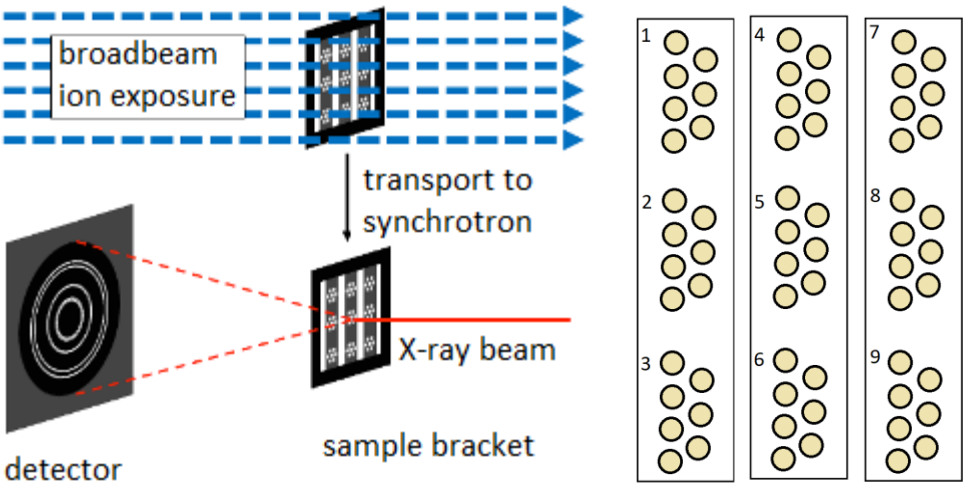

Figure 3.4: (Left) A schematic of sample irradiation and characterization procedures used for fluence series of irradiation experiments. (Right) Schematic of the sample bracket containing 9 samples placed into a respective group of 7 holes. The entire sample assembly contains three aluminum strips with three samples per strip. This method allows for simultaneous irradiation of series of samples under identical irradiation conditions.

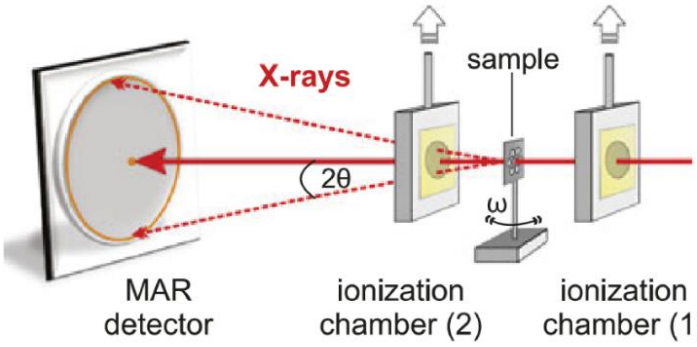

Figure 3.5: Schematics of X-ray diffraction experiment at beamline HPCAT 16-BM-D of the Advanced Photon Source. Figure is reproduced from ref [50].

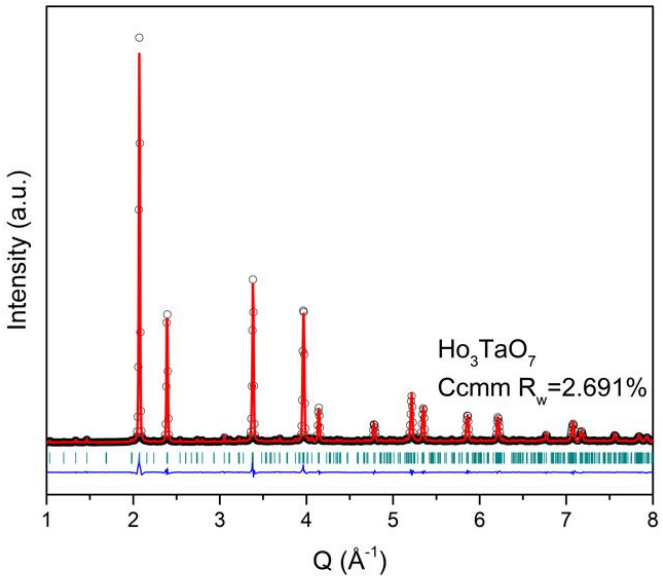

Figure 3.6: An example of X-ray diffraction profile of pristine Ho_3TaO_7 weberite-type oxide acquired at NSLS-II. Figure is reproduced from [45].

3.4 Neutron total scattering

Neutron total scattering characterization was performed on pristine and irradiated Pr_3TaO_7, Tb_3TaO_7, two polymorphs of Ho_3TaO_7, Tm_3TaO_7, and Yb_3TaO_7, using the time-of-flight Nanoscale-Ordered Materials Diffractometer (NOMAD) [52] at the beamline BL-1B at the Spallation Neutron Source (SNS) at Oak Ridge National Lab (ORNL). All samples were loaded into 2 mm quartz capillaries with a wall thickness of 0.01 mm. The measurements were performed at room temperature with an exposure time of 64 minutes (4C target charge) per sample (**Figures 3.7 and 3.8**). The six NOMAD detector banks were calibrated using scattering from a diamond powder and silicon sample. The silicon standard was used to obtain the instrument parameter file for the Rietveld refinements. The scattering intensity from an empty sample position as well as from an empty 2mm quartz capillary was measured as background signals and automatically subtracted from the scattering intensity of the polycrystalline powder samples. The resulting scattering intensity of each sample was normalized to the scattering intensity of a solid vanadium rod to account for the spallation neutron spectrum and detector inefficiencies. A Fourier transform was applied to the structure functions, S(*Q*), to obtain the pair distribution function,

$$\mathrm{G(r)} = A * \mathrm{Q}_{max} \int_{Qmin}^{Qmax} \mathrm{Q(S(Q)-1)Sin(Qr)dQ} \qquad \text{(Equation 3.1)}$$

where the maximum momentum transfer (Q_{max}) was 31.4 $Å^{-1}$ and *A* is an arbitrary scale parameter determined during post-processing assessment or small-box modeling of the experimental data (**Figure 3.8**). In the case of lower-mass irradiated samples, the Q_{max} was set to 25Å to limit the Fourier transform effects which arise from (*i*) the finite Fourier transform and (*ii*) unphysical statistical noise at high-*Q*. The momentum transfer is defined as: $Q = 4\pi sin\theta/\lambda$, where λ and θ are the neutron wavelength and scattering angle, respectively. Additional low-temperature neutron

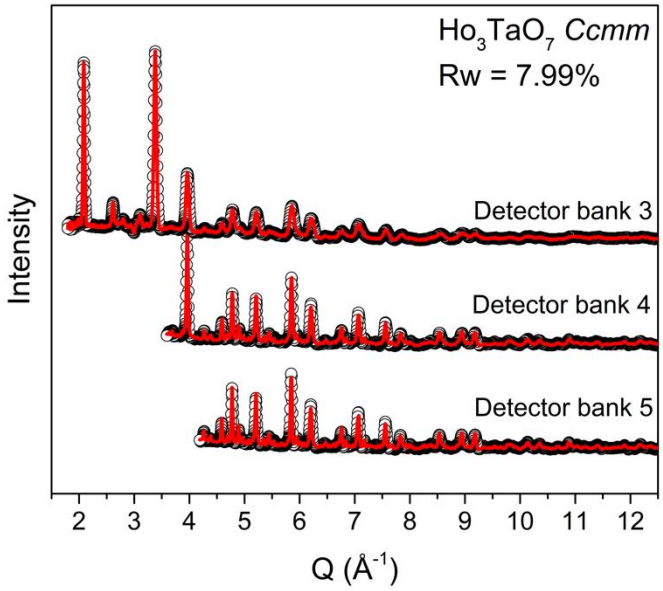

Figure 3.7: Room temperature diffraction profile of pristine Ho_3TaO_7 weberite-type oxide measured at NOMAD. The data and Rietveld refinements are shown for NOMAD detector banks 3, 4 and 5.

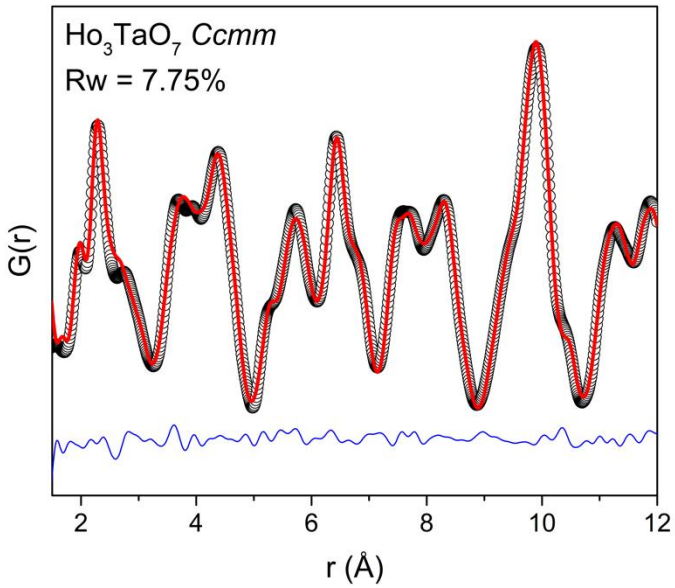

Figure 3.8: Room temperature pair distribution function (PDF) of pristine Ho_3TaO_7 weberite-type oxide measured at NOMAD and refined using small box modeling approach.

total scattering measurements were performed for pristine Pr_3TaO_7, Ho_3TaO_7, and Yb_3TaO_7 at 100 K using an otherwise identical instrument setup and data processing scheme.

3.4 High-resolution neutron diffraction

Additional high-resolution neutron diffraction measurements were performed on pristine (unirradiated) Pr_3TaO_7 and Ho_3TaO_7 samples using the POWGEN (High resolution time-of-flight diffractometer) [53] at the beamline BL-11A at the SNS, ORNL. Measurements were made with an exposure time of 4 hours per sample at room temperature using the frame 2 setting of the diffractometer (wavelength of 0.97-2.033 Å with a center λ of 1.5 Å). The samples were placed in 6 mm vanadium cans and filled with helium exchange gas prior to measurement. The calibration standard, empty sample containers, and vanadium rod were measured separately before the measurement to collect the data to be used in background subtraction and normalization. The POWGEN Automatic Changer (PAC) was used as the sample environment, which allowed measurements within a temperature region of 10-300 K (**Figure 3.9**). An additional low temperature neutron diffraction measurement was performed at 100 K on Ho_3TaO_7, using otherwise similar measurement conditions and data processing procedures.

3.5 Density functional theory

The first-principles calculations were used to evaluate the relative stabilities of the two orthorhombic phases in the pristine Y_3TaO_7 composition. These electronic structure calculations were performed within the DFT framework using the projector-augmented wave (PAW) approach for the core-valence interaction and the general gradient approximation with Perdew-Burke-Ernzerhof (PBE) [54] generalized gradient approximation for the exchange-correlation functional

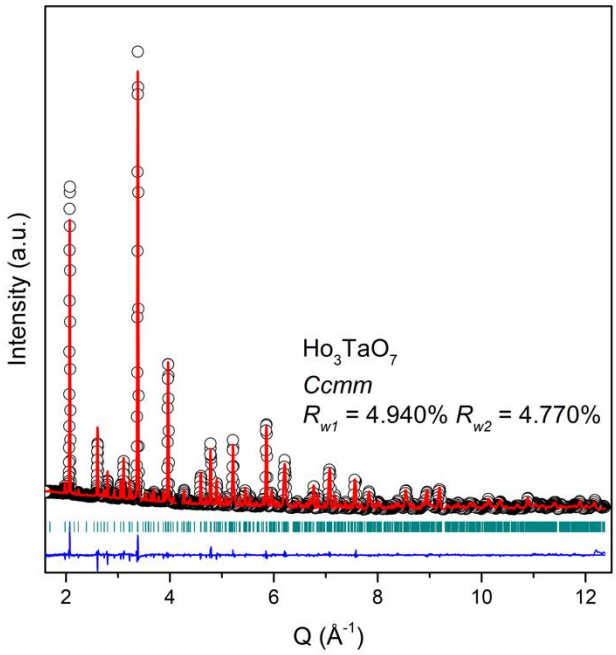

Figure 3.9: Room temperature high-resolution diffraction profile of Ho_3TaO_7 weberite-type oxide measured at POWGEN. The diffraction profile is split into two regions: 4 - 12.5Å and 1.5 - 4Å. The respective fit reliability factors (Rw_1 and Rw_2) are reported for each region. Figure is reproduced from [45].

as implemented in the VASP code [55]. The potentials included 11 valence electrons for Ta, 11 for Y, and 6 for O. A plane-wave kinetic energy cutoff was determined at 520 eV, with a uniform k-point mesh (6×6×5) for Brillouin zone sampling based on the Monkhorst-Pack scheme that was found to be sufficient to achieve well-converged energies. These parameters were used for static self-consistent calculations of the primitive cells having *Cmcm* and $C222_1$ symmetries, respectively. Electronic self-consistency was considered to be achieved when the total energy change between electronic steps was less than 1 μeV. The lattice metric was relaxed for all crystal symmetries and the internal structural parameters were relaxed until all Hellmann-Feynman forces on each ion were less or equal 2 meV/ Å. The *Cmcm* and $C222_1$ *(b,a,-c)* structures acquired from DFT calculations were later transposed into *Ccmm* and $C222_1$ *(a,b,c) via* simple lattice vector exchange for comparison with experimental results.

3.6 Data analysis

3.6.1 Rw reliability factor calculation

The long-range structures were analyzed using the Rietveld refinement method performed in the GSAS (EXPGUI) [56] and GSAS-II [57] software packages. The highest *Q*-resolution backscattering detector banks (3, 4, and 5) with different *Q*-space coverage and resolution were refined simultaneously for the NOMAD diffraction data, resulting in a single cumulative reliability factor parameter (R-factor), referred to as *wRp* in GSAS-I software or *Rw* in this study to avoid confusion. The POWGEN and SXRD diffraction patterns were refined using a single detector bank. During refinement of the POWGEN data, the diffraction patterns were divided into two *d*-space regions to minimize the effect of varying instrumental resolution across the large detector coverage in *d*-space. Therefore, the reliability factor is reported as two separate values (Rw_1 and

Rw$_2$) for POWGEN diffraction data and as single value (*Rw*) for SXRD data. For all symmetries used, the following sets of parameters were refined: 6 Chebyshev background parameters, scale factor, respective unit cell dimensions ($a \neq b \neq c$ for orthorhombic cells, $a = b = c$ for cubic cells), respective allowed positional parameters and harmonic U_{ij} for POWGEN diffraction and isotropic U_{iso} for NOMAD and SXRD diffraction for individual atomic sites [45].

Small-box refinements of neutron pair distribution functions (PDFs), representing the short-range structure, were performed using the PDFgui software [58]. Similar to the long-range refinement, scale factor, PDFgui specific *delta2* parameter (to account for the correlated displacements of the distances between nearest neighbors), allowed unit cell parameters ($a \neq b \neq c$, $\beta \neq 90°$ for monoclinic cells, $a \neq b \neq c$ for orthorhombic cells, and $a = b = c$ for cubic cells), and positional parameters were refined. Depending on the refinement type (discussed later in more detail), both isotropic (U_{iso}) and harmonic (U_{ij}) atomic displacement parameters (ADP) were used for each applicable atomic site. The VESTA software [59] was used to visualize and produce all 3-D structural images for visualization and interpretation, as well as to extract the necessary information from polyhedra. So-called 'boxcar' refinements were performed using PDFgui software with *r*-series macros, using the initial parameters of each refinement from previous fits. The initial fit range was set as 1.5-12 Å (10.5 Å fit window), with subsequent fits performed by increasing the minimum *r*-value (r_{min}) in 1 Å increments while keeping the same fit window size (*i.e.*, 2.5– 13 Å, 3.5-14 Å, etc.).

In both Rietveld and small box refinement, the cumulative *R*-factor (reliability factor, *Rw*) was defined as following:

$$R_w = \sqrt{\frac{\sum_{i=1}^{N} w(r_i)[G_{obs}(r_i) - G_{calc}(r_i)]^2}{\sum_{i=1}^{N} w(r_i) G_{obs}^2(r_i)}} \qquad \text{(Eq. 3.2)}$$

Where G_{obs} and G_{calc} are observed and modelled intensities at point r_i, and $w(r_i)$ is weighting factor, defined by the uncertainty in the data file.

3.6.2 Correlated G(r) calculation approach

In addition to the *R*-factor analysis of the PDF data, the *S*-factor analysis technique was adopted in this study. This was based on the diffraction data refinement approach and used here to estimate the limits of the local correlations and calculate the *correlated reliability factor* (*Gs*) for PDF data. Adopting equation 6 from [60], *Gs* is defined accordingly for the real space $G(r)$ data:

$$G_s = \sum_{j \in uncorrelated\ region} w_j \left(G_{obs}(r_j) - G_{calc}(r_j)\right)^2 + \sum_m \left(\sum_{k \in correlated\ region} w_k^{1/2} \left(G_{obs}(r_k) - G_{calc}(r_k)\right) \right)^2 \qquad \text{(Eq. 3.3)}$$

Where the first summation is the usual one; whereas the second summation, over *k*, is only defined on sets of neighboring points within each correlation region m, and it is the simple square of the sum of the *G(r)* differences, which are further summed across all correlated regions. The parameters G_{obs} and G_{calc} are the observed and calculated intensities at each point of *G(r)*, respectively. Two neighboring points are deemed correlated when the product of their differences across two points have the same sign and the modulus exceeds a specific threshold value, that is a chosen function of the statistical weights w_j:

$$|(G_{obs}(r_i) - G_{calc}(r_i)) * (G_{obs}(r_{i-1}) - G_{calc}(r_{i-1}))| > threshold \qquad \text{(Eq. 3.4)}$$

When the points are deemed uncorrelated, the *Gs* calculations fall back to the unnormalized *Rw* expression (Eq. 3.2); however, the length of the correlated regions dramatically affects the *Gs* value. A set of threshold values based on the confidence interval of the *G(r)* values was then used

to identify the regions where the error is correlated. The advantage of using *Gs* instead of *Rw* for the PDF analysis is that the *Rw* factor is biased by the assumption of uncorrelated errors, whereas *Gs* accounts for systematic correlations within the difference curve.

The maximum *r*-value (r_{max}) used for the refinements is relatively large, typically bigger than the largest dimension of the unit cell used for the different structural models (r_{max} ~ 12Å). Therefore, the *Rw* value is less sensitive to the fit quality in the low-*r* region (< 5Å), most important to the distortions of the coordination polyhedra, because it includes the contributions at high-*r* from the higher order atomic correlations (*e.g.*, second-, third-, … nearest neighbors). In addition, the PDF data across different sample compositions is affected by a scattering-length 'efficiency' effect due to the presence of different lanthanide ions. For example, the neutron scattering length of Yb is 12.4 fm, which is approximately twice the scattering length of O (5.80 fm) or Ta (6.91 fm). Therefore, the signal from Yb-Yb pair correlations dominates the refinement (as these peaks are typically much more intense than the corresponding O-O pair correlations), affecting the difference curve and the calculation of the *Rw* value. This bias can be somewhat adjusted by limiting the *r*-range of the PDF refinement to the region sensitive to the coordination polyhedra and the nearest neighbor distances (r_{max} ~ 4.2 Å). Over this fit range, only cation-oxygen and oxygen-oxygen correlations are typically present, which reduces the relative impact of the scattering lengths of the different lanthanides.

3.6.3 Amorphous fraction extraction procedure

The XRD patterns collected from the Advanced Photon Source (APS) were analyzed to extract amorphous phase fractions. The patterns were decomposed into crystalline and amorphous contributions, following an approach described in detail elsewhere [10]. The respective integrated

peak areas were determined, and the amorphous phase fraction was the amorphous area normalized to the total area of a given XRD pattern. Peak deconvolution and integration were performed with the FITYK software [61] dividing each diffraction pattern into two regions according to the two main amorphous bands (from ~5-10 two theta and ~10-17.5 two theta). A general background was removed from each section of the diffraction pattern, and crystalline diffraction reflections and broad amorphous contributions were fit with pseudo-Voigt and Gaussian functions, respectively. This procedure was applied to each diffraction pattern at every fluence measured. Rietveld refinements were performed on XRD patterns measured on all pristine samples to evaluate the quality of each starting material and on the diffraction patterns of irradiated samples to identify the formation of secondary phases. For sample compositions, which showed only radiation-induced amorphization, a single impact model [62] was used to describe the fluence-dependent behavior of amorphous phase fractions, where Φ is the fluence of the ions (in ions/cm^2) and σ the cross sectional area of the track (in cm^2/ion):

$$f_a = 1 - e^{-\sigma\phi} \qquad \text{(Eq. 3.5)}$$

For compounds in which the amorphization did not saturate at unity within the evaluated fluences and showed evidence of a secondary crystalline phase induced by ion irradiation, a track overlap model introduced by Tracy *et al.* [13], [63] was used, assuming a complex track morphology with a disordered shell (σ_d) surrounding an amorphous core (σ_a):

$$f_a = \frac{1-e^{(\sigma_d-\sigma_a)\phi}}{1-\left(\frac{\sigma_d}{\sigma_a}\right)e^{(\sigma_d-\sigma_a)\phi}} \qquad \text{(Eq. 3.6)}$$

in which recrystallization of the amorphization phase can occur in the disordered phase corresponding to the disorder cross section, σ_d.

Chapter 4: Local order of orthorhombic weberite-type Y_3TaO_7 as determined by neutron total scattering and density functional theory calculations

This chapter is reproduced with permission from: *Igor M. Gussev, Eric C. O'Quinn, Gianguido Baldinozzi, Jörg Neuefeind, Rodney C. Ewing, Fuxiang Zhang, and Maik Lang, "Local order of orthorhombic weberite-type Y_3TaO_7 as determined by neutron total scattering and density functional theory calculations☆," Acta Mater., vol. 196, pp. 704–709, 2020, doi: 10.1016/j.actamat.2020.07.005.* [46]. Introductory information regarding weberite-type structures is summarized in Chapter 2 while the experimental techniques are summarized in Chapter 3. This work was supported by the U.S. Department of Energy, Office of Science, Basic Energy Sciences, under Award DE-SC0020321. E.C.O. acknowledges support from the U.S. Department of Energy, Office of Science, Office of Workforce Development for Teachers and Scientists, Office of Science Graduate Student Research (SCGSR) program. The SCGSR program is administered by the Oak Ridge Institute for Science and Education for the DOE under contract number DESC0014664. The research at ORNL's Spallation Neutron Source was sponsored by the Scientific User Facilities Division, Office of Basic Energy Sciences, U.S. Department of Energy. We thank Michelle Everett (ORNL) for guidance during the neutron scattering experiments.

4.1 Abstract

Weberite-type oxides are a family of oxides with A_3BO_7 stoichiometry that can adopt different space groups depending on chemical composition. There is a discrepancy in previous studies as to whether Y_3TaO_7 is the orthorhombic $C222_1$ or the *Ccmm* space group. Here, we describe the short- and long-range structural properties of weberite-type Y_3TaO_7 using neutron total scattering data,

which has a high sensitivity to the oxygen sublattice. Simultaneous analysis of both short- and long-range structural data *via* conventional Rietveld and small box modelling demonstrates that Y_3TaO_7 is best modeled as $C222_1$. While the *Ccmm* describes equally well the long-range structure, pair distribution function analysis revealed that the local atomic configuration can be best modelled as $C222_1$. This is corroborated by first-principles calculations that confirm the energetic preference of the $C222_1$ over *Ccmm*. Neutron total scattering data are reported for the first time for the Y_3TaO_7 weberite-type ceramics.

4.2 Introduction

Advances in the development of energy technologies require specifically engineered materials that maintain structural stability in harsh working conditions, such as extreme radiation fields and high temperatures [64]. Complex oxide ceramics are promising candidates for a number of energy-related applications, such as nuclear waste-containing matrices and solid electrolyte fuel cells. Despite the wide body of research into the radiation response of such materials [12], [19], [65], [66], there is a limited understanding of the impact of extreme environments on their atomic-scale behavior. Recent neutron total scattering experiments have revealed that the local structure plays an important role in understanding irradiation-induced structural disorder in pyrochlore oxides ($A_2B_2O_7$) [19]. Depending on the chemical composition, ion irradiation will either induce an order-to-disorder transformation (all the while maintaining long-range crystallinity) or lead to complete amorphization [67], [68]. Analysis of neutron total scattering revealed that the local atomic arrangement is nearly identical in both amorphous and disordered pyrochlore oxides and can be best described by a weberite-type structural model [18]. Intriguingly, this weberite-type atomic arrangement also has been reported for pyrochlore compositions disordered by a variety of other methods including high-temperature treatment, high-energy ball milling [69], chemical

doping, or deviation from ideal stoichiometry [17]. As this weberite-type configuration appears to be a general phenomenon in disordered pyrochlore, there has recently been an increased interest [70] in oxide materials that exhibit the weberite-type structure over all length-scales.

Weberite-type tantalates (general formula A_3BO_7) with the A-site occupied by a rare-earth cation and the B-site occupied by Ta, can display either an ordered, orthorhombic weberite-type structure or a disordered, anion-deficient fluorite structure. The size of the A-site cation determines whether an ordered or disordered phase is formed. When the A-site cation is large (La, Ce, Pr) weberite-type oxides adopt a *Cmcm* space group, while medium-sized (Y, Pm through Dy) and smaller cations (Er through Lu) are orthorhombic ($C222_1$) and the disordered, anion-deficient fluorite (*Fm-3m*) structures, respectively [5]. Nd_3TaO_7 can be synthesized as a mixed-phase material (*Cmcm* and $C222_1$), while Ho_3TaO_7 can form either a $C222_1$ or *Fm-3m* phase, depending on the synthesis conditions and temperature treatment. [5]. There is no consensus in the literature [30], [39] on the best structural model for Y_3TaO_7 and different space groups have been proposed, including $C222_1$ [5], [8], [36], [70], *Ccmm* [39] and *Fm-3m* [71]. Previous neutron total scattering experiments showed that the $C222_1$ space group was the best fit to the local atomic arrangement of Yb_3TaO_7 with a long-range disordered-fluorite structure [20]. Most of these studies utilized either X-ray diffraction with limited structural information on the oxygen sublattice and local atomic arrangements or Raman spectroscopy that yields complex vibrational information, particularly for low-symmetry structures.

In this study, the limitations of X-ray diffraction and Raman spectroscopy are overcome by utilizing neutron total scattering. The weberite-type Y_3TaO_7 has favorable elements for neutron scattering analysis with Y having a large neutron scattering cross section and low absorption cross-section. Neutron total scattering simultaneously provides information on both short- and long-

range structures with high sensitivity to the oxygen sublattice. Here we report, using analysis of diffraction data and pair distribution functions, that the orthorhombic *C222₁* is the most appropriate structural model for the Y_3TaO_7 weberite-type compound. The validity of the proposed structural model is supported by density functional theory (DFT) calculations as energetically the most stable configuration.

4.3 Results and discussion

Refinements of neutron diffraction data confirmed that the as-prepared Y_3TaO_7 material was a pure single phase. The diffraction patterns (NOMAD detector banks 3 through 5) could not be indexed with a disordered, anion-deficient fluorite *(Fm-3m)* phase due to the obvious presence of peaks not indexed by the *Fm-3m* space group. The refinements with the two orthorhombic structural models proposed in literature, *Ccmm* and *C222₁*, are shown in **Figure 4.1**. These refinements (**Table 4.1**) revealed that both orthorhombic models yield nearly identical refinement quality as expressed by the goodness-of-fit parameter *Rw* (8.84% and 8.75% for *Ccmm* and *C222₁*, respectively). The two orthorhombic structural models acquired from the Rietveld refinements (**Figure 4.2**) are similar in terms of symmetry, and they are related to the cubic fluorite structure.

The idealized orthorhombic structure (**Figure 4.*2a***) consist of 6-coordinated Ta cations forming octahedra (TaO_6) as well as 8 and 7-coordinated Y cations forming distorted cubes (YO_8 and YO_7, where one oxygen site is replaced by a vacant site). The TaO_6 octahedra are tilted toward [100], share one oxygen atom, and form an infinite one-dimensional zig-zag chain projected along the [001]. The YO_8 distorted cubes share edges and form chains parallel to [001]. Combinations

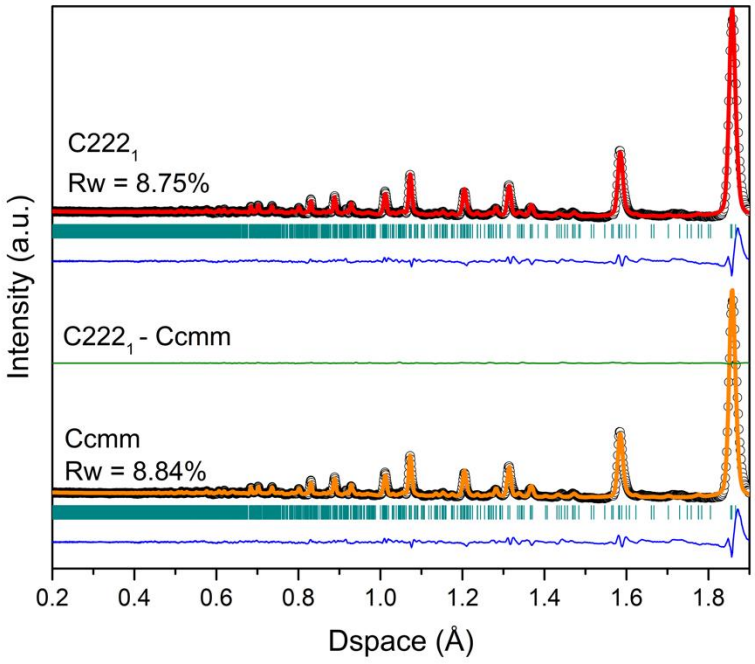

Figure 4.1: Neutron diffraction pattern of Y_3TaO_7 (NOMAD detector bank 4) as measured (black circles) and modeled using *Ccmm* (orange line, bottom profile) and *C222$_1$* (red line, top profile) space groups. The blue lines represent the difference curves between the experimental data and the model fit with the *Rw* values being the goodness-of-fit parameter. The green line represents the difference in diffraction profiles between the *C222$_1$* and *Ccmm* model, respectively.

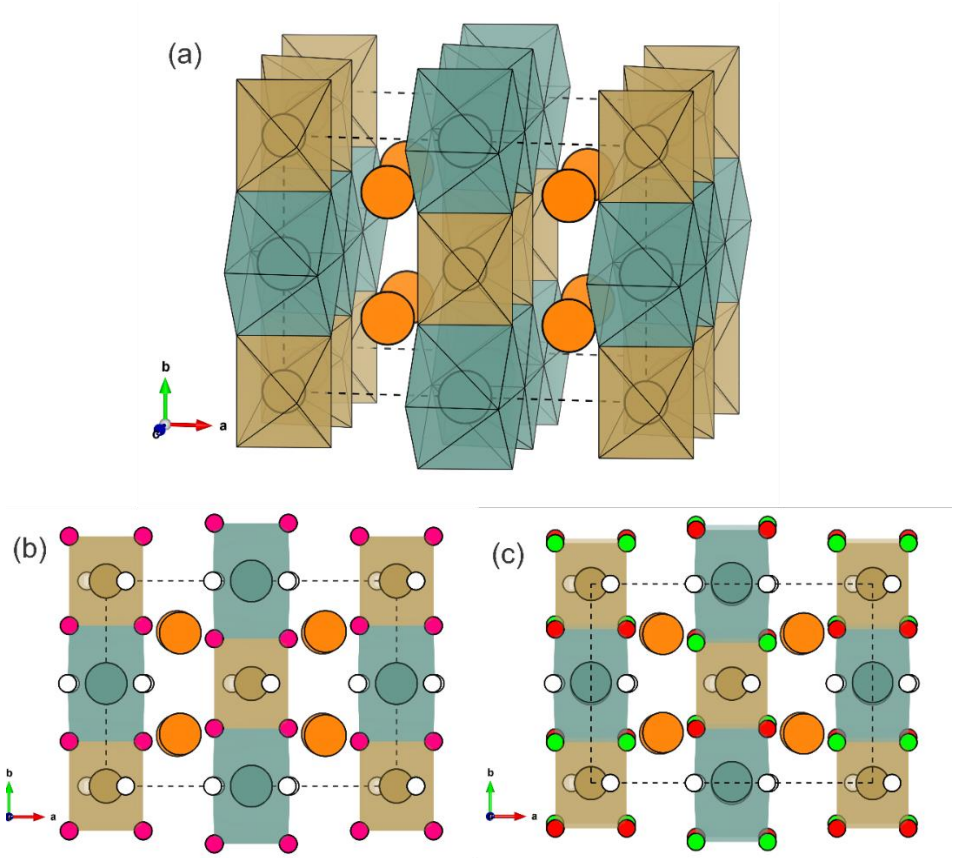

Figure 4.2: Schematic representations of the Y_3TaO_7 structures with dashed black lines representing the unit cells. (a) Idealized structural model with cations are shown for tantalum as golden-sand colored spheres and yttrium as cyan color spheres (8-coordinated) or as orange spheres (7-coordinated). Selected coordination polyhedra are represented using similar shades (YO_7 polyhedra are not shown). (b) Structure resulting from GSAS refinement using *Ccmm* symmetry viewed along [001]. 16h oxygen sites are shown as smaller magenta spheres, while three 4a oxygen sites are displayed as white spheres. (c) Structure resulting from GSAS refinement using $C222_1$ symmetry viewed along [001]. Two 8c oxygen sites are drawn as red and green spheres while three 4a oxygen sites are shown as white spheres. The $C222_1$ structure is shifted by ¼ *c* along [001] for the ease of comparison.

of those two chains form slabs parallel to (011); whereas the YO_7 distorted cubes are located between these slabs.

Although both orthorhombic structure types share the same cation sublattice, there is a difference in symmetry of the anion sublattice, as shown in **Figures 4.2b** and **4.2c**. Oxygen atoms located at the 16*h* Wyckoff site in the *Ccmm* structure are split into two identical 8*c* Wyckoff sites in the $C222_1$ structure. The latter allows for subtle distortions of the 6-coordinated Ta polyhedron, as well as the 7- and 8-coordinated yttrium polyhedra. This effect leads to slight variations in the <O-O> interatomic distances among both structure types. Although these variations are very small, they impact Rietveld refinement of the diffraction patterns and have an influence on the goodness-of-fit parameter *Rw*. This value is slightly lower for the $C222_1$ model (**Figure 4.1**), which indicates that this structure-type fits the data somewhat better. Application of a significance test developed by Hamilton [72] results in a confidence value of 99.95% that $C222_1$ is a more appropriate structural model, despite the addition of several refinement parameters. This similarity in R factors of both structural models explains the discrepancy in literature [5], [8], [30], [36], [39], [71] and highlights that diffraction experiments alone, even with neutron probes, are most likely not unambiguous for the accurate determination of the structure of Y_3TaO_7.

Insight into the short-range structure was obtained through analysis of the pair distribution function (**Figure 4.3**). Small-box refinements based on the *Ccmm* and $C222_1$ structural models yield R_w values of 7.18 % and 5.54% for *Ccmm* and $C222_1$, respectively (Table 1). As indicated by the difference curves of data and model fit, the higher R_w value for *Ccmm* is primarily related to deviations in intensity and position of the peak at 2.8 Å, denoted by an asterisk. The origin of this behavior can be better seen in the PDF data capturing only the *r*-range of local coordination polyhedra with the <Ta-O>, <Y-O>, and <O-O> nearest neighbor distances (**Figure 4.4**). The

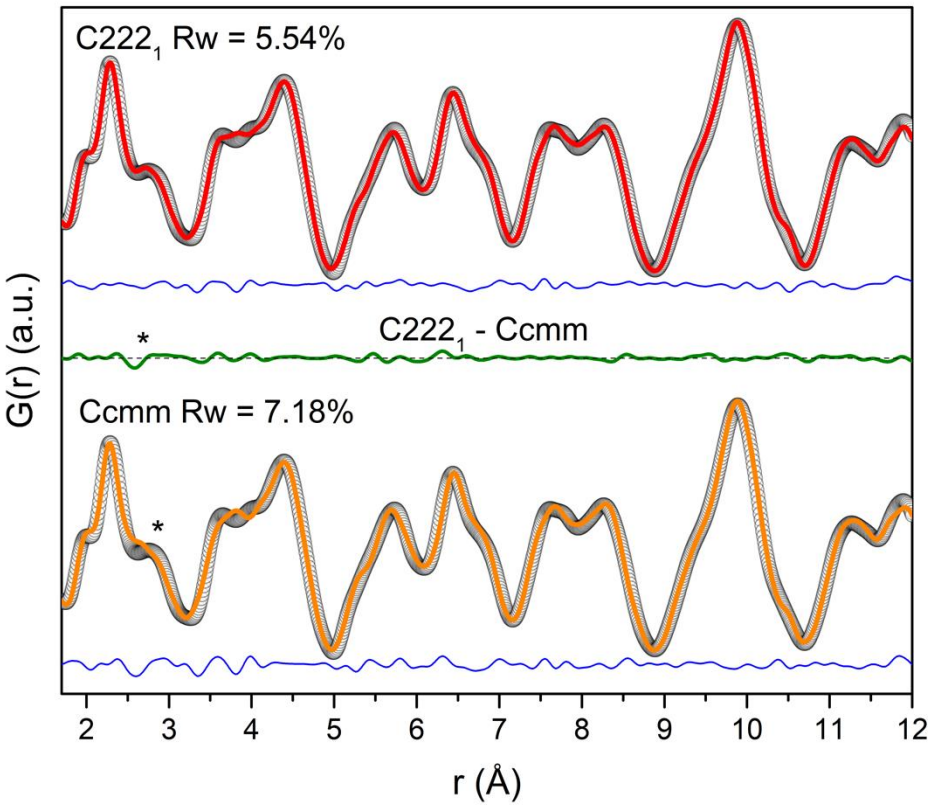

Figure 4.3: Neutron pair distribution functions (PDF) of Y_3TaO_7 modeled with *Ccmm* and *C222$_1$* space groups (bottom and top profiles, respectively). Black circles represent the experimental data and red and orange lines are model fits. The blue lines are difference curves between data and the model and the green line is the relative difference between the *C222$_1$* and *Ccmm* model fits. The asterisk (*) at 2.8 Å in bottom Figure indicates the deviation between experimental data and refinement with the *Ccmm* model.

partial PDFs reveal that the <O-O> interatomic correlations are responsible for the peak in the PDF data around 2.8 Å. The 16*h* Wyckoff oxygen site is too constrained by symmetry in the *Ccmm* structural model to fully capture the pair correlations of the major coordination polyhedra. The <O-O> nearest neighbor correlations in the experimental PDF data are broader and shifted to larger *r*-values (**Figure 4.4**). This is better captured by the $C222_1$ structural model, which allows for less symmetric oxygen arrangement due to the presence of two 8*c* oxygen sites. While overall both structural models fit the data very well across the short-range, this small difference related to the oxygen sublattice indicates that the $C222_1$ structural model is indeed most appropriate for the weberite-type Y_3TaO_7. Only a local probe with high sensitivity to the oxygen sublattice is able to capture the actual atomic arrangement as demonstrated in this study by neutron total scattering utilizing the pair distribution function analysis. Thus, the present neutron total scattering study resolves the discrepancy in literature and confirms the validity of the $C222_1$ structural model from the local atomic arrangement to the long-range behavior. This is also in agreement with physical properties measurements of ordered weberite-type oxides [5], [70]. The occurrence of a second harmonic in laser-related applications can only be understood by distortions of the Ta polyhedron and the absence of an inversion center as required by the $C222_1$ symmetry.

Density functional theory (DFT) modeling was employed to gain further insight into the energetic stability of both orthorhombic structural models for Y_3TaO_7. The DFT results revealed an energy value at 0 K of -207.0408 eV and -207.1525 eV, for *Cmcm* and $C222_1$, respectively. This confirms that the atomic configuration with the lowest energy state for Y_3TaO_7 is best described with the $C222_1$ structural model in agreement to the neutron PDF results. The difference between the cohesive energies at 0K is significant though small enough to consider a possible phase transition to the centrosymmetric structure at high temperature. A comparison of the $C222_1$

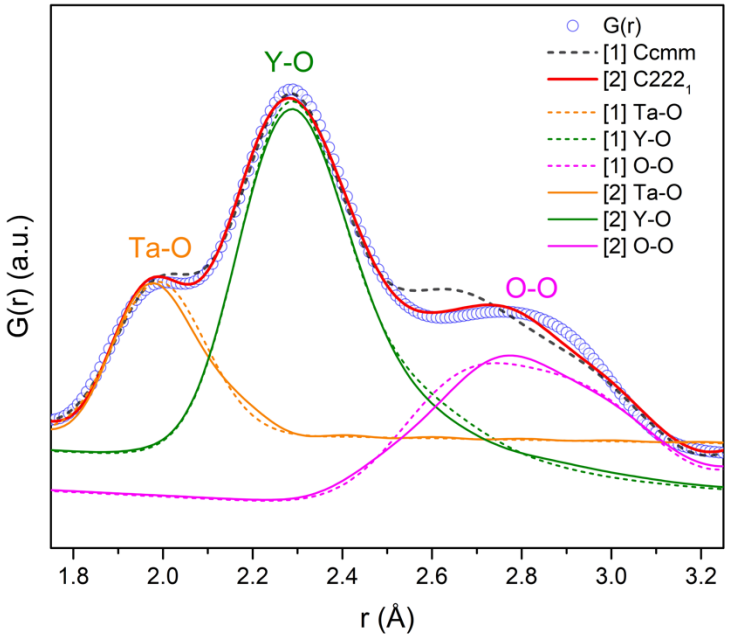

Figure 4.4: Neutron pair distribution function (PDF) of Y_3TaO_7 (blue circles) with refined small-box models using a *Ccmm* (dashed black curve) and a *C222₁* (solid red curve) symmetries. To highlight nearest neighbor bond distances, partial PDFs are shown for both structural model (dashed lines for *Ccmm* and solid line for *C222₁*). Partial PDFs are shifted for the ease of visualization.

structure from DFT modelling and experimental results from small-box analysis reveals small deviations between experiment and simulation. While the backbone of the structure, the 6-coordinated Ta polyhedra, is identical, the 8-coordinated Y polyhedra are slightly shifted against each other within the reference frame. This offset leads to a small difference that is only visible along the [001] in the weberite-type unit cell in the DFT model, which is compensated for by an increased bond distance of the two weakly bound oxygen atoms away from the 8-coordinated cation. This elongates the 8-coordinated polyhedral parallel to [100] and changes their size (larger in the DFT model) inducing a more pronounced zig-zag type pattern of the Y polyhedra in the DFT structure observed along [001].

The small discrepancy between the structural model from DFT calculations and PDF refinements can be explained by the absence of thermal effects in the calculation (performed at 0 K). In addition, the [100] and [001] lattice dimensions are more rigid in terms of electronic structure and the system compensates for any distortion or rotation of polyhedra by adjusting the "soft" dimension of the electronic structure, which is [010] or the b-lattice parameter. (**Figure 4.5**).

4.4 Conclusion

Weberite-type Y_3TaO_7 was investigated using neutron total scattering analysis by the means of Rietveld refinement, small-box modelling and by applying first-principles calculations. Neutron total scattering with high sensitivity to the oxygen sublattice along with simultaneous access to short- and long-range structures identify the $C222_1$ space group as most appropriate structural model. While the long-range structure shows only subtle differences between $C222_1$ and *Ccmm*, the local structure is much better described by the $C222_1$ structural model. The only difference

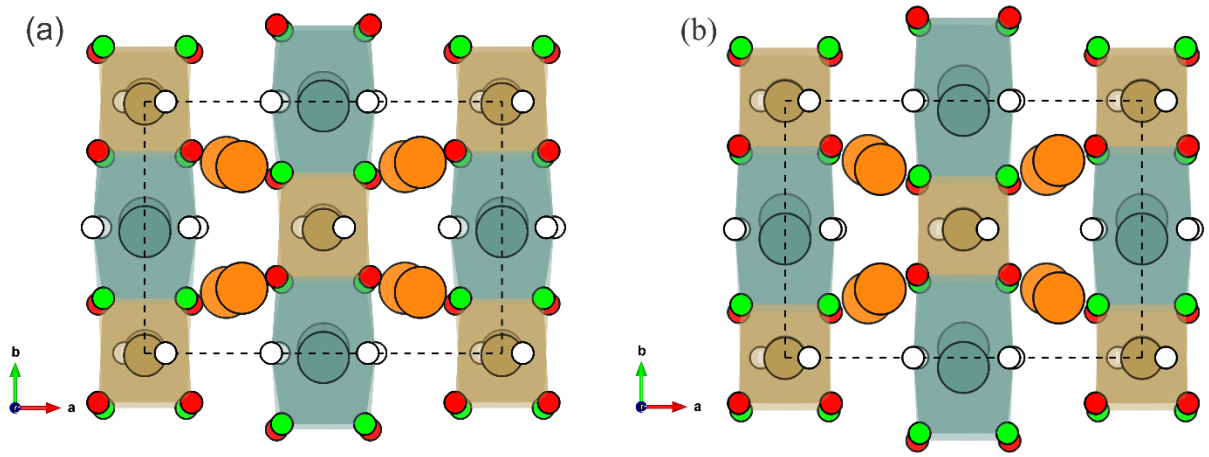

Figure 4.5: Schematic representations of Y_3TaO_7 using a *C222₁* structural model from (a) experimental data *via* small-box refinement and (b) DFT calculations. Yttrium cations are shown as cyan spheres (8-coordinated) or as orange spheres (7-coordinated), while tantalum cations are shown as golden sand spheres. Two 8c oxygen sites are shown as red and green spheres while three 4a oxygen sites are shown as white spheres. Both structural models are shifted by ¼ *c* along [001] for ease of comparison with the *Ccmm* structure. The dashed black line represents the reference cells.

between both orthorhombic structural models is within the local atomic arrangement of the anion sublattice, which is inaccessible by conventional X-ray diffraction experiments. These experimental results are corroborated by DFT calculations that show that the $C222_1$ structural model is energetically more stable (-207.1525 eV) as compared with the *Ccmm* model (-207.0408 eV). These results may also impact the local weberite-type ordering that was recently reported for disordered pyrochlore oxides.

Chapter 5: Systematic study of short- and long-range correlations in RE_3TaO_7 weberite-type compounds by neutron total scattering and X-ray diffraction

This chapter is reproduced with permission from: *Igor M. Gussev, Eric C. O'Quinn, Matthew Tucker, Rodney C. Ewing, Cale Overstreet, Jörg Neuefeind, Michelle Everett, Qiang Zhang, David Sprouster, Daniel Olds, Gianguido Baldinozzi, Maik Lang, "Systematic study of short- and long-range correlations in RE3TaO7 weberite-type compounds by neutron total scattering and X-ray diffraction," J. Mater. Chem. A, pp. 8886–8903, 2023, doi: 10.1039/d3ta01042b.* [45]
Introductory information regarding weberite-type structures is summarized in Chapter 2 while the experimental techniques are summarized in Chapter 3. This work was supported by the U.S. Department of Energy, Office of Science, Basic Energy Sciences, under Award DE-SC0020321. Partial support was provided by the Joint PhD Programme of Université Paris-Saclay as part of the *Investissements d'Avenir* program, grant number ANR-11-IDEX-003. This work was also supported by the U.S. Department of Energy, Office of Science, Basic Energy Sciences, under the SCGSR fellowship program. The SCGSR program is administered by the Oak Ridge Institute for Science and Education for the DOE under contract number DESC0014664. This research used resources at the Spallation Neutron Source, a DOE Office of Science User Facility operated by the Oak Ridge National Laboratory. These experiments and analyses were supported by the U.S. Department of Energy (DOE) Office of Fusion Energy Sciences under Contract No. DE-SC0018322 with the Research Foundation for the State University of New York at Stony Brook. This research used resources at the Pair Distribution Function Beamline of the National Synchrotron Light Source II, a U.S. Department of Energy (DOE) Office of Science User Facility

operated for the DOE Office of Science by Brookhaven National Laboratory under Contract No. DE-SC0012704.

5.1 Abstract

The atomic structures of the lanthanide tantalates, Ln_3TaO_7, series (Ln = Pr, Tb, Dy, Ho, Tm, Yb) were systematically investigated using total scattering techniques. High-energy X-ray and neutron diffraction analysis revealed that the long-range structures can be grouped into three distinct families: (*1*) ordered *Cmcm* (Ln = Pr), (*2*) ordered *Ccmm* (Ln = Tb, Dy, Ho), and (*3*) disordered, defect-fluorite *Fm-3m* (Ln = Ho, Tm, Yb). These findings help to clarify the symmetry discrepancy for the already reported long-range structures in literature. The short-range analysis of neutron total scattering data *via* pair distribution functions reveals a high degree of structural heterogeneity across length scales for all compounds, with distinct local atomic arrangements that are not fully captured by the average, long-range structure. The short-range structures at the level of coordination polyhedra are better captured by a set of alternative non-centrosymmetric structural models: (*1*) *C2cm*, (*2*) $C222_1$, and (*3*) *C2mm*. This establishes a short-range multiferroic character for weberite-type tantalates because ferroelectric interactions compete with magnetic correlations. These ferroelectric interactions are particularly pronounced for the disordered compounds Tm_3TaO_7 and Yb_3TaO_7. The structural differences among the three families are the result of changes in TaO_6 polyhedral tilt (transition between families 1 and 2) and dipolar interactions of off-centered Ta cations (transition between families 2 and 3).

5.2 Introduction

The chemical and structural flexibility of compounds derived from the mineral weberite (Na_2MgAlF_7, *Imma*) [9] displays a diverse array of physical properties, such high ionic conductivity, magnetic ordering, ferroelectricity, and photocatalytic activity [8], [24], [40], [70], [73]–[75]. These properties make weberite-derived compounds of interest for water splitting photocatalysts [29], [75], solid oxide fuel cell electrolytes [26], thermal barrier materials [76], [77], and for applications exploiting their magnetic and dielectric properties [5], [8], [28], [78]. A specific subset of weberite-derived compounds, the $A^{III}{}_3B^{V}O_7$ *weberite-type* oxides [9], exhibit a greater variety of cation environments (allowing broader cation sizes and charge states) with respect to the weberite oxides ($A^{II}{}_2B^{V}{}_2O_7$), as well as to other topologically-related oxides (*e.g.*, $A_2{}^{III}B_2{}^{IV}O_7$ pyrochlore). For this reason, many different structural models have been proposed in the literature [5], [36], [39] for weberite-type oxides making an unambiguous classification of $A^{III}{}_3B^{V}O_7$ compounds into different structural families challenging.

The structures of A_3BO_7 weberite-type oxides (where A = lanthanide, B = Ta, Nb, Sb) [79],[80] are related to the fluorite structure and are generally best described by an orthorhombic supercell with unit-cell parameters $2a_F, \sqrt{2}a_F, \sqrt{2}a_F$. Initially, structures such as weberite, disordered fluorite, and disordered pyrochlore [79] were proposed for weberite-type compounds based on laboratory diffraction experiments (X-rays and/or electrons). Later, a comprehensive study was performed by Allpress *et al.*, who proposed, based on X-ray diffraction and selected-area electron diffraction (SAED) experiments [5], [36], [38], [39], three distinct structure types for describing weberite-type oxides with different chemical composition. Allpress *et al.* proposed that the size of the A-site lanthanide cation influences their final symmetry, as trivalent lanthanides exhibit a monotonic contraction of ionic radius with increasing atomic number. Results from X-

ray diffraction experiments (in some cases revealed by SAED) [36],[37] were used to assign *Cmcm* (space group 63) to compounds with larger lanthanides (*e.g.*, La_3TaO_7, La_3NbO_7, La_3SbO_7, and Nd_3NbO_7), the *C222₁* (space group 20) to lanthanides with intermediate-sized ionic radius (*e.g.*, Gd_3TaO_7, Gd_3NbO_7, and Ho_3TaO_7), and the *Fm-3m* (space group 225) to compounds with smaller lanthanide cations (*e.g.*, Er_3NbO_7 and Er_3TaO_7). For the smaller lanthanide compounds, no supercell diffraction maxima were observed, and their diffraction patterns corresponded to a disordered, defect-fluorite structure with randomly distributed anion vacancies and random cation occupancy across the two available sites [36]. Finally, weberite-type oxides at phase boundaries between structure types can exhibit different structures depending on the thermal history and temperature conditions during data collection [40]. For example, according to Wakeshima *et al.*, compounds with intermediate sized cations, such as Ho_3TaO_7, display a *C222₁* symmetry after prolonged annealing at 1673 K or a *Fm-3m* symmetry after annealing at 1973 K [5]. Similarly, Nd_3TaO_7 displays two polymorphs at room temperature, a mixture of *Cmcm* and *C222₁* phases, that transform into a single *C222₁* phase at higher temperature [5],[36] .

After those seminal studies, other research groups have investigated the structure of several weberite-type oxides mostly belonging to the initially assigned *C222₁* space group (intermediate-sized lanthanides, *e.g.*, Sm_3TaO_7 – Ho_3TaO_7 and Y_3TaO_7), though alternative structural models were sometimes proposed [39]. The motivation for this reassessment was based on previously overlooked weak diffraction maxima, hardly detected in XRD patterns measured with laboratory diffractometer, but disagreeing with the selection rules of the *C222₁* symmetry. Space groups with mutually incompatible selection rules, such as *Cmcm* (or an alternative *Ccmm*, 63), *C222₁* (20), *Cmmm* (65), *Amm2* (38), *Cmm2* (35), and *C222* (21), were proposed for some of these compounds [5], [36], [38], [39]. The fact that so many different space groups have been proposed can be

explained by large uncertainties of refinements resulting from weak and overlapping peaks of powder diffraction data.

Looking in perspective to the set of proposed space groups, common trends emerge for ordered weberite-type tantalates, as these structures share similar structural motifs. The 6-coordinated B-site cations (Ta) form rigid TaO_6 octahedra, while A-site cations (Ln, Y) occupy two distinct polyhedra: AO_8 and AO_7 distorted cubes. In case of AO_7 polyhedra, one of the fluorite oxygen atoms is replaced by a vacancy. The TaO_6 octahedra share one corner with each other and form infinite chains projected along one of the shorter orthorhombic directions, typically the *c*-lattice parameter [001]. AO_8 distorted cubes share edges and form chains also parallel to [001]. These two chains form layers parallel to (100) with layers made of distorted AO_7 cubes between them (**Figure 5.1 b and c**). While the weberite-type structure is complex, it is constrained by the orthorhombic *c*-lattice parameter, which is a function of the size and tilt of the octahedra. This in turn imposes geometric constraints upon the other polyhedra, leading to distortions in most of the weberite-type compounds. All structural models proposed in literature for orthorhombic weberite-type compounds contain the same polyhedra arrangements with specific distortions: the main difference between them is the orientation of the tilt axis of the BO_6 octahedra. Indeed, *Cmcm* structures have a [010] tilt system, as shown in **Figure 5.1(*b*),** while *Ccmm* (or $C222_1$) structures have a [100] tilt system, as shown in **Figure 5.1(*c*)**. For the reader's convenience, we will refer to these structure types as ordered weberite-type families 1 and 2, respectively rather than by the actual space group definitions.

In this paper, we have used state-of-the-art spallation neutron and synchrotron X-ray scattering techniques to gain detailed insight into the structural complexity of weberite-type oxides that arises from proposed incompatible structural models and symmetries. Weberite-type tantalates

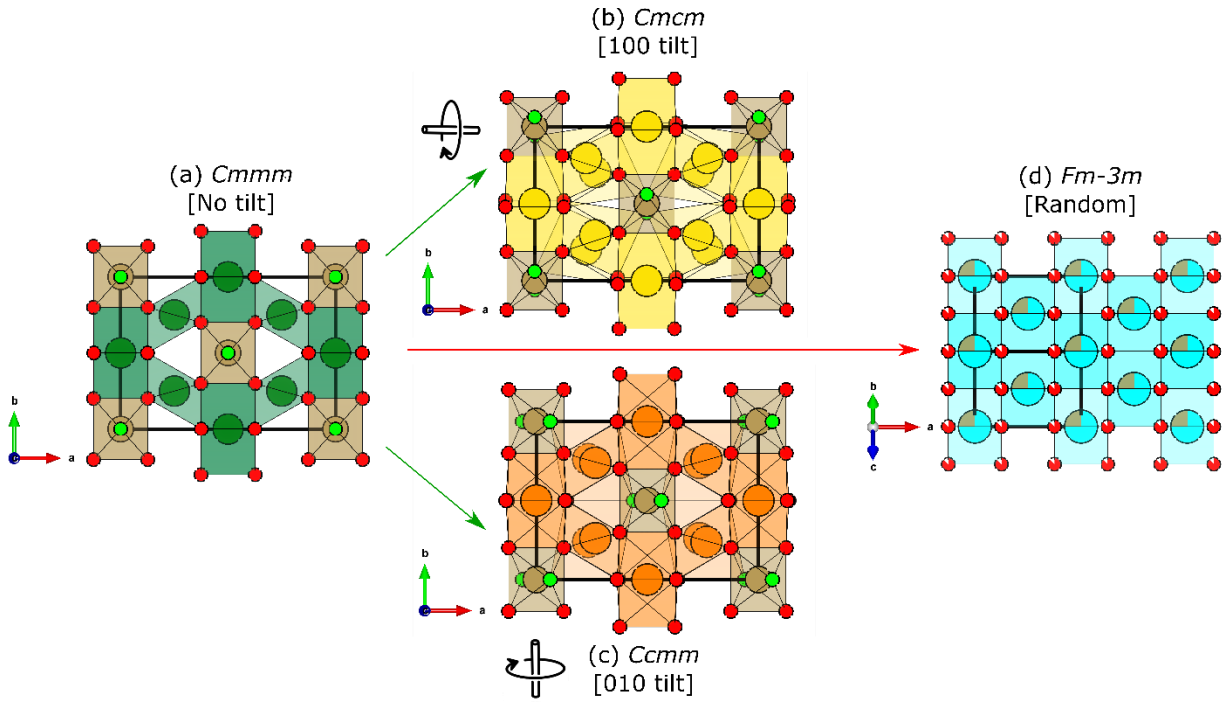

Figure 5.1: Relations among the three structural families of A_3TaO_7 weberite-type oxides (*b*,*c*,*d*). The structures are shown with the relation to the single c-layer parent prototype structure. Thick solid black lines represent the respective unit cells. (*a*) *Cmmm* prototype model with A-site cations shown as green spheres, (*b*) *Cmcm* structural model with large radii A-site cations shown as yellow spheres, (*c*) *Ccmm* structural model with medium radii A-site cations shown as orange spheres and (*d*) *Fm-3m* structural model with small radii A-site cations shown as cyan spheres. Oxygen anions and Ta cations are shown in all four structures as red and brown spheres, respectively. Oxygen anions highlighted as smaller lime green spheres and displaced according to different tilt systems. The tilt systems of the (*a*) single layer *Cmmm* prototype structure produce either the bilayer structure (*b*) *Cmcm* with [100] tilt, or the (*c*) *Ccmm* with [010] tilt, as represented by black loops around the rotation axes. The white sectors within red spheres in (*d*) denote the partial occupancy of oxygen sites in the *Fm-3m* model, and mixed brown/cyan spheres represents a randomization of cations across cation sites. All coordination polyhedra are shown according to the color of their respective cations. Structures are projected along their conventional directions: (*a*,*b*,*c*) along $[001]_W$ and (*d*) $[011]_F$ with W and F subscripts denoting the weberite-type and defect-fluorite lattices, respectively.

covering a large range of lanthanide cation with different structures were synthesized and investigated across the long-range structure by means of combined neutron and X-ray diffraction experiments. The short-range structure was characterized *via* pair distribution analysis to describe the atomic arrangement and coordination polyhedra within the different long-range structures. This comprehensive analytical approach with high sensitivity to both the cation and anion positions provides a more unified description of the three structural families of weberite-type tantalates across different length scales.

5.3 Results

5.3.1 Analytical derivation of the weberite-type structure

Before experimental data are presented, general aspects of the weberite-type structures are assessed, which will help to contextualize and better interpret the results presented in this study. In weberite-type tantalate oxides, the charge difference between the two cations (Ln^{+3} and Ta^{+5}) can favor long-range order, with both cations and anions at specific crystallographic sites. This defines a specific bonding environment resulting in a repeating configuration of four different coordination polyhedra: (*i*) an octahedron, formed by the pentavalent Ta cation, (*ii*) and (*iii*) two sevenfold-coordinated polyhedra, occupied by the rare-earth or lanthanide cations, typically in form of a mono-capped octahedral configuration, and (*iv*) an eightfold-coordinated distorted cube, occupied by the lanthanide cation. Moving across the Ln^{3+} series from Pr to Yb, the size of the lanthanide ions contract, which influences the tilt and deformation modes of the stiffer Ta-octahedron, leading to structural changes in the other three more flexible Ln-polyhedra. For the smallest lanthanide cations, these changes lead eventually to a loss of the long-range order, folding the orthorhombic weberite-type structure into a disordered, defect-fluorite structure. In this

disordered structure, the two cations randomly occupy a shared cation site; whereas, the oxygen vacancy is statistically distributed onto the anion sites. However, recent results on weberite-type oxides with the defect-fluorite structure [20] and structurally-related pyrochlore oxides suggest that short-range ordered correlations persist within such disordered compounds that are distinct from the average long-range structure [13], [15], [17], [18], [46]. In contrast, ordered weberite-type Ln_3TaO_7 oxides exhibit small distortions with respect to the parent fluorite structure, leading to an orthorhombic lattice with pseudo-tetragonal characteristics. To simplify the presentation of the results, a unique reference lattice is defined, assuming $a_W = 2a_F$ and $b_W \approx c_W \approx a_F\sqrt{2}$, with "*W*" and "*F*" subscripts referring to weberite and fluorite lattices, respectively. This orientation convention is not always adopted in previous studies, but it aids in discussing and comparing the structural changes across all weberite-type oxides. In this reference frame, a set of two Ta octahedra form corner-sharing chains along the *c*-axis. As a result, half of the distorted octahedra tilt clockwise around either the a_W or the b_W axes, while the other half in the next atomic layer tilts counterclockwise. The extent of the octahedron distortion and the actual tilt axis determine the overall length of the c_W-axis parameter and the final symmetry of the space group.

As described before, three main space groups have been defined previously to describe the structures of Ln_3TaO_7 weberite-type tantalates: *Cmcm*, *Ccmm* (*or* $C222_1$), and *Fm-3m* (**Figure 5.1b, c**). The use of these different structural models can be rationalized based on a prototype 'parent' structure, for which tilts and distortions are removed. This prototype (P) structure (**Figure 5.1a**), which is described in detail in **Table 5.1**, has a *Cmmm* (65) symmetry with a *c*-lattice parameter that is halved as compared with that of the C-centered weberite-type structures ($a_P = a_W$, $b_P = b_W$, and $c_P = ½\ c_W$).

Table 5.1: Starting values for the Ln_3TaO_7 weberite-type prototype *Cmmm* (65) structure.

Ln_3TbO_7		**a (Å)**	**b (Å)**	**c (Å)**
Cmmm		10.49940	7.42422	3.71211
Atom	**Wyckoff Site**	**x**	**y**	**z**
Ta1	2a	0	0	0
Ln1	2b	0	0.5	0
Ln2	4f	0.25	0.25	0.5
O1	8p	0.37388	0.29953	0
O2	2d	0	0	0.5
O3	4h	0.125	0.5	0.5

The most common structural models proposed in the literature for niobates and tantalates weberite-type compounds can be derived using mechanical instabilities of the irreducible representations at the Y, T, and Z points of the centered orthorhombic Brillouin zone of the prototype weberite structure. All structures of the Ta-based compounds reported in literature can be obtained systematically by considering Z-point irreducible representations. The most symmetric structural models belonging to these 8 irreducible representations are described by four centrosymmetric space groups, each one with two distinct origins: Z_1^+, Z_2^- lead to *Cmmm* (65), Z_2^+, Z_1^- to *Cccm* (66), Z_3^+, Z_4^- to *Cmcm* (63), and Z_4^+, Z_3^- to *Ccmm* (63). Eventually, these space group symmetries can be further reduced if specific peaks in the diffraction patterns provide the required evidence. For instance, suppression of the inversion center in either *Ccmm* or *Cmcm* yields the *C222₁* symmetry. The different space groups are characterized by distinct supercell peaks, which can be compared with high quality diffraction data to identify the most appropriate model for any particular compound.

5.3.2 Long-range structural analysis

High-energy synchrotron X-ray (SXRD) diffraction data were collected for the ordered, orthorhombic Pr_3TaO_7, Dy_3TaO_7 and Ho_3TaO_7 samples and refined using structural models previously reported in literature [5], [36], [39] (*Cmcm* for Pr_3TaO_7; *Ccmm* or Dy_3TaO_7 and Ho_3TaO_7, (**Figure 5.2a**). All refinements provided reasonable fits as demonstrated by the difference curves and acceptable reliability factor (*Rw*) parameters. Only the refinement of the Pr_3TaO_7 diffraction pattern resulted in a slightly larger *Rw*, which can be explained by the presence of a minor impurity phase (less than 3% of $PrTaO_4$). No impurities were detected in the XRD patterns of Ho_3TaO_7 and Dy_3TaO_7. Inspection of the low-*Q*/high *d*-spacing part of the diffraction

patterns is critical for establishing the correct space group for the different weberite-type compounds. This region is very sensitive to site occupancy and atomic order, which produces separate peaks in the synchrotron X-ray and neutron diffraction patterns. Of particular importance is the presence, or absence, of *0kl* and *h0l* peaks: (*e0o*) like (201), (401), or (403) are allowed by *Ccmm* and forbidden for *Cmcm*; *vice versa*, (*0eo*) like (021), (041), (043) are allowed by *Cmcm* and forbidden for *Ccmm*. If the peaks of both sets are observed in the diffraction patterns, the inversion center is suppressed. This was experimentally demonstrated for the structure of the rare-earth compound Y_3TaO_7 [46], described by the $C222_1$ space group. While not being part of this study on lanthanide tantalate compounds, we have re-measured this sample [46] under identical high-energy SXRD conditions as reference data set to compare with the ordered weberite-type lanthanide compounds (**Figure 5.2b**).

Inspection of the low-*Q* region (**Figure 5.2b**) clearly shows that Pr_3TaO_7 exhibits a (021) diffraction maximum at ~1.85 $Å^{-1}$, while the (201) peak is absent. This agrees with the crystallographic rules of the *Cmcm* space group, which confirms that this structural model reported in literature is indeed the most symmetrical one for Pr_3TaO_7 and potentially for all the other members of structural family 1. Rietveld refinement with the *Cmcm* space group yields excellent agreement to the XRD data for Pr_3TaO_7 (*Rw* = 3.359%). The extinction rules are reversed for *Ccmm* and the low-*Q* diffraction regions of Ho_3TaO_7 and Dy_3TaO_7 of structural family 2 (**Figure 5.2b**); (201) peaks are observed at ~1.48 $Å^{-1}$, whereas (021) peaks are not observed at ~1.83 $Å^{-1}$. This agrees with the proposed *Ccmm* space group by Fu *et al.* for Sm_3TaO_7 [39], a compound of the same structural family. Refinement of the measured SXRD patterns of Ho_3TaO_7 and Dy_3TaO_7 with this *Ccmm* space group provides excellent agreement with very low *Rw* of 2.409% and 2.691%, respectively, confirming the choice of this highly symmetrical space group. The

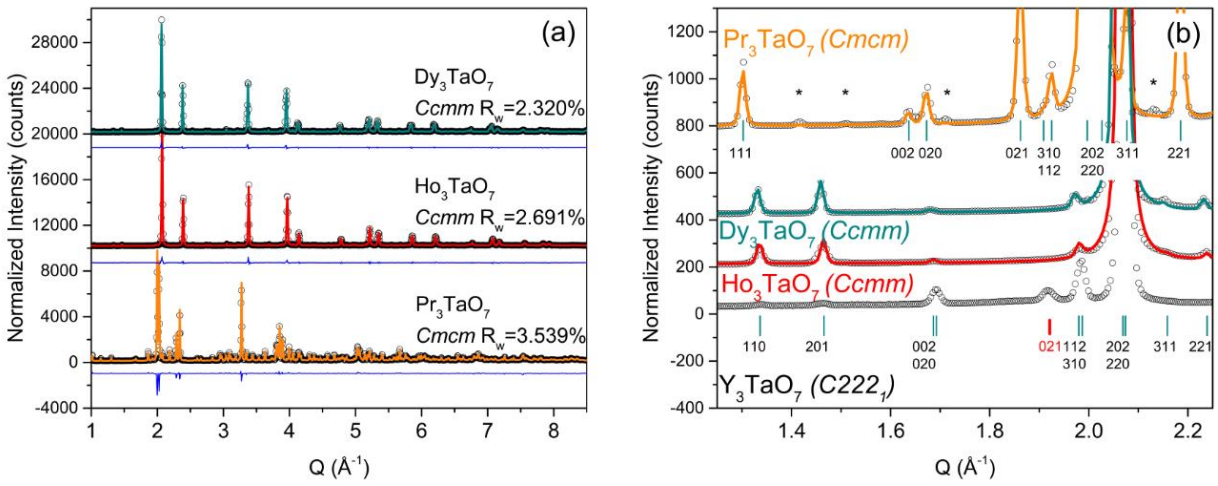

Figure 5.2: (a) Stacked high-energy synchrotron X-ray diffraction patterns for A_3TaO_7 (A = Pr, Dy, Ho) as measured (black circles) and modeled (orange, cyan and red curves). Blue curves represent the difference between measurement and calculated model (space groups *Cmcm* and *Ccmm*). The reliability factor (*Rw*) is reported for every sample. Diffraction patterns are offset by values of 10'000 and 20'000 respectively. (b) Expanded view of the low-Q range of (a) using the same color labeling, along with diffraction data of Y_3TaO_7 (black circles), which serves as reference measurement. Cyan ticks represent diffraction conditions allowed in (top) *Cmcm* and (bottom) *Ccmm* space groups. Asterisks (*) mark the $PrTaO_4$ impurity phase reflections for Pr_3TaO_7. The red tick mark at ~1.93 $Å^{-1}$ indicates the location of the (021) diffraction peak, which serves as space group distinction between $C222_1$ and *Ccmm* (and it is only allowed for $C222_1$). Diffraction patterns are offset by values of 200, 400 and 800 respectively.

centrosymmetric nature of this space group is further corroborated by the reported absence of any second harmonic generation signal at room temperature, as described by Astafyev *et al.* [41] for Ln_3TaO_7 (Ln = Sm-Gd). Therefore, it is reasonable to expect that the *Ccmm* space group is the common representation for all structural family 2 compounds. On the other hand, the $C222_1$ symmetry is confirmed by the existence of (201) and (021) peaks in Y_3TaO_7 (**Figure 5.2b**), and this compound can no longer be considered as the room temperature structural model for the long-range structures of family 2 weberite-type tantalates.

Rietveld refinement of the high-resolution time-of-flight neutron diffraction patterns (POWGEN) with high sensitivity to the oxygen positions yielded a good agreement with the *Cmcm* model (Rw_1 = 2.501% and Rw_2 = 4.769%) for Pr_3TaO_7 **(Figure 5.3)** and the *Ccmm* model (Rw_1 = 4.940% and Rw_2 = 4.770%) for ordered Ho_3TaO_7 (**Figure 5.4**).

The amount of $PrTaO_4$ impurity phase in Pr_3TaO_7 was 1.7%, and neutron characterization did not reveal any impurity phases in Ho_3TaO_7. In agreement with the SXRD results, the time-of-flight neutron diffraction results also show strong evidence of the (021) peak for Pr_3TaO_7 with no apparent signal of the (201) peak; whereas, Ho_3TaO_7 shows a pronounced (201) peak. The absence of the (021) peak (expected at ~1.92 Å in *Q*-space or ~3.3 Å in *d*-space) confirms the centrosymmetric *Ccmm* model for Ho_3TaO_7 (**Figure 5.5**). The diffraction pattern of Ho_3TaO_7 measured at 100 K with reduced effect of thermal vibrations show the same structural behavior and supports this conclusion (**Figure 5.6**).

Neutron diffraction patterns of A_3TaO_7 (A=Pr, Tb, Ho, Tm, and Yb) collected at NOMAD revealed three distinct structures across the lanthanide series (**Figure 5.7**). Rietveld refinement confirms that these patterns belong to the three distinct structural families of weberite-type tantalates. The NOMAD diffraction patterns (**Figure 5.7**) are in good agreement with SXRD and

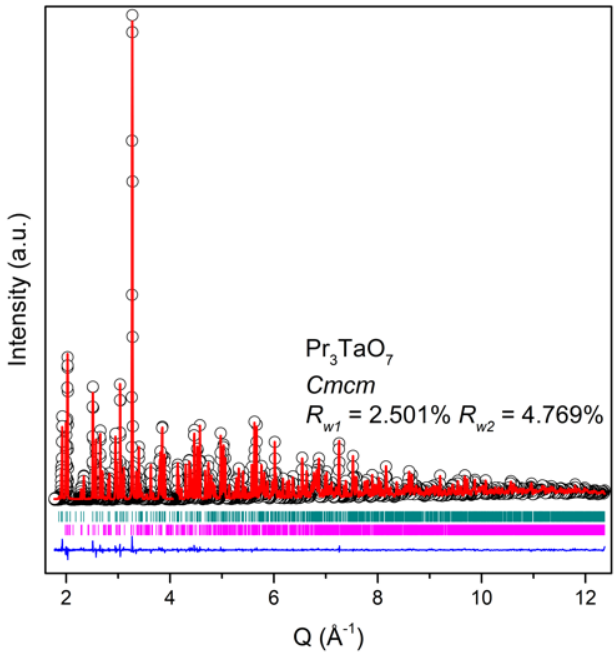

Figure 5.3: POWGEN' high-resolution neutron diffraction pattern of Pr_3TaO_7 measured at room temperature (black circles) and modeled (red curve) using *Cmcm* space group. The blue curve represents the difference curve between measurement and the model fit, with R_{w1} and R_{w2} being the fit reliability factors. Cyan and magenta ticks indicate the expected Bragg peak positions according to the crystal structure models of Pr_3TaO_7 and $PrTaO_4$ impurity phase, respectively.

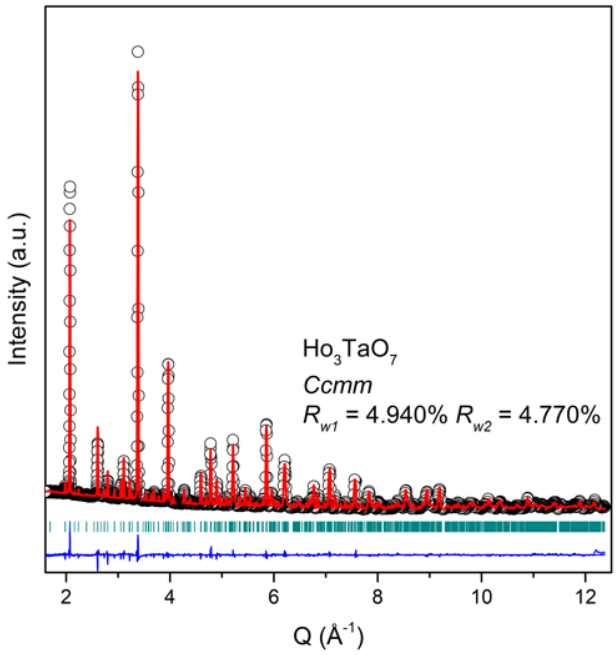

Figure 5.4: POWGEN' high-resolution neutron diffraction pattern of Ho_3TaO_7 measured at room temperature (black circles) and modeled (red curve) using *Ccmm* space group. The blue curve represents the difference curve between measurement and the model fit, with Rw_1 and Rw_2 being the fit reliability factors. Cyan ticks indicate the expected Bragg peak positions according to the crystal structure model.

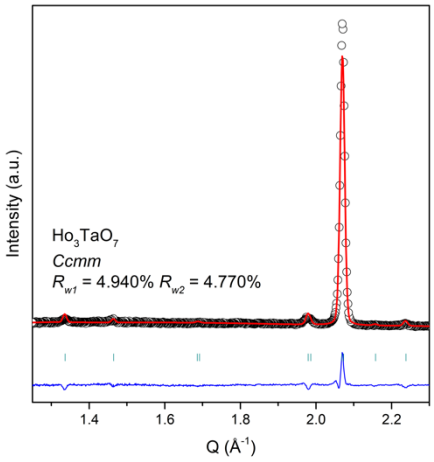

Figure 5.5: An expanded view of low-Q region of POWGEN' high-resolution neutron diffraction pattern of Ho_3TaO_7 measured at room temperature (black circles) and modeled (red curve) using *Ccmm* space group. The blue curve represents the difference curve between measurement and the model fit, with Rw_1 and Rw_2 being the fit reliability factors. Cyan ticks indicate the expected Bragg peak positions according to the crystal structure model.

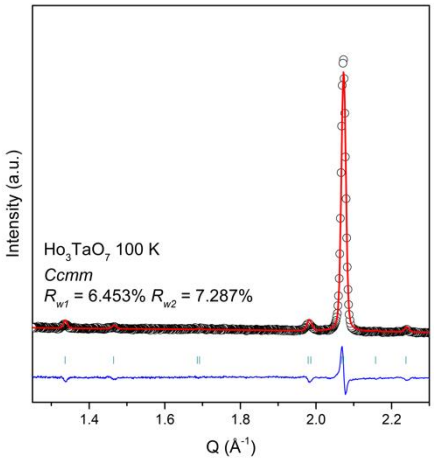

Figure 5.6: Low-Q region of POWGEN' high-resolution neutron diffraction pattern of Ho_3TaO_7 measured at 100 K (black circles) and modeled (red curve) using *Ccmm* space group. The blue curve represents the difference curve between measurement and the model fit, with Rw_1 and Rw_2 being the fit reliability factors. Cyan ticks indicate the expected Bragg peak positions according to the crystal structure model.

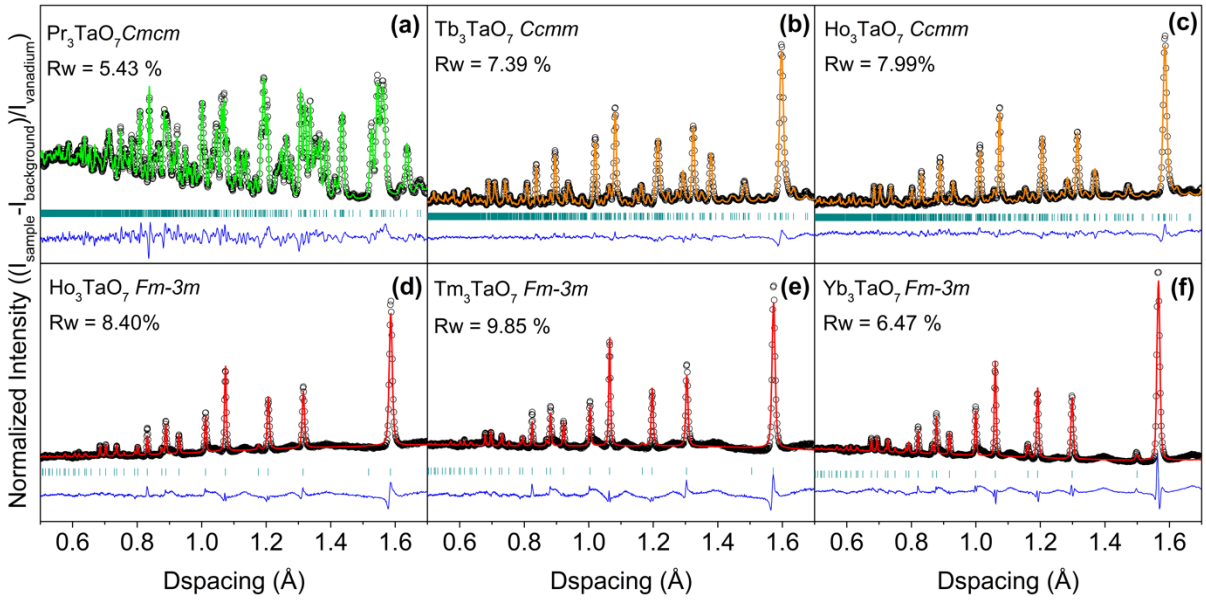

Figure 5.7: Neutron diffraction patterns of A_3TaO_7 (A=Pr, Tb, Ho, Tm, and Yb) measured at NOMAD's detector bank 4. The experimental data (shown as black circles) were refined using small-box modeling based on the following space groups: (**a**) *Cmcm* (green curve), (**b,c**) *Ccmm* (amber curve) and (**d,e,f**) *Fm-3m* (red curve). The blue curves are the difference between experimental data and calculated models. *Rw* values are reported for each refinement.

POWGEN data obtained for the two ordered families. Family 1 is described by the orthorhombic *Cmcm* model (Pr_3TaO_7, *Rw* = 5.43%) and family 2 by the orthorhombic *Ccmm* model (Tb_3TaO_7 and Ho_3TaO_7 synthesized at 1673 K with *Rw* = 7.39% and 7.99%, respectively). As already reported in the literature [5], [20], structural family 3 of disordered weberite-type tantalates is described by the defect-fluorite (*Fm-3m*) space group: disordered Ho_3TaO_7 synthesized at 1973 K, Tm_3TaO_7, and Yb_3TaO_7 , with *Rw* = 8.40%, 9.85% and 6.47%, respectively. The Pr_3TaO_7 refinement is the best in terms of cumulative *Rw* value among all samples, despite the minor impurity phase. In the disordered, defect-fluorite compounds, the orthorhombic superstructure peaks, characteristic of the weberite-type ordering, are only detectable as a weak and broad diffuse scattering signal, which carries information about specific short-range atomic correlations. These were analyzed in real space using pair distribution functions (PDFs) to obtain valuable insight into the atomic-scale structure of the different weberite-type oxides.

5.3.3 Short-range structural analysis

Analysis based on long-range derived structural models

High-resolution PDF data of all samples are shown in **Figure 5.8** over a *r*-range between about 2 Å and 11 Å. The peak positions are characteristic of specific atomic-pair correlations (sometimes leading to several unresolved contributions within one peak), the area under the peak depends on the coordination number, and the width is related to the spread of the interatomic distances that increases with the displacive disorder in the system. The PDFs across the sample series show variations in peak intensities and widths and, as a first step, the long-range structural models from diffraction data (**Figure 5.7**) were used for small-box modeling: *Cmcm* for weberite- type

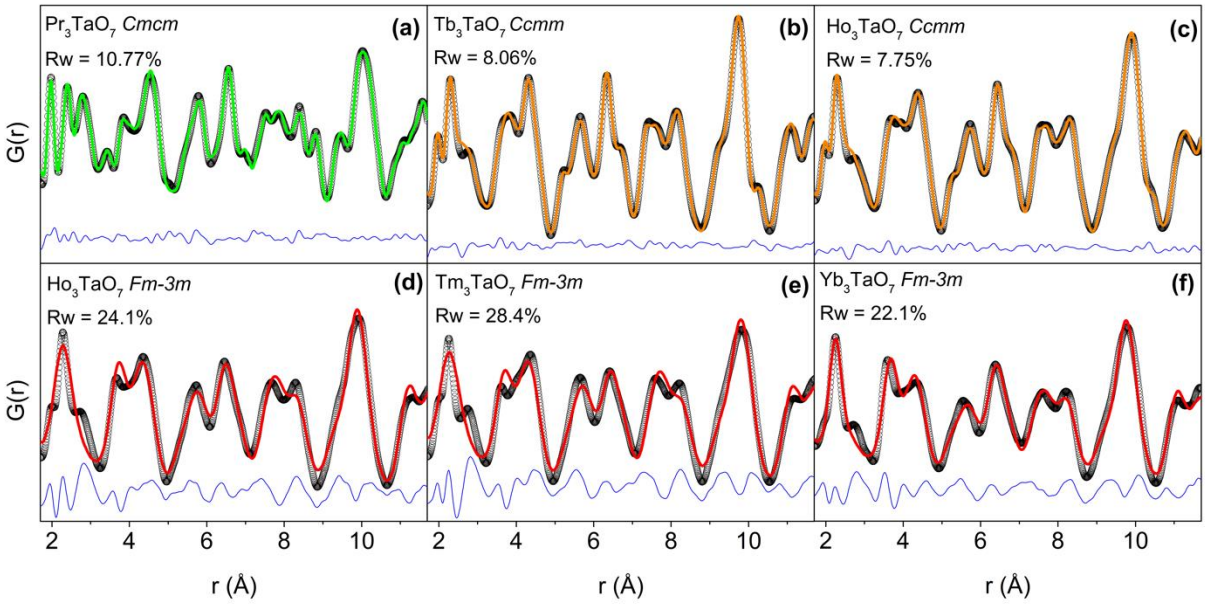

Figure 5.8: Neutron pair distribution functions (PDFs) of Ln_3TaO_7 (Ln=Pr, Tb, Ho, Tm, and Yb). Data (black circles) obtained at room temperature and modelled with long-range derived structural models (green, amber, and red curves for each family) using (**a**) *Cmcm*, (**b, c**) *Ccmm* and (**d, e, f**) *Fm-3m* space groups, respectively. The blue curves are the difference between the experimental data and the small-box refinement calculated models. *Rw* values are reported for each refinement.

compounds with large lanthanides, *Ccmm* for the medium-sized lanthanides, and *Fm-3m* for small lanthanides (**Figure 5.8**). All ordered orthorhombic models (either *Cmcm* or *Ccmm*) provide a reasonably good agreement with the experimental data (Pr_3TaO_7, Tb_3TaO_7, and long-range ordered Ho_3TaO_7, with *Rw* values typically less than 10%). However, refinement of long-range disordered Ho_3TaO_7, Tm_3TaO_7, and Yb_3TaO_7 with the *Fm-3m* defect-fluorite model resulted in an extremely poor fit quality (*Rw* values well above 20%) (**Figure 5.8**), which motivates further detailed analysis of the short-range structure, as discussed later in this section.

Small-box analysis of weberite-type compositions with larger and medium sized lanthanides (ordered, orthorhombic structural families)

The previously reported *Cmcm* and *Ccmm* models, which described well the corresponding long-range structures of the ordered weberite-type samples, also provide a reasonably good agreement for the short-range data as expressed by the reasonably low *Rw* values. There was no strong dependence of the *Rw* values on the spatial range considered for these small-box refinements. However, there are certain PDF sections, particularly at ~2.9 Å, sensitive to O-O correlations in Tb_3TaO_7 and Ho_3TaO_7 (**Figure 5.9**, asterisk markers), that evidence systematic discrepancies between experiment and model. A similar behavior has been previously reported for weberite-type Y_3TaO_7, and changes in these O-O correlations were instrumental to the assignment of $C222_1$ symmetry [46]. On the other hand, there is no obvious localized systematic discrepancy between data and refinement for Pr_3TaO_7 (**Figure 5.9a**), but the *Rw* value is still somewhat higher than expected.

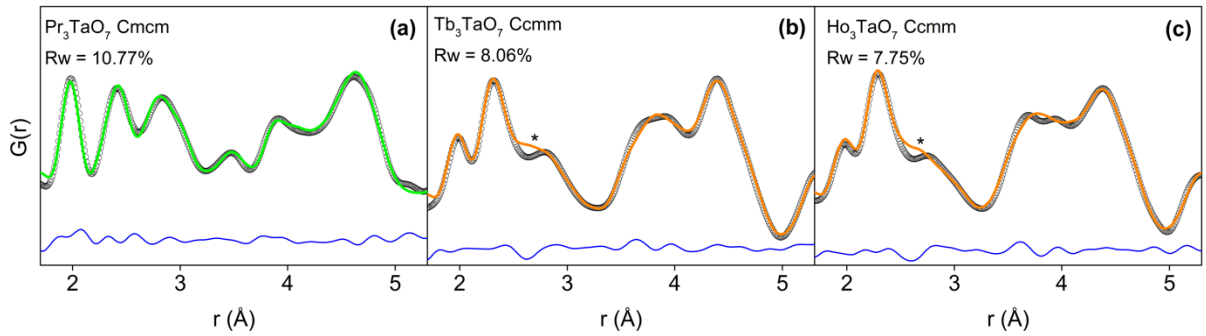

Figure 5.9: Enlarged view of the neutron PDFs of Figure 5.8 covering the very local *r*-range (1.7-5.3 Å) where 1st and 2nd nearest neighbor correlations are observed in ordered weberite-type A_3TaO_7 (A=Pr, Tb, Ho) with (**a**) *Cmcm* and (**b, c**) *Ccmm* space group models, respectively. Black circles represent the experimental data and red lines are the refined models. The blue lines are the difference curves between data and the small-box refinements. *Rw* values are reported. Asterisk symbols (*) highlight the O-O correlation misfit of the *Ccmm* model at ~2.8 Å for Tb_3TaO_7 and Ho_3TaO_7.

To improve the small-box PDF refinement, a set of alternative symmetries were employed to improve the description of the displacive distortions affecting the O-O pair correlations. The approach was to systematically explore the subgroup structures deduced from the Brillouin zone center (Γ) irreducible representations of the respective *Cmcm* and *Ccmm* space groups corresponding to the long-range structures of weberite families 1 and 2, respectively. Seven additional structural models were derived for each space group. For the *Cmcm* model (Pr_3TaO_7, [100] tilt), the order parameter of the 8 irreducible representations (Γ) lead to the following space groups: *Cmcm* (63, (a, b, c), Γ_1^+), *P2₁/m* (11, unique axis c, Γ_2^+), *C2/m* (12, unique axis a, Γ_3^+) and *C2/c* (15, unique axis b, Γ_4^+), which are centrosymmetric, and the four non-centrosymmetric *C222₁* (20, (a, b, c), Γ_1^-), *Cmc2₁* (36, (a,b,c), Γ_2^-), *C2cm* (40, (-c, b, a), Γ_3^-), *Cm2m* (38, (b, c, a), Γ_4^-). For the *Ccmm* model (ordered Ho_3TaO_7, [010] tilt), the tested Γ-point space groups were: *Ccmm* (63, (b, a, -c), Γ_1^+), *P2₁/m* (11, unique axis b, Γ_2^+), *C2/m* (12, unique axis b, Γ_3^+) and *C2/c* (15, unique axis a, Γ_4^+) and the non-centrosymmetric counterparts *C222₁* (20, (b, a, -c), Γ_1^-), *Ccm2₁* (36, (b, a, -c), Γ_2^-), *Cc2m* (40, (b, c, a), Γ_3^-), *C2mm* (38, (-c, b, a), Γ_4^-). Initially, to provide the best model selectivity, the structural analyses were performed on Pr_3TaO_7 and ordered Ho_3TaO_7 measured at 100 K. Indeed, the low-temperature measurement greatly reduced the effect of thermal smearing and improved the positional parameter analysis for each compound representative of families 1 and 2 tilt systems. The quality of the fit for each model was evaluated by two criteria: *(i)* the conventional *Rw* value (Eq. 3.2) and *(ii)* the correlated *Gs*-value (Eq. 3.3), which 'penalizes' correlated errors of the difference curve, apart from purely stochastic deviations. The most accurate model is the one with the lowest *Rw* value and with the least correlated difference curve, particularly within the low-*r* PDF section sensitive to 1st and 2nd nearest neighbor correlations.

The results of this detailed PDF analysis with refinements based on these eight models are shown in **Figure 5.10** for Pr_3TaO_7 measured at 100 K. Qualitative inspection shows that most models describe the local structure of Pr_3TaO_7 quite well (**Figure 5.10a**), though some space group choices lead to unstable refinements and to an increased *Rw*.

These models were rejected as unsuitable. *Rw* values reveal that non-centrosymmetric models ($\Gamma_{1\text{-}4}^-$) generally produce slightly better fits to the neutron PDF data as compared with centrosymmetric models ($\Gamma_{1\text{-}4}^+$), including the long-range *Cmcm* model, in particular. This reliability factor analysis favors in the *r*-range of 1.5 – 12 Å especially the *Cmc2₁* (Γ_2-), *C2cm* (Γ_3-), *Cm2m* (Γ_4-), *C2/c* (Γ_4+), and marginally *C222₁* (Γ_1-) models with *Rw* values close to 8%. The analysis of the correlated reliability factor *Gs* also demonstrates that non-centrosymmetric models are preferable as they generally have smaller *Gs*-values, indicative of reduced systematic errors.

Considering both *Rw* and *Gs* criteria, this reduces the initial eight possible choices for the [100] tilt system to the models Γ_3^- (*C2cm*) and Γ_4^- (*Cm2m*). Providing similar agreement, both models were judged based on their number of refined parameters, which were 49 and 54, respectively. Thus, Γ_3^- (*C2cm*) is the preferred description of the coordination polyhedra environment and the best fit to the short-range structure of Pr_3TaO_7. This is supported by the evolution of the difference curve (**Figure 5.10b**), which exhibits only uncorrelated intensity fluctuations, specifically in the *r*-range significant for the critical O-O correlations (2.5 – 3 Å, shaded region in **Figure 5.10b**).

The same systematic PDF refinement procedure was also applied to Ho_3TaO_7 measured at 100 K (**Figure 5.11**). All models provided reasonable fits. The *Ccmm* structural model used for the long-range diffraction data produced the largest *Rw* value; therefore, it is not a good choice for

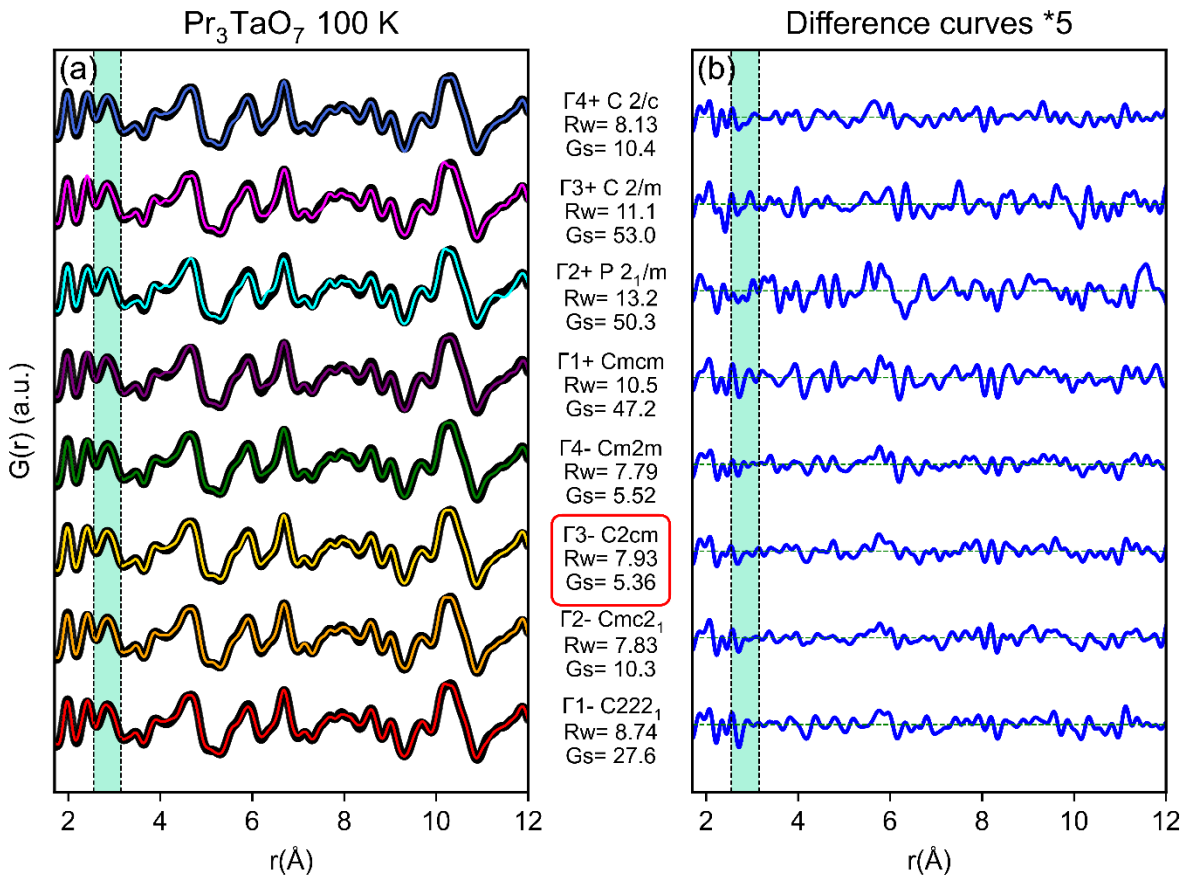

Figure 5.10: (a) Neutron pair distribution function (PDF) of weberite-type Pr_3TaO_7 measured at 100 K (black circles) and refined with the long-range *Cmcm* space group (purple) and with the models derived at the Brillouin zone center (red, orange, gold, green, cyan, magenta, and royal blue) of *Cmcm*. The four non-centrosymmetric models ($\Gamma_{1\text{-}4}^{-}$) are the bottom curves and the four centrosymmetric models ($\Gamma_{1\text{-}4}^{+}$) are the top curves. (b) Difference curves (multiplied by a factor 5) between as-collected data and respective models in the *r*-range between 1.7 – 12 Å. The turquoise shaded area enclosed by the vertical dashed lines between 2.5 and 3 Å highlights the region most sensitive to the O-O atomic correlations. The red frame around the *C2cm* space group highlights the best structural model to describe the PDF of Pr_3TaO_7.

the short-range structure. Several models do not capture the details of the O-O pair correlations around 2.5 – 3 Å and produce systematically positive residuals in the difference curves. The quantitative *Gs*-factor analysis (**Figure 5.11**) identifies the Γ_1^- model as the best in terms of uncorrelated regions, followed by the Γ_3^+ (*C2/m*) model. However, close inspection of the Γ_3^+ model reveals that the 7-coordinated Ho cations exhibit unusually large harmonic (U_{ij}) atomic displacement parameters, despite the measurement being performed at 100 K (**Figure 5.12**). The effect is particularly pronounced along the [010] direction, a side effect related to positional coordinates constrained along this direction by the space group symmetry. This effect is not observed for the Γ_1^- (*C222₁*) harmonic model. Considering that the *C222₁* model has also a smaller set of refined parameters (43 for Γ_1- *versus* 50 for Γ_3^+), we conclude that the short-range organization of Ho_3TaO_7 is best described by the non-centrosymmetric *C222₁* space group.

When comparing the neutron PDF data measured at room temperature refined with the initial long-range symmetry (**Figure 5.9**) with the improved (low temperature derived) short-range models (**Figure 5.13**), it is apparent that the average, long-range structure is not the best model for the actual atomic arrangement.

This leads to the conclusion that there exists a cross-over between the long-range and short-range symmetry in ordered orthorhombic weberite-type tantalates. Family 1 (Pr_3TaO_7) with *Cmcm* long-range symmetry has a short-range structure that is better described by a *C2cm* local atomic configuration, while family 2 (Tb_3TaO_7 and Ho_3TaO_7) with a *Ccmm* long-range symmetry by a *C222₁* local atomic configuration. In both cases, a non-centrosymmetric space group is the most suitable model able to fully capture the subtle, local atomic relaxations and distortions, which are particularly evident for the O-O nearest neighbor

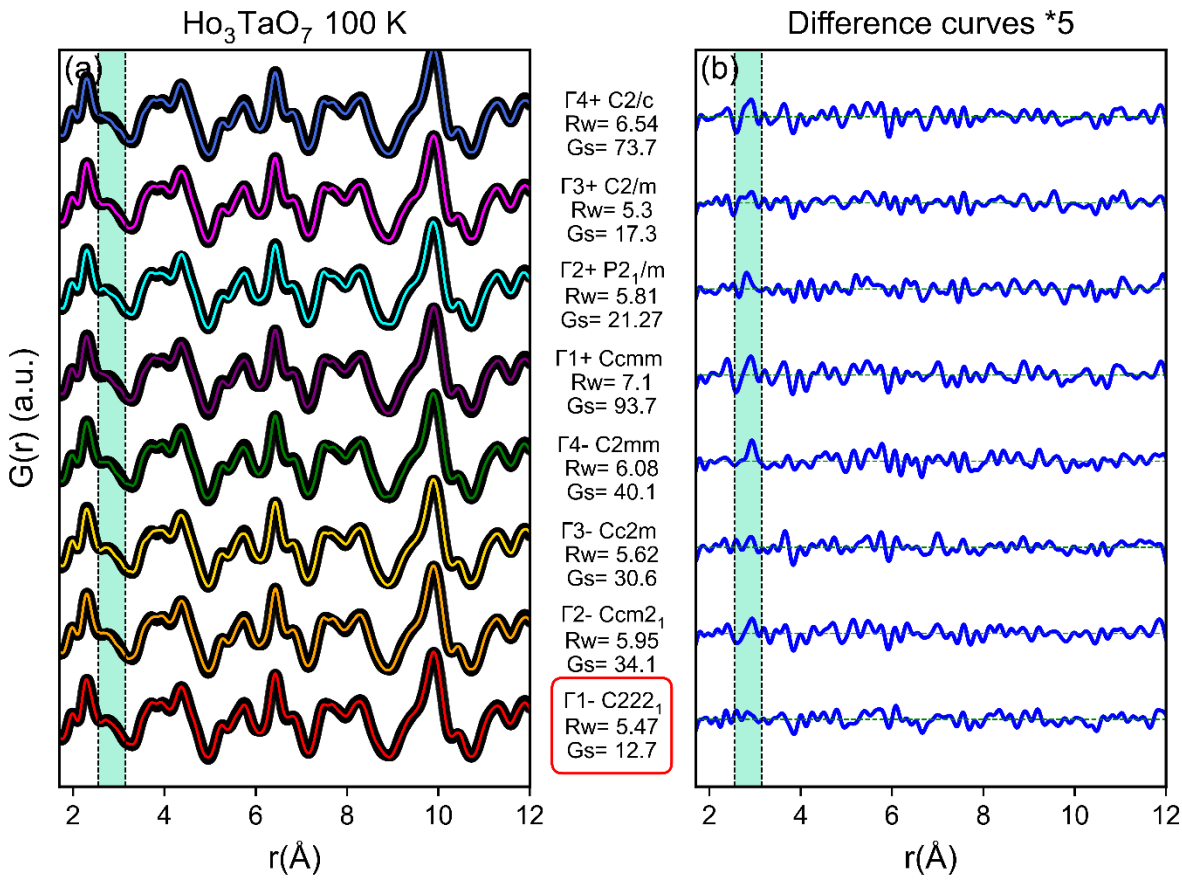

Figure 5.11: (a) Neutron pair distribution functions of weberite-type Ho_3TaO_7 measured at 100 K and modelled with 7 displacive small-box models in addition to the *Ccmm* long-range space group. Black circles represent the experimental data. Red, orange, gold, green, purple, cyan, magenta and royal blue lines are fits of the respective models. (b) Difference curves (multiplied by a factor 5) between as-collected data and respective models in the *r*-range between 1.7 – 12 Å. The turquoise shaded area enclosed by the vertical dashed lines between 2.5 and 3 Å highlights the region most sensitive to the O-O atomic correlations. The red frame around the $C222_1$ space group highlights the best structural model to describe the PDF of Ho_3TaO_7.

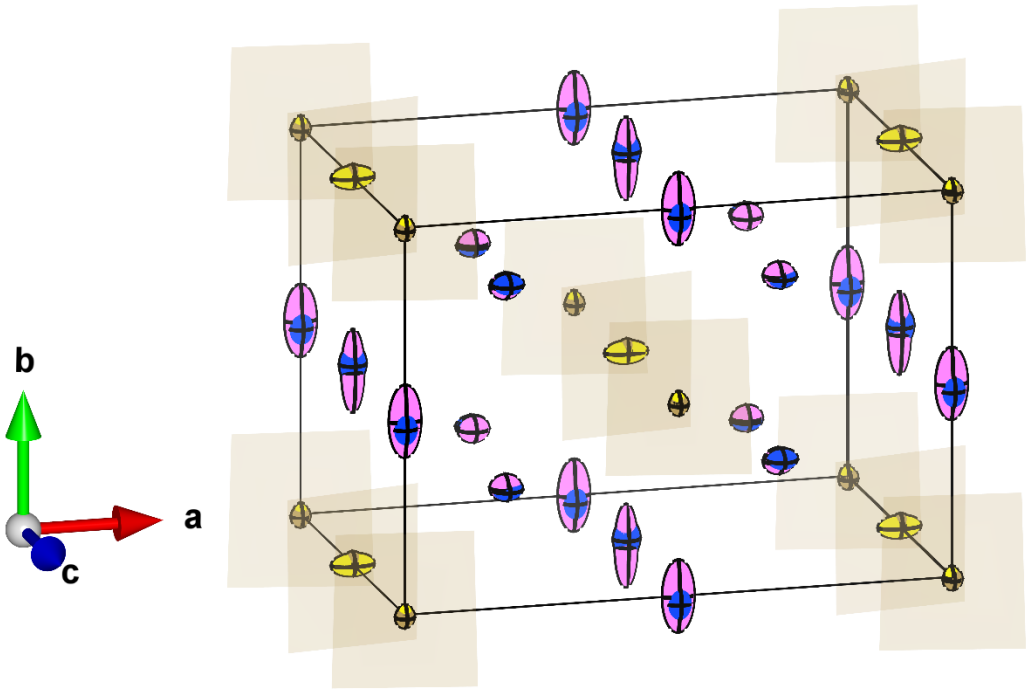

Figure 5.12: Overlayed *C222₁* **(**Γ_1-) and *C2/m* (Γ_{3+}) Ho_3TaO_7 structural models from short-range PDF refinement performed at 100 K. Solid black lines indicate the respective unit cell while shaded brown regions represent TaO_6 octahedra. Ta and Ho cations in respective atomic sites in the *C222₁* structure are indicated as solid dark brown and blue ellipsoids, while Ta and Ho cations in respective atomic sites in the *C2/m* structure are indicated as solid yellow and pink ellipsoids. The ellipsoids represent the extent of anisotropic thermal vibrations, U_{11}, U_{22} and U_{33} diagonal ellipsoid components are not shown.

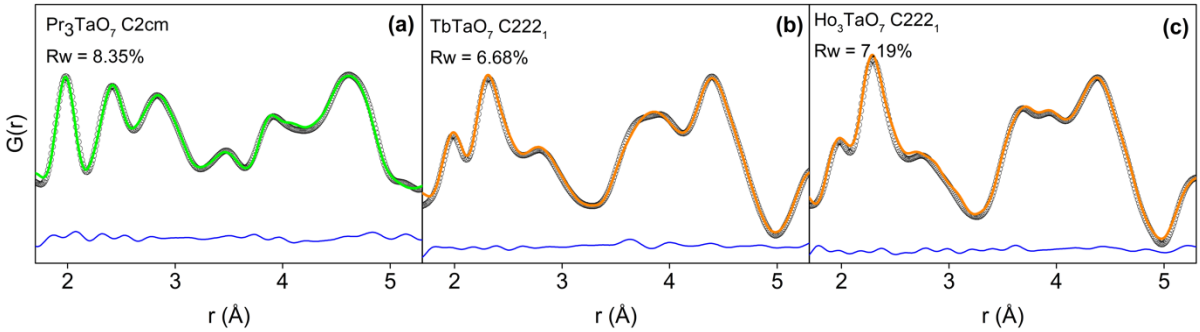

Figure 5.13: A segment of very local (1.7-5.3 Å) neutron pair distribution functions showing 1st and 2nd nearest neighbor correlations of weberite-type A_3TaO_7 (A=Pr, Tb, Ho) modelled with (**a**) *C2cm* and (**b, c**) *C222₁* space groups, respectively. Black circles represent the experimental data while green and orange curves are fits with the respective models. Difference curves between data and models are displayed in blue.

correlations in the PDFs of the two compounds of family 2. In general, the much-improved fit quality of the *C222₁* model for structural family 2 reflects the increased degrees of freedom for the Ta cations in TaO_6 octahedra, which is only allowed in non-centrosymmetric space groups (Ta cations are located at the inversion center of the long-range space group structure). Indeed, there are significant displacements of Ta cations observed in the *C2cm* and *C222₁* models, shifting Ta away from the barycenter of the O anions. In this process, the ADPs of the displaced Ta cations are also satisfactorily reduced in both non-centrosymmetric models according to the expected stiff and tight octahedral environment. The ADPs of the remaining atomic constituents of the structure (Ln cations and O anions) remain unchanged or are slightly reduced.

Small-box analysis of weberite-type compositions with smaller lanthanides (disordered, defect-fluorite structural family)

Discrepancies between the long- and short-range structures (**Figure 5.8**) are most pronounced in the disordered weberite-type compounds of family 3 with defect-fluorite symmetry (Ln = Ho, Tm and Yb) expressed by unacceptable reliability factors (*Rw* values between 22 and 28%). These findings are consistent with previous observations by King *et al.* [20]. The fit quality of the *Fm-3m* model to the PDFs depends on the considered *r*-range, and box-car refinements have been used to determine the extension in real space for which the long-range structure provides an unsatisfactory fit for disordered Ho_3TaO_7, Tm_3TaO_7, and Yb_3TaO_7 (**Figure 5.14**). Particularly, the low-*r* regions of the PDFs characteristic for the nearest neighbor coordination polyhedra (up to 3 Å) are very poorly described by the *Fm-3m* structural model with *Rw* values up to 30%. The fit quality progressively improves for larger *r* regions but remains poor well beyond the size of the

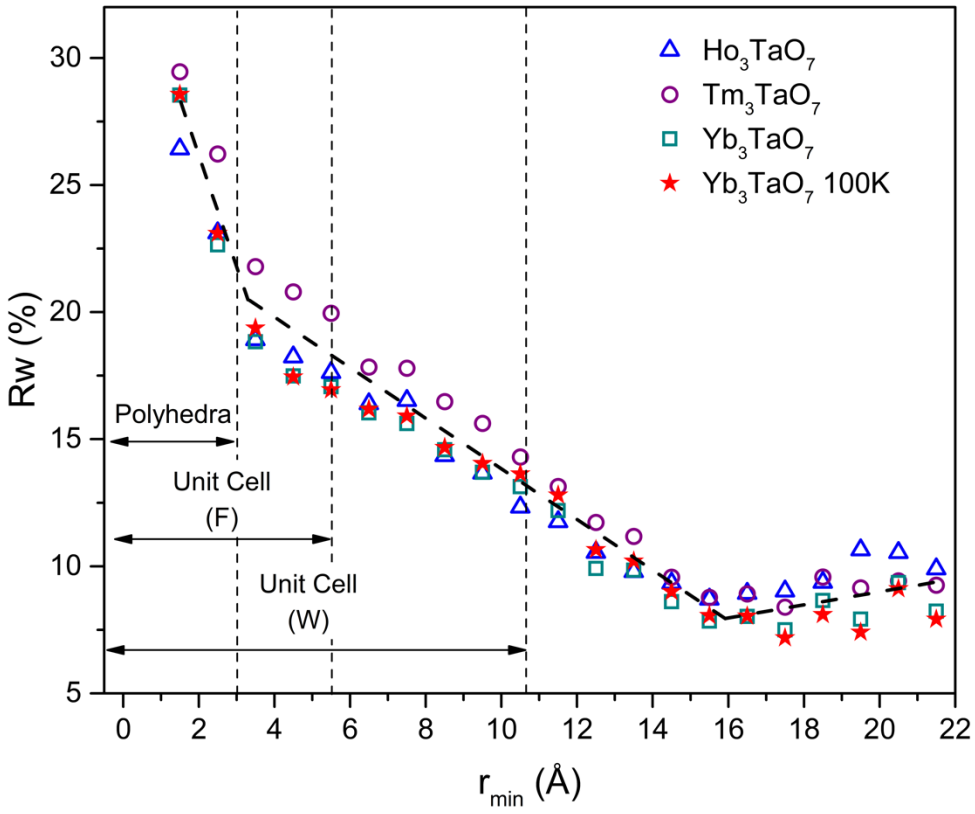

Figure 5.14: Reliability factors, *Rw*, determined from "boxcar" refinements of neutron PDFs of disordered A_3TaO_7 (A = Ho, Tm, and Yb) measured at room temperature and Yb_3TaO_7 measured at 100 K using the long-range *Fm-3m* structural model. The *x*-axis represents the minimum *r*-value (r_{min}) for each 10.5 Å refinement window and the data points correspond to the *Rw* obtained in each refinement window. The bold black dashed line is to guide the eyes with respect to the *Rw* behavior and the vertical dashed lines represent the characteristic distances corresponding to the polyhedra, the lattice parameter a_F of the defect-fluorite unit cell (F), and the a_W lattice parameter of the weberite-type unit cell (W). The different symbols represent individual compounds of the disordered weberite-type family 3 as labelled in the legend.

defect-fluorite unit cell. This behavior clearly indicates that these compounds have a distinct local atomic arrangement not represented by the disordered long-range structure.

Boxcar refinement was performed by monitoring the resulting *R*w values from PDF small-box modeling as a function of a constant *r*-range window (10.5 Å) with increasing minimum fit boundary, r_{min}. The behavior is consistent for all compounds with an initially very high *Rw* value (r_{min} =1.5 – 3 Å) that gradually decreases until reaching a minimum of approximately 10% for a r_{min} of about ~15 Å (**Figure 5.14**). This means that the defect-fluorite model provides only a good description of the structure for interatomic distances and pair correlations exceeding 3-4 times the dimension of the cubic defect-fluorite unit cell (approximately 2 times of the conventional orthorhombic weberite-type unit cell). This trend holds even if the PDF was obtained at low temperature as for Yb_3TaO_7 measured at 100 K. Therefore, an improved structural model must be found to describe the short-range structural details below a *r*-range of about ~15 Å.

For all disordered compounds, Yb_3TaO_7 has the most favorable scattering conditions due to its large neutron scattering length of Yb (12.4 fm); thus, the PDF of this sample was used for the most selective analysis of the short-range structure. Based on the boxcar refinements (**Figure 5.14**), the small-box modeling was limited to a region of *r*-space where the *Fm-3m* long-range model did not provide a good fit quality (1.5 to 12 Å). As alternative structural models for the disordered compounds of family 3, the eight displacive orthorhombic models with tilt system [010], derived from the zone-center representations of the *Ccmm* long-range symmetry (of the neighboring structural family 2), were initially tested. The short-range analysis with these alternative models followed the same approach as described for the ordered weberite-type Ho_3TaO_7 (**Figure 5.11**). To obtain the best structural model for these disordered atomic configurations, the following approach was adopted: (*i*) the sample was measured at 100 K, where

the effect of thermal vibrations is greatly reduced, and (*ii*) the number of allowed thermal parameters was decreased by using only isotropic thermal factors (U_{iso}) to increase the selectivity of the model on the atomic positions. The U_{iso} parameters in each model were set to be distinct for all cation sites and the oxygen sites forming TaO_6 polyhedra and identical for all remaining oxygen sites. This resulted in a smooth convergence of the refinements as shown in **Figure 5.15a**.

All alternative lower symmetry models significantly improved the fit quality (*Rw* values of 10 – 18.6%). Among these models is the one proposed by King *et al.,* who used $C222_1$ to model the short-range structure of Yb_3TaO_7 [20]. However, the best small-box refinements in this study were obtained with the Γ_2- ($Ccm2_1$) and Γ_4- (*C2mm*) models (*Rw* values of 12.2 and 8.65%, respectively), while refinement with Γ_1- produced a significantly higher *Rw* value of 16%. As mentioned before, the most accurate model must describe particularly the PDF region (1.5-3.5 Å) representative of the nearest neighbor distances and coordination polyhedra. Careful inspection of the difference curve in the low-*r* region (**Figure 5.15b)** reveals that all centrosymmetric models, with the exception of Γ_2+ ($P2_1/m$), produce a systematic misfit in the region between 1.5 and 2.5 Å for the Ta-O (first positive residual in PDF) and Yb-O nearest neighbor correlations (second positive residual in PDF). In addition, the O-O nearest neighbor correlations show distinct residuals for these models (shaded region in **Figure 5.15b**). Overall, the four non-centrosymmetric models agree much better to the data with respect to the Ta-O and Yb-O correlations, but they differ in the description of the O-O correlations. Quantitative analysis of *Gs* confirms that the Γ_4- (*C2mm*) model also has by far the lowest correlated residual among all models. Therefore, we conclude that this is the most accurate model in describing the short-range structure of Yb_3TaO_7.

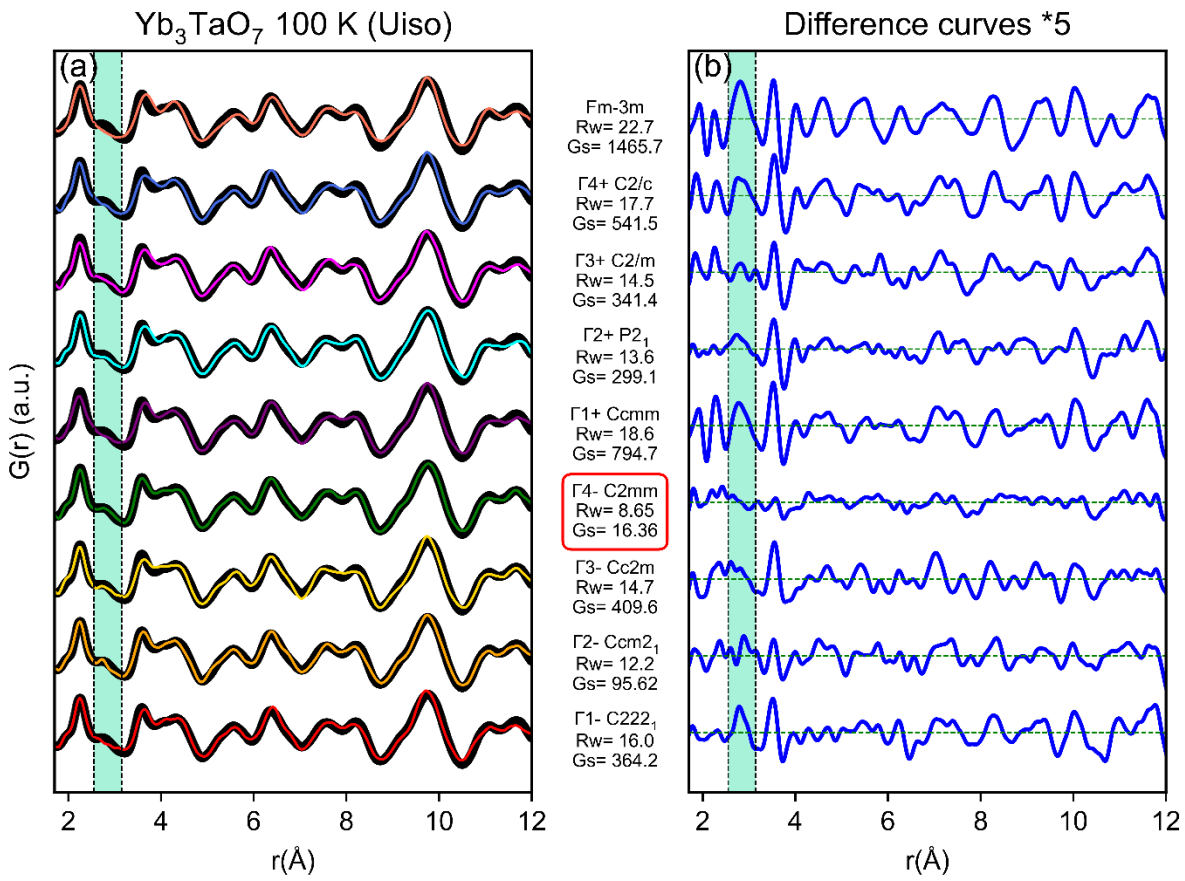

Figure 5.15: (a) Neutron pair distribution functions of Yb_3TaO_7 measured at 100 K (black circles) and refined with the *Fm-3m* defect-fluorite model (top). The eight alternative models are shown as red, orange, gold, green, purple, cyan, magenta, and royal blue curves. (b) Difference curves (multiplied by a factor 5) between data and models in the *r*-range between 1.7 – 8 Å. The turquoise shaded area enclosed by the vertical dashed lines between 2.5 and 3 Å highlights the region most sensitive to the O-O atomic correlations. The red box around the *C2mm* space group highlights the best structural model to describe the PDF of Yb_3TaO_7.

The use of this non-centrosymmetric space group indicates an inversion center loss at the atomic scale. This space group provides more degrees of freedom and differentiates Ta-O bond lengths, allowing more pronounced distortions of TaO_6 octahedra. Nonetheless, despite this displacive disorder, a high level of occupational order is locally maintained, which contrasts the fully disordered character of the long-range defect-fluorite structure. However, there are still some regions in the PDF that are not fully captured by the *C2mm* model (*e.g.*, feature at 3.9 Å). This suggests that mesoscale polyhedra stacking and ferroelastic boundaries among nanoscale *C2mm* domains can produce detectable correlations in the PDF, which cannot be described with a simple small-box model.

To test the broader transferability of the newly established model, the PDFs of all three defect-fluorite structured samples (Ho_3TaO_7, Tm_3TaO_7, and Yb_3TaO_7) measured at the room temperature were refined with the same *C2mm* space group over the same *r* region (1.5-12.0 Å). Small box modeling using this model (**Figure 5.16**) provided excellent agreement to the experimental data with a significant drop in *Rw* values compared to the initial fits with the long-range *Fm-3m* structural model (**Figure 5.8**). The lower *Rw* value for Yb_3TaO_7 at room temperature compared to low temperature can be explained by the effect of thermal broadening. The overall good agreement, for all disordered samples studied here, leads to the conclusion that the compounds of weberite-type family 3 with a long-range *Fm-3m* structure, are best described by the orthorhombic *C2mm* space group.

The simultaneous characterization of the short-range and long-range structure by total scattering experiments revealed that all studied weberite-type tantalates exhibit some degree of structural heterogeneity across different length scales. In all cases, the space groups, which modeled the diffraction data the best, did not accurately describe the PDFs. Alternative structural

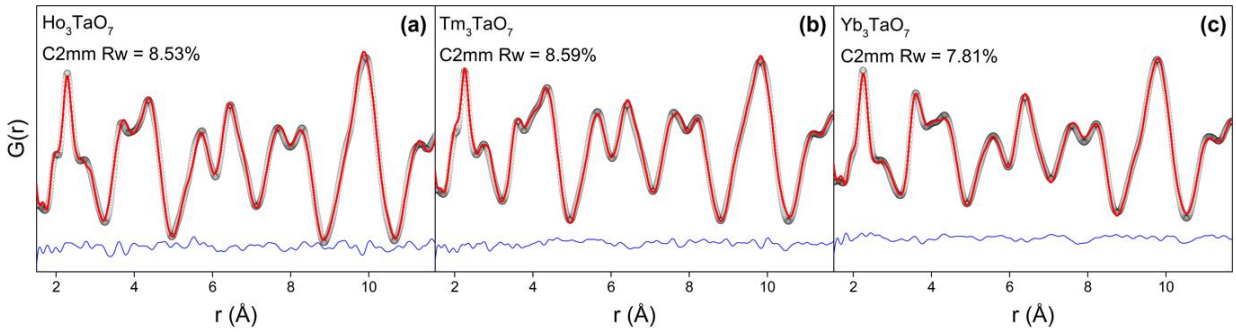

Figure 5.16: Neutron pair distribution functions (black circles) of disordered Ho_3TaO_7, Tm_3TaO_7, and Yb_3TaO_7 measured at room temperature and modeled (red curves) using the *C2mm* space group derived from PDF refinement of Yb_3TaO_7 measured at 100 K. The blue curves represent the difference between experimental data and refinement.

models were required to capture the local atomic configurations, an exploration that yielded improved small-box refinements. To summarize this behavior and derive general trends among the three structural families, the *Rw* values of initial and improved PDF models were compared (**Figure 5.17**).

The improved model used for disordered family 3 compounds showed a large *Rw* drop, suggesting that the atomic arrangements in disordered compounds are most distinct from the long-range average structures. The local structure is in fact quite similar to the short-range organization of intermediate lanthanides of family 2 (Tb, Ho) that display an ordered long-range orthorhombic structure. The refinement of the PDFs of family 2 samples with the improved local model showed a more limited decrease of *Rw*. This indicates that the short-range structure of these compounds has only minor deviations from the long-range centrosymmetric model. For the larger lanthanides, Pr_3TaO_7, of the ordered orthorhombic family 1, the reduction in *Rw* values is somewhat larger again as compared with family 2 compounds, suggesting more pronounced deviations of the local atomic arrangement from the long-range centrosymmetric structure. While this *Rw*-value analysis (**Figure 5.17**) is partially biased by the different neutron scattering lengths of the individual lanthanide elements (ranging from 4.6 fm for Pr to 12.4 fm for Yb), it still highlights the structural complexity across all weberite-type tantalates, showing a strong dependence on chemical composition and characteristics of the long-range structure.

5.4 Discussion

Considering the structures of weberite-type tantalates as a derivative of the high-symmetry prototype *Cmmm* structure, provides a unified framework for explaining the findings of this study.

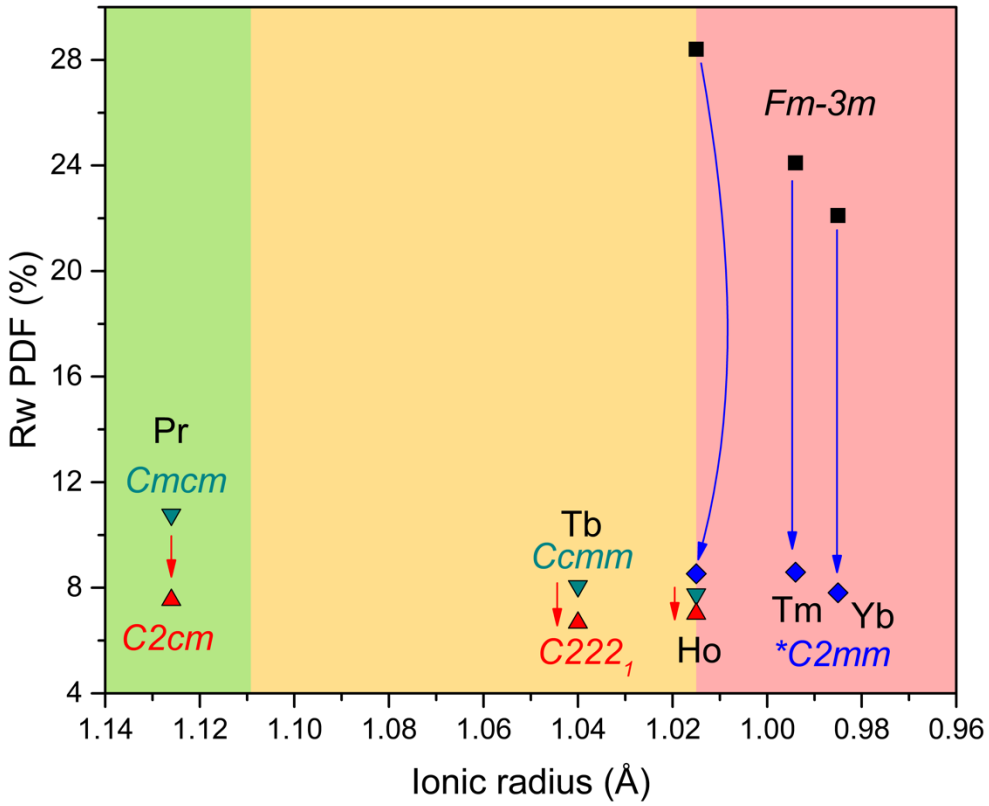

Figure 5.17: Reliability factors (*Rw*) of neutron PDF refinements of Ln_3TaO_7 compounds displayed as a function of the ionic radius of the Ln cation. *Rw* values based on *Cmcm* and *Ccmm* structural models are shown as downward oriented dark green triangles, and as black squares for *Fm-3m* structural model. *Rw* values based on alternative *C2cm*, *C222₁* models are shown as upward oriented red triangles and as blue chevrons for *C2mm* model respectively. Red and blue arrows denote decrease in *Rw* factors for improved models. Green, yellow and red shaded regions represent the long-range structural families: green = family 1 (*Cmcm*), yellow = family 2 (*Ccmm*), and red = family 3 (*Fm-3m*).

The three structural families can be described by two distinct tilt systems, [100] and [010], corresponding to distinct irreducible representations of this prototype structure at the *Z*-point of the Brillouin zone. The two tilt systems were unambiguously determined through analysis of peak extinctions in high-resolution diffraction data. Structural family 1 compounds with large lanthanides (Pr_3TaO_7) exhibit a *Cmcm* long-range structure with the [100] tilt system, while structural family 2 compounds with intermediate lanthanides (Tb_3TaO_7 and ordered Ho_3TaO_7) display the *Ccmm* space group with the [010] tilt system. Only one weberite-type tantalate compound can display both tilt systems: Nd_3TaO_7, at the boundary between families 1 and 2 undergoes a first order semi-reconstructive transition from a low temperature [010] tilt system to a high temperature [100] tilt system as reported in [5]. Finally, family 3 compounds with small lanthanides (disordered Ho_3TaO_7, Tm_3TaO_7, and Yb_3TaO_7) with a defect-fluorite structure *Fm-3m* exhibit the same tilt system as structural family 2, but with a very short correlation length. The average tilt angle of TaO_6 octahedra is directly related to the *c*-axis of weberite-type structures. The amplitude of this tilt was extracted using the lattice parameters determined in the present study (neutron total scattering and X-ray diffraction results) and those reported by Wakeshima *et al*. [5]. In the case of the defect-fluorite structure, the *c*-axis was reconstructed by using the metric transformation between the two lattices ($a_F\sqrt{2}$). The average tilt angle increases linearly as a function of decreasing ionic radii of the lanthanide ions across all three structural families (**Figure 5.18, white squares**). While the transition from structural family 2 to family 3 (Ho_3TaO_7) displays a continuous evolution at the macroscopic scale, there is an apparent discontinuity between families 1 and 2 (Nd_3TaO_7). This is a result of the change in the Ta-O-Ta inter-polyhedra tilt system occurring between the low- and high-temperature polymorphs of Nd_3TaO_7. None of these long-range structural models provide an accurate description of the local structure. Improved models

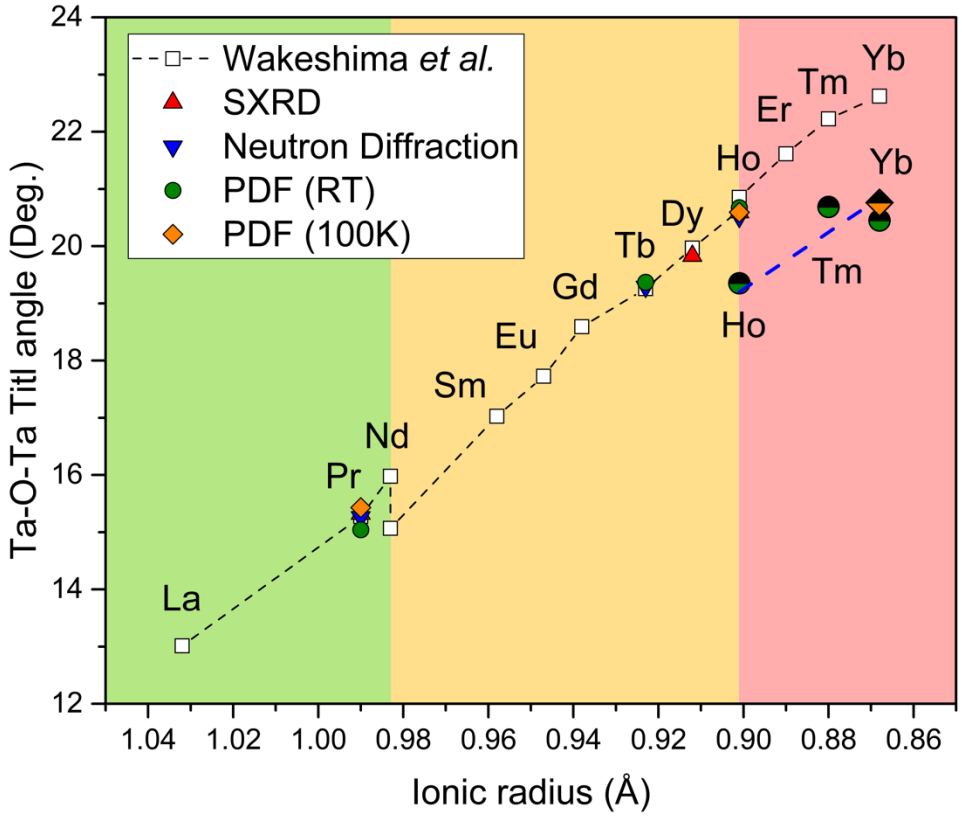

Figure 5.18: Ta-O-Ta tilt angles between TaO_6 octahedra in Ln_3TaO_7 derived from c-lattice parameters published by Wakeshima *et al.* [5] as a function of ionic radius of the lanthanide cations shown as white squares and connected by a black dashed line. The c-lattice parameter for (long-range) defect-fluorite structured compounds (Ln = Ho-Yb) was estimated as $a_F\sqrt{2}$. Tilt angles determined from c-lattice parameters measured in this study by SXRD and neutron diffraction data (long-range) are shown as red and blue triangles. Tilt angles determined from short-range structures are shown as green spheres for room temperature data and as orange chevrons for 100K data. Fully filled circles and chevrons denote PDF models obtained from ordered compounds (Pr, Tb, Ho) whereas partially filled colored symbols denote models obtained for disordered compounds (Ho, Tm, Yb) with blue dashed line serves as a guide to the eye. Green, yellow and red shaded regions represent the long-range structural families: green = family 1 (*Cmcm*), yellow = family 2 (*Ccmm*), and red = family 3 (*Fm-3m*).

were derived for all three families and allowed the description of local tilts and deformations of coordination polyhedra across the entire lanthanide series.

The evolution of the tilt angle of TaO_6 octahedra derived from the PDF refinements shows excellent agreement with the results from the long-range analysis for families 1 and 2 at room temperature and low temperature (**Figure 5.18,** colored symbols). The structure analysis of the PDF data of family 3 allows direct determination of the tilt angle beyond the estimation based on the lattice parameter of the defect-fluorite structure. The evolution of the tilt angle with decreasing ionic radii remains linear for the three compositions of family 3 with no explicit dependence on the sample temperature (**Figure 5.18,** partially filled symbols); however, there is a distinct discontinuity between families 2 and 3, occurring for the ordered and disordered polymorphs of Ho_3TaO_7. Despite the observed discontinuities, a single slope seems to describe all data. The systematic increase in tilt angle across the entire series can be explained by the contraction of the lanthanide ionic radii. The linear dependence suggests that rigid TaO_6 octahedra are a good approximation because the tilt angle produces a linear reduction of the available volume for the lanthanide polyhedra. This also explains the two observed discontinuities; the tilt angle is larger for the high-temperature polymorph of Nd_3TaO_7, but is reduced for low-temperature phase, thus maintaining an optimum volume available for the Nd cation. For Ho_3TaO_7, the ordered polymorph has a larger tilt, reducing the volume required for the Ho cation, a configuration that cannot be achieved in the disordered polymorph where the Ho experiences significant positional disorder.

For the discussion of the octahedral tilt, TaO_6 octahedra were approximated as rigid units; however, small internal distortions may occur that can be assessed through analysis of the short-range structure. (**Figure 5.19**). Two parameters are important to describe such distortions: the

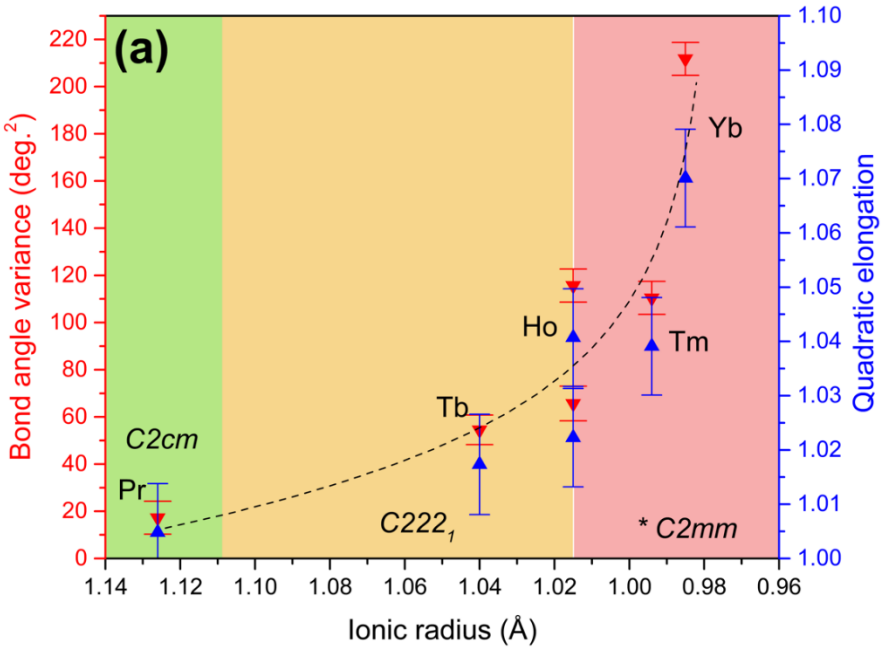

Figure 5.19: Various polyhedra parameters of Ln_3TaO_7 (Ln = Pr, Tb, Ho, Tm, and Yb) extracted from PDF refinements using *C2cm* (Pr), *C222$_1$* (Tb, Ho), and *C2mm* (disordered Ho, Tm, Yb) models. (a) Bond angle variance (downward oriented red triangles) and quadratic elongation (upward oriented blue triangles) parameters of TaO_6 octahedra with the dashed black curve serving as a guide to the eyes. (b) Magnitude of the displacement vectors (distance between the Ta position and the O_6 barycenter) and respective vector directions. (c) Respective volumes of TaO_6, BO_7, and BO_8 polyhedra from short-range structures (*C2cm*, *C222$_1$*, *C2mm*) shown as completely filled symbols for Ln = Pr, Tb, and ordered Ho and as semi-filled symbols for Ln = disordered Ho, Tm, and Yb. Additionally shown as white-filled symbols are the average polyhedra volumes from the long-range structures (*Cmcm*, *Ccmm* and *Fm-3m*). Circles, upward-oriented triangles and squares indicate TaO_6, LnO_7 and LnO_8 polyhedra, respectively, whereas white-filled red stars indicate average $(Ta/Ln)O_7$ polyhedra from long-range *Fm-3m* models. For the ease of visualization, the legend is also shown within the white box above the data, denoting polyhedra from long-range diffraction and short-range PDF models as '*Diffr*' and '*PDF*', respectively. Green, yellow, and red shaded regions represent the three weberite-type tantalate long-range families with green (family 1, *Cmcm*), yellow (family 2, *Ccmm*), and red (family 3, *Fm-3m*). The error bars in (a) represent propagated uncertainties from quadratic elongation and bond angle variance formulas, while in (b), uncertainties are calculated by the VESTA crystallographic software.

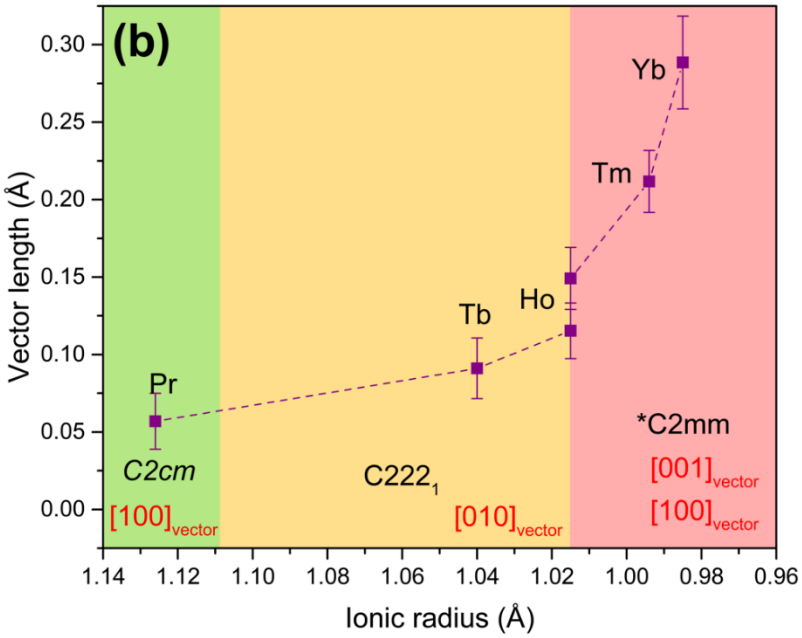

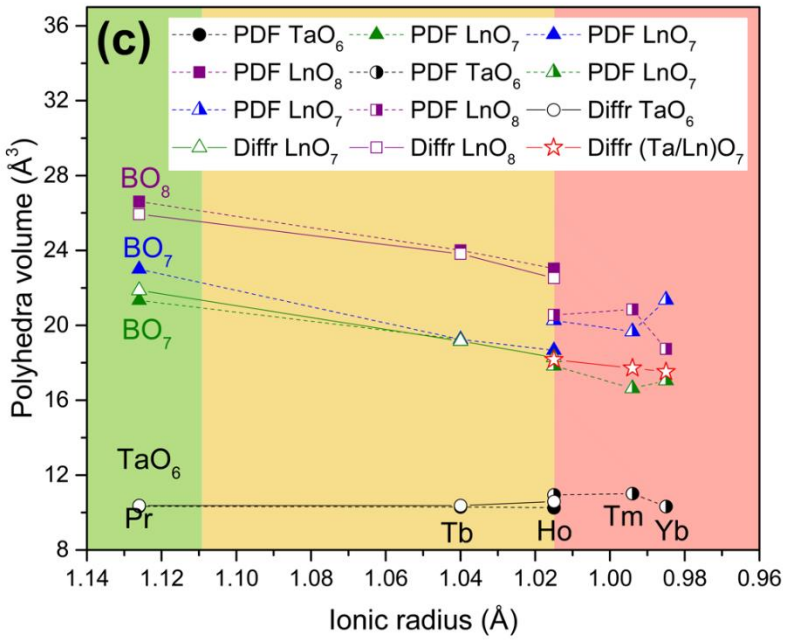

Figure 5.19 (continued).

bond-angle variance and the quadratic elongation [81], which were both determined by atomic positions from the PDFs for all compounds (**Figure 5.19a**). The TaO_6 octahedra in family 1 compounds (Pr_3TaO_7) have six almost identical Ta-O bonds, and therefore, an extremely small value of quadratic elongation [5], but slightly different O-Ta-O angles (whose distributions are described by the bond angle variance), a feature characteristic of a pure trigonal distortion. For family 2 (Tb_3TaO_7 and ordered Ho_3TaO_7), the Ta-O bonds display larger trigonal distortions, and a tetragonal distortion also develops with the Ta-O bond lengths splitting into three pairs of distances for these compounds. At the boundary between family 2 and family 3 there appears another discontinuity, which is apparent in both distortion parameters of the ordered and disordered polymorphs of Ho_3TaO_7. For family 3 compounds (disordered Ho_3TaO_7, Tm_3TaO_7, and Yb_3TaO_7) both parameters further increase with decreasing ionic radii of the lanthanide cations, mirroring the behavior already observed for the octahedral tilts (**Figure 5.18**).

While the underlying mechanisms of these distortions are not fully understood, this seems to be a secondary effect of the octahedral tilts; for family 3, the larger amplitudes can be related to the loss of long-range order. The distortion of the TaO_6 octahedra might be explained by a pseudo-Jahn-Teller type mechanism as observed in perovskite compounds [82], because the Ta^{5+} cations in an octahedron have d^0 electronic configuration, known to promote off-center displacements. From this analysis, such octahedral distortions are significant in weberite-type tantalates and suggest an increasing covalent bonding character of the corner-shared TaO_6 framework in compounds with smaller lanthanide cations. Weberite-type compounds have often been studied for their magnetic properties [5]; however, the short-range analysis reveals the ferroelectric character of the TaO_6 octahedra due to the non-centrosymmetric nature of the local atomic

arrangement. It would be therefore more appropriate to classify these compounds as multiferroic systems.

The off-center displacements of the Ta^{5+} cations within the coordination polyhedron can be precisely captured by the dipolar vector defining the position of the geometric center of mass of the O_6 group of anions relative to the actual Ta position (**Figure 5.19b**). Following the same trend of the distortion parameters (**Figure 5.19a**), the dipolar vector increases slightly from Pr_3TaO_7 to ordered Ho_3TaO_7, then followed by a sharp increase for disordered Ho_3TaO_7, a trend which extends to the other disordered compounds of family 3.

All changes to the rigid TaO_6 framework (tilts and distortions) are likely to impact the other polyhedra. Since LnO_7 and LnO8 are irregular, it is hard to develop equivalent distortion parameters to describe their changes; therefore, we analyzed the changes in polyhedra volumes measured across all structural families as a function of ionic radii (**Figure 5.19c**) for both local short-range (colored symbols) and long-range (white symbols) structures. As expected, the TaO_6 octahedra experience no significant change across the series, being the most rigid element of the structure. On the other hand, LnO_8 and LnO_7 polyhedra show a monotonic decrease of their volumes as a function of Ln ionic radii, with LnO_8 decreasing more rapidly than LnO_7, a trend accelerating in disordered compounds. No significant discrepancy between short-range and long-range polyhedra volume is observed in ordered compounds, whereas at the frontier between family 2 and 3, disordered compounds display an abrupt change in volume leading to smaller polyhedra than what can be estimated from long-range trends. Moreover, in *C2mm* local structure (Γ_4-) there are two independent LnO_7 polyhedra: the volume of one of them converges to the volume of LnO_8, whereas the other one is consistently smaller.

Three different space groups were used to model the local structure of all weberite-type tantalates using small-box refinement of the PDFs. This is required to obtain an accurate description of the atomic arrangement of each compound. Nevertheless, the changes across the short-range structure are more gradual and are captured by the cooperative tilts and distortions of the coordination polyhedra (**Figures 5.18 and 5.19**). The spatial extent of these modifications over macroscopic length scales is highly dependent on the ionic radii of the lanthanide cations and determines the apparent symmetry of the long-range structure. The two observed tilt systems, which were described as instabilities of the *Cmmm* prototype structure, explain the two observed long-range symmetries of family 1 and 2. For a given tilt angle, tilt system [010] of family 2 is more effective in achieving the necessary polyhedra volume reduction to accommodate the lanthanide cations in the structure. With further increase in tilt, dipolar contributions of the Ta cations also increase, competing energetically with the tilts. Above a given threshold in lanthanide ionic radii, the dipolar energy begins to dominate and prevents a long-range tilt organization, leading to a long-range disordered structure. This marks the transition between families 2 and 3. For Ho_3TaO_7, this cooperative ordering of the dipoles depends on the annealing conditions, which explains the existence of the ordered and disordered polymorphs.

The rank ratio of the space groups of the local structure and long-range structure provides the number of domain variants required to achieve the apparent long-range symmetry [83], [84]. The long-range structure is the configurational average of these correlated local domain variants [14]. For example, in structural family 1, the long-range space group is *Cmcm*, while *C2cm* was used to describe the short-range structure; therefore, only two variants exist as a result of the loss of the mirror plane. In family 2 (long-range *Ccmm*, short-range $C222_1$), two variants also exist, but they are related to each other by the loss of the inversion center. In both cases, configurational

averaging of the two variants yields the ordered long-range structure. For family 3 (long-range *Fm-3m*, short-range *C2mm*), 96 variants are involved in the configurational average that forms the disordered defect-fluorite long-range structure since the space groups belong to different crystal systems (orthorhombic and cubic). It is interesting to note, that only Y_3TaO_7 is fully described by the $C222_1$ space group at any length-scale and therefore no configurational averaging is required [36], [46].

All of these structural descriptions and underlying effects can be summarized in the following manner: the monotonic decrease Ln ionic radius dictates the formation of three long-range structural families. Family 1 displays a [100] tilt of Ta-O-Ta chains, while structural family 2 displays a [010] tilt and both ordered structures retain the same motif of TaO_6, LnO_7, and LnO_8 polyhedra. In the structural family 3 with defect-fluorite structure, these polyhedra are not distinguishable and the tilt definition is lost. Across the structural family 1, the Ln ionic radius decreases, which causes a monotonic contraction of the unit cell, accompanied by the increase of the [100] tilt, linked with the c-lattice dimension. The [100] tilt becomes incompatible with the ionic radius of Nd cation, and Nd_3TaO_7 displays a semi-reconstructive first order phase transition, from [100] to [010] tilt systems, which results in a discontinuity in tilt angles for Nd_3TaO_7. As Ln ionic radius continues to decrease, the respective unit cell volumes continue to contract monotonically and Ln cations smaller than Nd adopt the [010] tilt system instead, to counteract this behavior. The decrease of orthorhombic unit cell volumes, and especially the 'rigid' c-lattice parameter, causes a monotonic increase of the [010] tilt, reaching maximum for the Ho_3TaO_7 compound. A polymorph of Ho_3TaO_7 and Ln cations smaller than Ho display a disordered structure with almost no structural information. The alternative short-range structures are identified for all three families to counter this issue and to characterize the following structural

features: (i) an inter-polyhedra loss of inversion center, governed by increasing polarizability of Ta cation, (ii) corresponding distortions of polyhedra across the compositional series, (iii) Ta-O-Ta tilt angle, an intra-polyhedral character and (iv) the respective sizes of 'rigid' TaO_6, 'soft' LnO_8 and LnO_7 polyhedra. Within these short-range structures, several trends can be observed. The decreasing ionic radius of Ln cation results in (i) an increasing polarization of Ta, thus an increasing offset of Ta cation from TaO_6 barycenter, which in turn dictates the necessity of non-centrosymmetric space groups to describe the local organization, (ii) an increasing amount of local trigonal (Pr) and then both trigonal and tetragonal (Tb-Yb) distortions across the series, (iii) increasing Ta-O-Ta tilt angle, necessary to compensate the decrease of c-lattice parameter and (iv) a monotonic decrease of polyhedra size across the series. As all of these effects are accumulated, the structure becomes unable to compensate for accumulated distortions and collapses to a long-range defect-fluorite configuration for smaller Ln. Locally, this effects progresses even across structural family 3, as Ta-O-Ta, polyhedra distortions and increased polarization of Ta cation mark a consistent trend across the local organization.

It remains to be shown whether the findings of this study on weberite-type tantalates have implications to other weberite-type compounds, such as niobates (Ln_3NbO_7) and antimonates (Ln_3SbO_7). The electron affinity increases in the sequence Ta^{5+} - Nb^{5+} - V^{5+} and Jorgensen *et al.* [85] has discussed the nephelauxetic effect in several octahedral compounds establishing that covalency, described by the formation of molecular orbitals from the metal ion orbitals and the orbitals of the surrounding oxygen anions, increases in the sequence 5*d*-4*d*-3*d*. The Nb^{5+} and Ta^{5+} cations have no *d* electrons, whereas the Sb^{5+} cation has a completely filled *d* shell. The structural differences between mixed metal oxides containing Nb^{5+}, Sb^{5+}, and Ta^{5+} cations can be qualitatively understood by the different metal interactions, which are very effective for Nb^{5+}, not

effective for Sb^{5+}, and only weakly effective for Ta^{5+} [86]. Therefore, it can be expected that displacements are strongly enhanced in Nb^{5+}, weaker in Ta^{5+}, and unfavorable for Sb^{5+}. The expected ferroelectric character should then be distinct in the three series of weberite-type oxides as well as the competitive magnetic interactions.

The complex structural behavior with ordered local atomic configurations within a highly disordered long-range structure found in this study for family 3 appears to be a broader phenomenon. A similar behavior was reported before for disordered, defect-fluorite structured $A_2B_2O_7$ pyrochlore [14], [15], [18] , inverse AB_2O_4 spinel [87], and $A_4B_3O_{12}$ delta phase [88]. These results show that atomic arrangements describing the ground state of a material may differ from that derived from analysis of X-ray diffraction data providing information on the long-range structure. The discrepancy between short- and long-range structures appears to be most pronounced for disordered systems. A more comprehensive multi-scale analysis is therefore required to accurately describe the structure-property relations in complex oxides.

5.5 Conclusion

This study revealed that lanthanide-bearing weberite-type tantalates exhibit three distinct long-range structures over the range of lanthanide ionic radii. Structural models were derived based on high-resolution, low-temperature X-ray and neutron diffraction characterization. Family 1 compounds (Pr_3TaO_7) have a *Cmcm* structure, represented by systematic TaO_6 octahedral tilt along [100]. The structure of family 2 compounds was reassessed; the members of family 2 (Tb_3TaO_7 and Ho_3TaO_7) display a *Ccmm* structure, for which the octahedral tilt is along [010]. Family 3 compounds (disordered Ho_3TaO_7, Tm_3TaO_7, and Yb_3TaO_7) have a disordered, defect-

fluorite *Fm-3m* structure with no long-range tilt system. However, analysis of the short-range structure by means of neutron PDF analysis revealed that each long-range structure is the result of configurational averaging of local atomic domains with distinct displacements and orientations. The derived structural models for the short-range structure, best described for the three families by non-centrosymmetric *C2cm*, $C222_1$, *C2mm* space groups, respectively, are the true ground states that accurately capture all atomic relaxations, tilts, and distortions. All of these effects are the result of an increased local polarization of Ta cation: the local loss of inversion center, which results in a distortion of polyhedra and progresses monotonically across the series. When the critical quantity of local distortions is acquired, the system experiences a frustration, leading to a change in the direction of the octahedral tilt system, which explains the long-range transition between families 1 and 2. Furthermore, the dipolar interactions with increasing tilt angles are responsible for the loss of long-range order and the transition to family 3. Detailed knowledge of this atomic-scale structural behavior is essential to fully describe the multiferroic character of these compounds. The structural heterogeneity across multiple length scales, particularly pronounced in long-range disordered compounds, may have also implications on other physical properties at the equilibrium and out-of-equilibrium (*e.g.*, thermomechanical gradients, mass-transport, and irradiation environments) as domain boundaries and interfaces can lead to the formation of a percolating network capable of accommodating large concentrations of point defects.

Chapter 6: Probing the long- and short-range order of ion-irradiated A_3TaO_7 weberite-type oxides by synchrotron X-ray diffraction and neutron total scattering

This chapter contains text presented in the unpublished manuscript "***Probing the long- and short-range order of ion-irradiated A_3TaO_7 weberite-type oxides by synchrotron X-ray diffraction and neutron total scattering***" by Igor M. Gussev, Eric. C. O'Quinn, Mason King, Jörg Neuefeind, Michelle Everett, David Sprouster, Frieder Koch, Gianguido Baldinozzi and Maik Lang. For this yet unpublished work: M.L. conceived the irradiation experiment, I.G and M.K. provided the samples, I.G., E.C.O., J.N., and M.E. performed the neutron total scattering experiments, D.S. performed the X-ray diffraction experiments. F.K. performed irradiation experiment I.G., E.C.O., M.K., and G.B. analyzed the data, and I.G. wrote the manuscript with input from all the authors.

This work was supported by the U.S. Department of Energy, Office of Science, Basic Energy Sciences, under Award DE-SC0020321. Partial support was provided by the Joint PhD Programme of Université Paris-Saclay as part of the *Investissements d'Avenir* program, grant number ANR-11-IDEX-003. This work was also supported by the U.S. Department of Energy, Office of Science, Basic Energy Sciences, under the SCGSR fellowship program. The SCGSR program is administered by the Oak Ridge Institute for Science and Education for the DOE under contract number DESC0014664. This research used resources at the Spallation Neutron Source, a DOE Office of Science User Facility operated by the Oak Ridge National Laboratory. These experiments and analyses were supported by the U.S. Department of Energy (DOE) Office of Fusion Energy Sciences under Contract No. DE-SC0018322 with the Research Foundation for the State University of New York at Stony Brook. This research used resources at the Pair Distribution Function Beamline of the National Synchrotron Light Source II, a U.S. Department of Energy

(DOE) Office of Science User Facility operated for the DOE Office of Science by Brookhaven National Laboratory under Contract No. DE-SC0012704. The results presented here are based on a UMAT experiment, which was performed at the M-branch and X0 beamline of the UNILAC at the GSI Helmholtzzentrum für Schwerionenforschung, Darmstadt (Germany) in the frame of FAIR Phase-0.

6.1 Abstract

The response of A_3BO_7 weberite-type oxides to swift heavy ion irradiation is examined for the first time. Using 946 MeV Au ions, the structural evolution was examined with increasing radiation exposure, revealing that weberite-types, like other fluorite derivatives, are amorphizable. Also, as with other fluorite derivatives, the development of the amorphous phase correlates with the cation size variance. Deeply penetrating 1.46 GeV Au ions enabled the use of bulk scattering techniques, such as neutron total scattering and PDF analysis. Irradiated weberite-type structures retain the polyhedral building blocks characteristic of their unirradiated form, in contrast to compositionally-related compounds such as pyrochlore, under identical conditions. The concept of cation size variance as a tool for predicting radiation tolerance in complex oxides, which was previously linked with the propensity for compositional disorder, is extended here as it instead correlates with the local displacive disorder in weberite-type oxides. This capacity for displacive disorder, only evident with neutron PDF analysis, is the source of local radiation tolerance in weberite-type oxides and is related to the topology of the BO_6 octahedral network. These results, which elucidate the structural response of weberite-type oxides to ionizing radiation, extend the knowledge about fundamental ion-matter interactions across multiple spatial length scales within the important class of fluorite-derived materials.

6.2 Introduction

Complex ionic materials exhibiting the $A^{3+}{}_3B^{5+}X_7$ stoichiometry often adopt the weberite-type structure, subject of much recent attention due to its compositional flexibility [9], structural peculiarities [1] [2] and a diversity of physical properties [32], [89], [90]. The weberite-type complex oxide structure is a $2\times\sqrt{2}\times\sqrt{2}$ superstructure of the ideal AO_2 fluorite structure, itself consisting of interpenetrating face-centered cubic cation and simple cubic anion sublattices, resulting in cations sitting in perfect eight-fold cubic coordination with the anions. In the weberite-type derived structures, constitutional anion vacancies and O interstitials yield distinct cation polyhedra. The A-site cation occupies two distinct polyhedra: eight- and seven-fold coordinated distorted cubes, and the B-site cation resides in a six-coordinated octahedron. Although all structurally ordered weberite-type oxides can be characterized in this way, the actual symmetry of any chemical compound is defined by the relative sizes of the cations at the A- and B-sites [5], [37], [91]. For example, Ln_3TaO_7 (Ln = lanthanide) exhibits three distinct symmetries: (family I) orthorhombic space group *Cmcm* for large Ln, (family II) orthorhombic *Ccmm* for medium Ln, and (family III) cubic, *Fm-3m* for small Ln. In the latter case, the compounds are isostructural with fluorite but structurally disordered with cations and anion vacancies randomly distributed on their respective sublattices. In other cases (Y_3TaO_7, *C222₁*; Pr_3NbO_7, *Pnma*), other symmetries may be adopted, but for all ordered compounds, the differences between symmetries reflect displacive distortions away from the general structural building block described above.

Although the response of $A^{3+}{}_3B^{5+}O_7$ weberite-type oxides to swift heavy ion irradiation has not been reported, the response of compositionally related $A_2B_2O_7$ pyrochlore oxides has been well-documented due to their consideration as an actinide-bearing nuclear waste form [92]–[95]. The propensity to amorphize under exposure to ions has been shown to correlate directly with the

variation in the cation sizes, typically represented by the ratio of the A- and B- cation radii (r_A/r_B) [19]. Thus, the larger this ratio (*e.g.* large A-cations and small B-cations like $Sm_2Ti_2O_7$), the more readily the compound amorphizes. Compounds with smaller radius ratios (*e.g.* $Gd_2Zr_2O_7$ [96]) do not amorphize at all, transforming into disordered, anion-deficient fluorite structures. Despite the depth of literature on this topic, much recent attention, with advanced characterization techniques, has been paid to the structural peculiarities of pyrochlore oxides. For instance, using neutron total scattering with pair distribution function analysis, it has been shown that $A_2B_2O_7$ compounds that adopt the disordered fluorite structure (*e.g.* $Ho_2Zr_2O_7$) actually exhibit short-range order that is nearly indistinguishable from the atomic configuration of A_3BO_7 weberite-type oxides [17][15][14]. More intriguingly, this short-range weberite-type ordering is observed in disordered pyrochlore oxides, regardless of how the disorder was introduced and what form of long-range order is exhibited; the same weberite-type order has been identified in ion-disordered and ion-amorphized pyrochlore oxides [18][16].

Given the apparent preference of certain ternary complex oxides to adopt the weberite-type local atomic configuration either governed by chemical disorder or subjected to swift heavy irradiation conditions, we report here the first systematic study of A_3BO_7 weberite-type compounds under swift heavy ion exposure. Using a variety of chemical compounds that span a wide range of cation radius ratios and two different experimental scattering approaches, we probed the radiation stability of both the long-range weberite-type crystal structure and short-range weberite-type structural building block. Synchrotron XRD and neutron total scattering experiments reveal that weberite-types accumulate an amorphous phase under ion exposure, the formation rate of which correlates directly with the variance of cation sizes. Cation size ratios have previously been correlated with the propensity for *compositional* disorder in pyrochlores, a defect

mechanism that is an accessory in weberite-types; instead, here, we show that the variance of cation radii correlates with *displacive* disorder, a necessary ingredient in preserving the local structural building block and the mechanical properties of these structures.

6.3 Results and discussion

6.3.1 *Amorphization Resistance: Irradiation with 946 MeV Au ions*

Assessment of synchrotron X-ray diffraction (XRD) data of all weberite-type samples, as well as the reference pyrochlore, weberite, and fluorite samples, confirms that the pristine materials are well-crystallized with no apparent phase impurities. All details on structural characteristics of the unirradiated weberite-type materials are provided elsewhere [28], [33], while the patterns of three other reference materials were indexed with the *Fd-3m* structural model for $Ho_2Ti_2O_7$ (ordered pyrochlore) pyrochlore [97], the *Fm-3m* structural model for $Ho_2Zr_2O_7$ (disordered, defect fluorite) [15] and the *Imma* structural model for $Sr_2Sb_2O_7$ weberite[98].

Synchrotron XRD reveals the radiation response of weberite-type oxides, and in particular the susceptibility to amorphization to 946 MeV Au ions (**Figure 6.1**). Ion-beam-induced amorphization is apparent in XRD patterns as a broad diffuse scattering signal that increases in intensity with increasing irradiation fluence. The sharp diffraction maxima of the crystalline phase, instead, broaden and decrease in intensity [10]. This behavior is observed in the diffraction patterns of all tantalate weberite-type compounds of the three structural families (**Figure 6.1**). This means that, like many other complex oxides [12] such as many pyrochlore compounds [19], weberite-type tantalate oxides are amorphizable under swift heavy ion irradiation. The susceptibility to amorphization is highest for the compound in family I (Pr_3TaO_7), decreases to family II (Tb_3TaO_7),

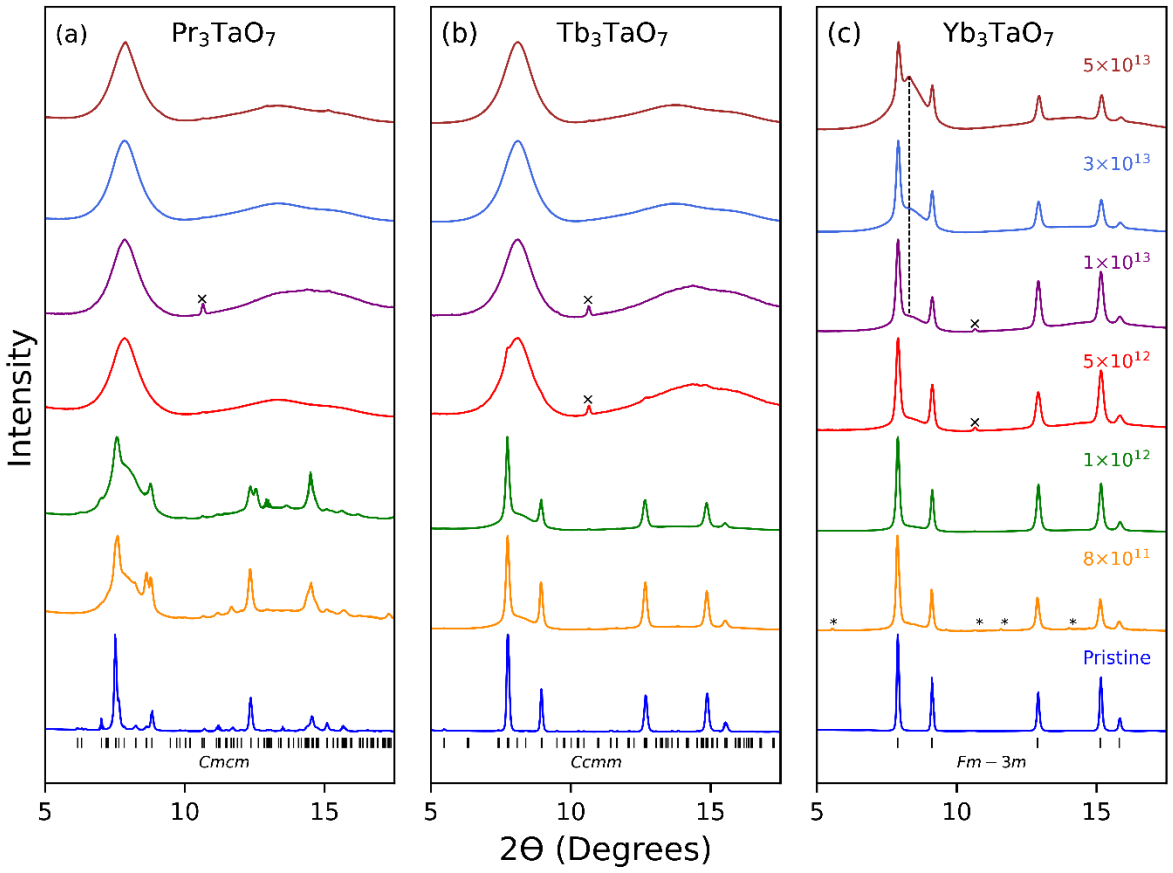

Figure 6.1: Stacked, normalized XRD patterns for (*a*) Pr_3TaO_7, (*b*) Tb_3TaO_7 and (*c*) Yb_3TaO_7 weberite-type oxides representing compositional changes in the A-cation and three respective structural families. X-symbols in some measurements (particularly 5×10^{12} and 1×10^{12} ions/cm^2) indicate diffraction maxima from the Mo sample chamber. For Yb_3TaO_7, in the diffraction data at 8×10^{11} ions/cm^2 fluence, asterisk (*) symbols indicate small impurity, which is only detected in this particular fluence point measurement.

and is the lowest for the compound in family III (Yb_3TaO_7). This can be seen, for example, in the patterns of the 5×10^{12} ions/cm^2 fluence step: the XRD pattern of Pr_3TaO_7 (**Figure 6.1a**) has no remaining crystalline diffraction peaks, while remnants of the most intense Bragg peak are still visible for the XRD pattern of Tb_3TaO_7 (**Figure 6.1b**) as a small shoulder, and only low levels of diffuse scattering are visible in the XRD pattern of Yb_3TaO_7 (**Figure 6.1c**). All samples were simultaneously irradiated by the same ion beam, so even small changes in the XRD patterns are significant. Although Pr_3TaO_7 and Tb_3TaO_7 are fully amorphous after irradiation to the highest fluence used in this study (5×10^{13} ions/cm^2), the XRD pattern of Yb_3TaO_7 (**Figure 6.1**) retains all characteristic diffraction maxima for the fluorite phase of the pristine sample; however, pronounced diffuse scattering is also observed with the indication of an additional sharper Bragg peak at ~8 degrees two theta. To more quantitatively analyze the crystalline-to-amorphization transformation induced under irradiation, all XRD patterns were decomposed [99] to extract the amorphous phase fractions at each fluence for the tantalate weberite-type compounds of the three families (**Figure 6.2**). This fraction increases linearly at lower fluences, reaching saturation at higher fluences with a gradual transition between both regimes at intermediate fluences. This fluence-dependent accumulation behavior is in good agreement with a single impact mechanism [62], [100] (Eq. 3.5), in which each ion adds to the amorphous phase fraction, f_a, by transforming the crystalline material into an amorphous state along its path. This procedure also yields the areal cross section, σ, and therefore the diameter, d, of the track, assuming cylindrical geometry ($\sigma = (d/2)^2 \cdot \pi$).

Consistent with the more qualitative trend seen in the XRD patterns (**Figure 6.1**), the extracted amorphous cross-section is higher for Pr_3TaO_7 than for Tb_3TaO_7. Pr_3TaO_7, Tb_3TaO_7, and

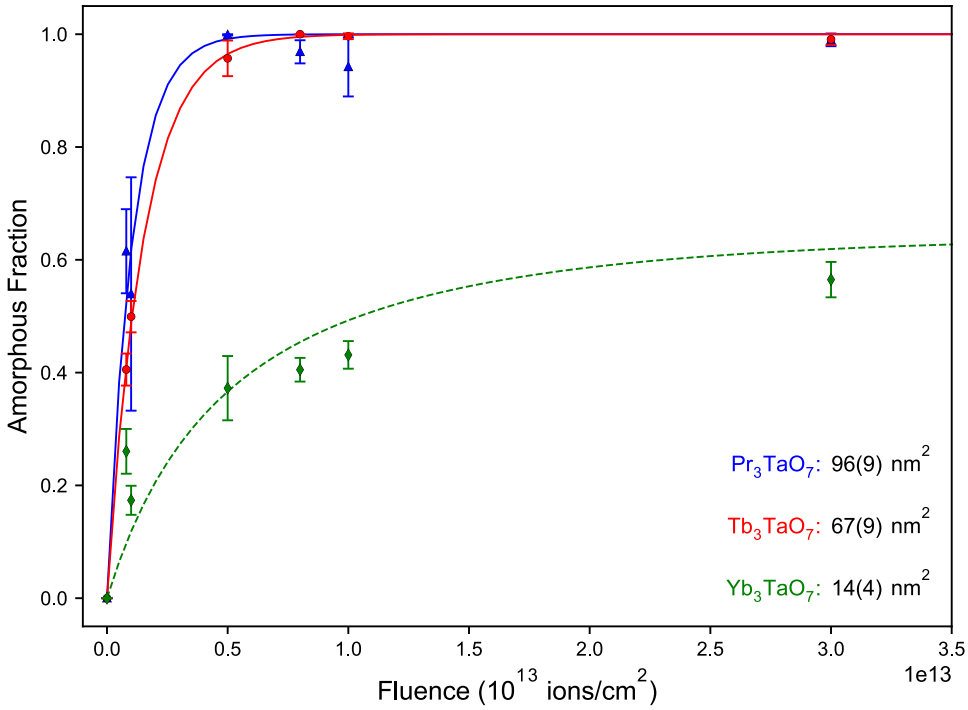

Figure 6.2: Fits of the single impact model (Eq. 3.5.) to the ion-induced amorphous fractions for Pr_3TaO_7, Tb_3TaO_7 and track overlap model (Eq. 3.6.) for Yb_3TaO_7. Uncertainties in the amorphous fractions arise from the deconvolution of multiple XRD patterns, and uncertainties in the amorphous cross section arise from fitting of the models to the amorphous fractions.

Dy_3TaO_7 (not shown) completely amorphize (100% amorphous phase fraction) while Yb_3TaO_7 retains 30-40% crystallinity up to the highest ion fluence (**Figure 6.2**). The appearance of an additional, sharper diffraction maximum at the highest fluence (**Figure 6.1**) indicates that the Yb_3TaO_7 compound has a more complex damage accumulation behavior. An amorphous core and a recrystallization shell can explain such incomplete amorphization, which has been experimentally observed for swift heavy ion tracks in many pyrochlore compounds [13], [101]. Molecular dynamics has revealed [102], [103] that such a shell can form as a result of recrystallization processes following a thermal spike [104], leaving an amorphous core behind because the recrystallization is incomplete. In both titanate and stannate pyrochlores, the shell is, in general, disordered and displays the defect-fluorite structure [13], [63], [105]. To better describe the evolution of damage in Yb_3TaO_7, the track core was assumed to be amorphous and the surrounding recrystallization shell was considered to have a cubic X-phase [106], [107] as supported by the Rietveld analysis of the observed reflections. Both the evolution of the amorphous phase fraction (peak deconvolution) and the X-phase (Rietveld refinement) as a function of fluence were used to fit the track overlap model and extract the accurate value of the amorphous cross section. As also qualitatively shown by the slopes of the linear regime in **Figure 6.2**, the track size is larger for Pr_3TaO_7 and gradually decreases across the tantalate series with decreasing ionic radius of the A-site lanthanide ion, following the usual lanthanide contraction [108], with the smallest track size in Yb_3TaO_7.

To test the effect of the B-site cation on the amorphization resistance of weberite-type oxides, three family II members Tb_3NbO_7, Tb_3TaO_7, and Tb_3SbO_7 were irradiated, and their response compared with each other (**Figure 6.3**). The fluence-dependent behavior is very similar to that of the tantalate compounds with changing A-site cation (**Figure 6.1**) and all three samples

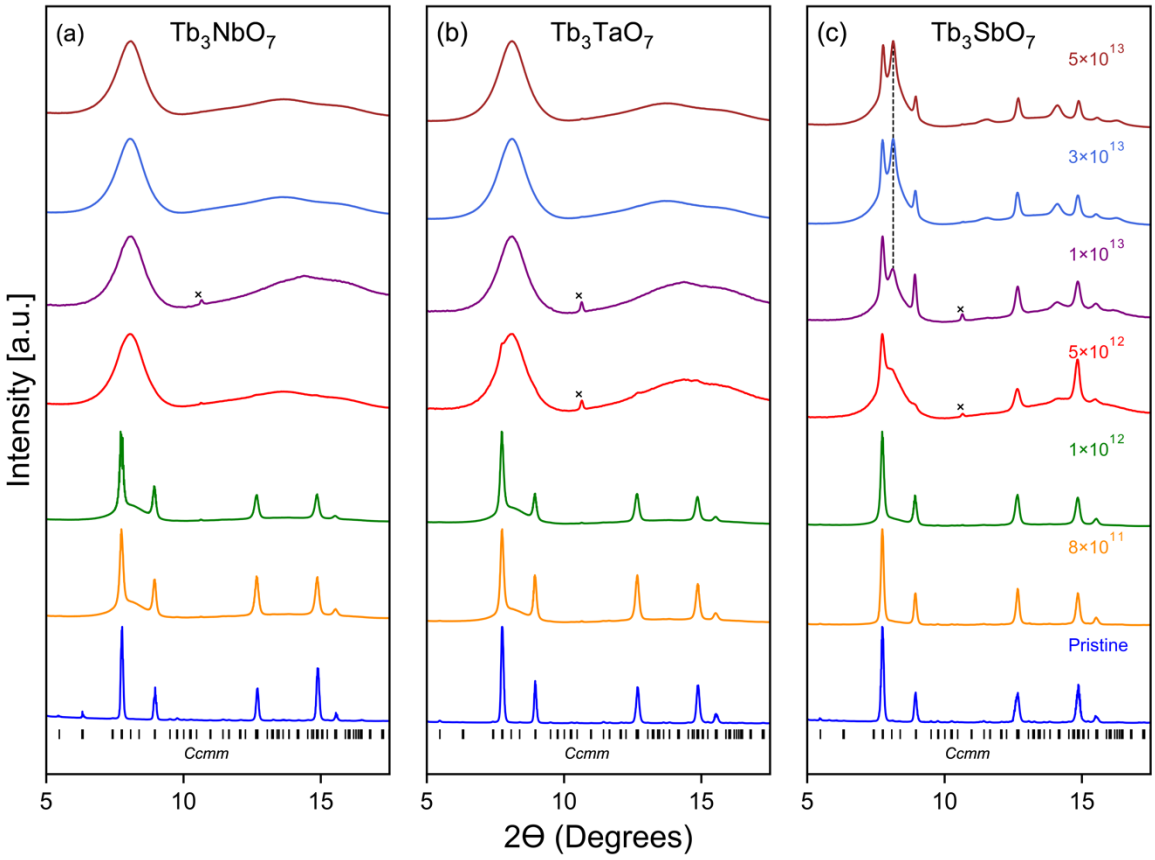

Figure 6.3: Stacked normalized XRD patterns for (*a*) Tb_3NbO_7, (*b*) Tb_3TaO_7 and (*c*) Tb_3SbO_7 weberite-type oxides representing compositional changes in the B-cation. X-symbols in some measurements indicate diffraction maxima from the Mo sample chamber. For Tb_3SbO_7, the dashed gray line at high fluences denotes the emergence of a Bragg peak corresponding to a distinct crystalline phase.

are amorphizable. Both Tb_3NbO_7 and Tb_3TaO_7 exhibit an almost identical radiation response, with the latter having slightly enhanced radiation resistance as evidenced by the small shoulder peak in the XRD pattern at 5×10^{12} ions/cm^2 (**Figure 6.3b**). Tb_3SbO_7 (**Figure 6.3c**) has a large remnant crystalline fraction at the maximum fluence, consisting of the original weberite-type phase and a clearly discernable new irradiation-induced phase. The most intense Bragg peak of the new phase at ~8 degrees becomes apparent at 5×10^{12} ions/cm^2 and grows in intensity with increasing fluence. Two additional weaker peaks of the new phase are detectable at ~11 and ~14 degrees two theta, respectively. Rietveld refinements were performed with several structural models, while the diffuse scattering of the amorphous contributions was modeled using a broad Gaussian background. The best agreement between the structural model and the experimental data was obtained with a mixture of two phases: the original *Ccmm* structure (low fluence points) or a defect-fluorite *Fm-3m* structure (high fluence points) and an X-type structure described by *Im-3m* model. The cubic X-type phase is an unquenchable high-temperature phase of sesquioxides with medium to large cations (*e.g.*, La_2O_3, Tb_2O_3, and Dy_2O_3) [109], but has also been reported to stabilize under ambient conditions in swift heavy ion-irradiated sesquioxides with smaller cations for which the X-type phase is not part of the phase diagram (Tm_2O_3, Yb_2O_3, and Lu_2O_3) [106], [110]. The thermodynamics and phase diagram of Tb_3SbO_7 and its constituent oxides Tb_2O_3 and Sb_2O_5 provide potential information on the formation process of the X-type phase in a weberite-type oxide under ion irradiation. Rietveld refinement shows that this scenario agrees with the broader diffraction maxima observed in the XRD patterns. The Sb_2O_5 byproduct of the decomposition is not apparent as a crystalline phase in the pattern, but may be part of the diffuse scattering background. It has been shown before that pentoxides like Ta_2O_5 are susceptible to radiation-induced amorphization [111]. Swift heavy ion-induced chemical decomposition

processes have been observed before in some materials [112] and were attributed to differential thermal effects associated with the thermal spike; in fact, the melting point of Sb_2O_5 is only 380 °C.

The evidence of an X-phase with *Im-3m* symmetry in the XRD pattern of Tb_3SbO_7 (**Figure 6.3c**) supports the idea that a similar phase is also present as a minor contribution to the XRD pattern at the highest fluence of Yb_3TaO_7 (**Figure 6.1c**). Therefore, a complex core-shell track morphology was used for Tb_3SbO_7 to extract individual phase contributions after peak deconvolution and Rietveld refinement; however, in the case of Tb_3SbO_7, the track structure is more complex with at least two crystalline phases (weberite-type and X-type) and an amorphous contribution. This was used in conjunction with the track overlap model [63] to fit the fluence-dependent phase fractions and deduce the respective cross sections (**Figure 6.4**). However, the main purpose of this study is to compare the amorphization resistance of different weberite-type oxides, and the crystalline shell and halo have only minor impact on the amorphous cross section, the amorphous phase fraction, and the associated amorphization resistance. Finally, the amorphous phase fractions for the two other compounds of the B-site cation series, Tb_3NbO_7 and Tb_3TaO_7 (Figs. 3a and 3b) were deduced by simple peak deconvolution, as no other crystalline phases were apparent in the XRD patterns, and the fluence-dependent growth of the amorphous phase fraction agrees well with a single impact behavior (**Figure 6.4**).

To compare the amorphization resistance of a weberite-type structure with other fluorite-derived structures, the weberite-type Y_3TaO_7 with $C222_1$ symmetry [46] was irradiated with swift heavy ions and compared to $Sr_2Sb_2O_7$ weberite, ordered $Ho_2Ti_2O_7$ pyrochlore, and disordered fluorite $Ho_2Zr_2O_7$ (**Figure 6.5**). A disordered fluorite with the A_3BO_7 stoichiometry (Yb_3TaO_7) shown above in **Figure 6.1**. Swift heavy ions completely amorphize $Sr_2Sb_2O_7$ weberite and

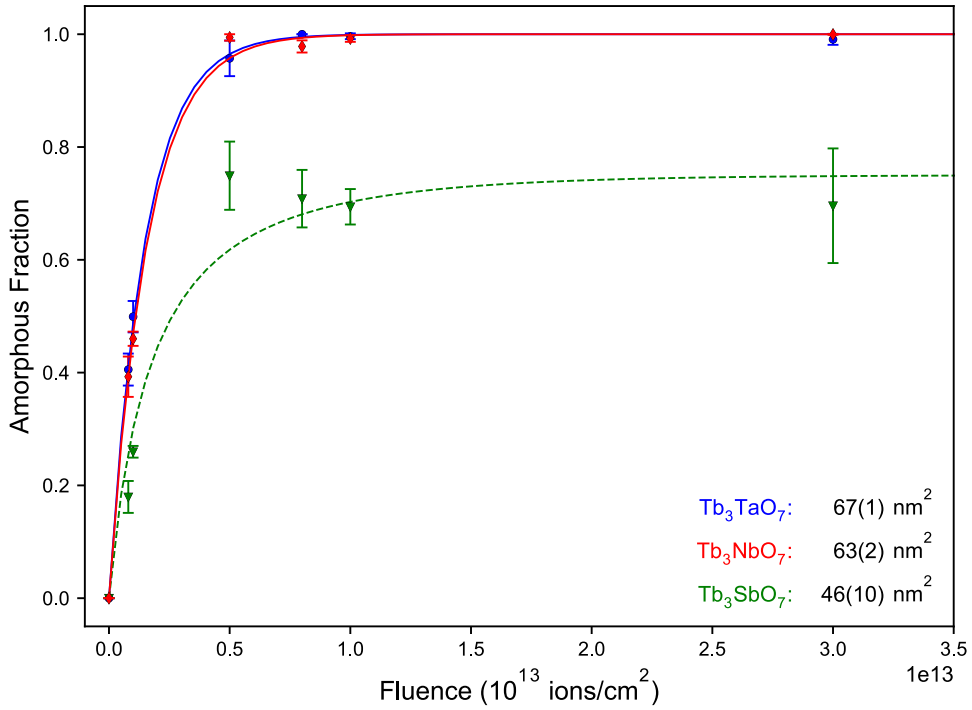

Figure 6.4: Fits of the single impact model (Eq. 3.5.) to the ion-induced amorphous fractions for Tb_3TaO_7, Tb_3NbO_7 and track overlap model (Eq. 3.6.) for Tb_3TaO_7. Uncertainties in the amorphous fractions arise from the deconvolution of multiple XRD patterns, and uncertainties in the amorphous cross section arise from fitting of the models to the amorphous fractions.

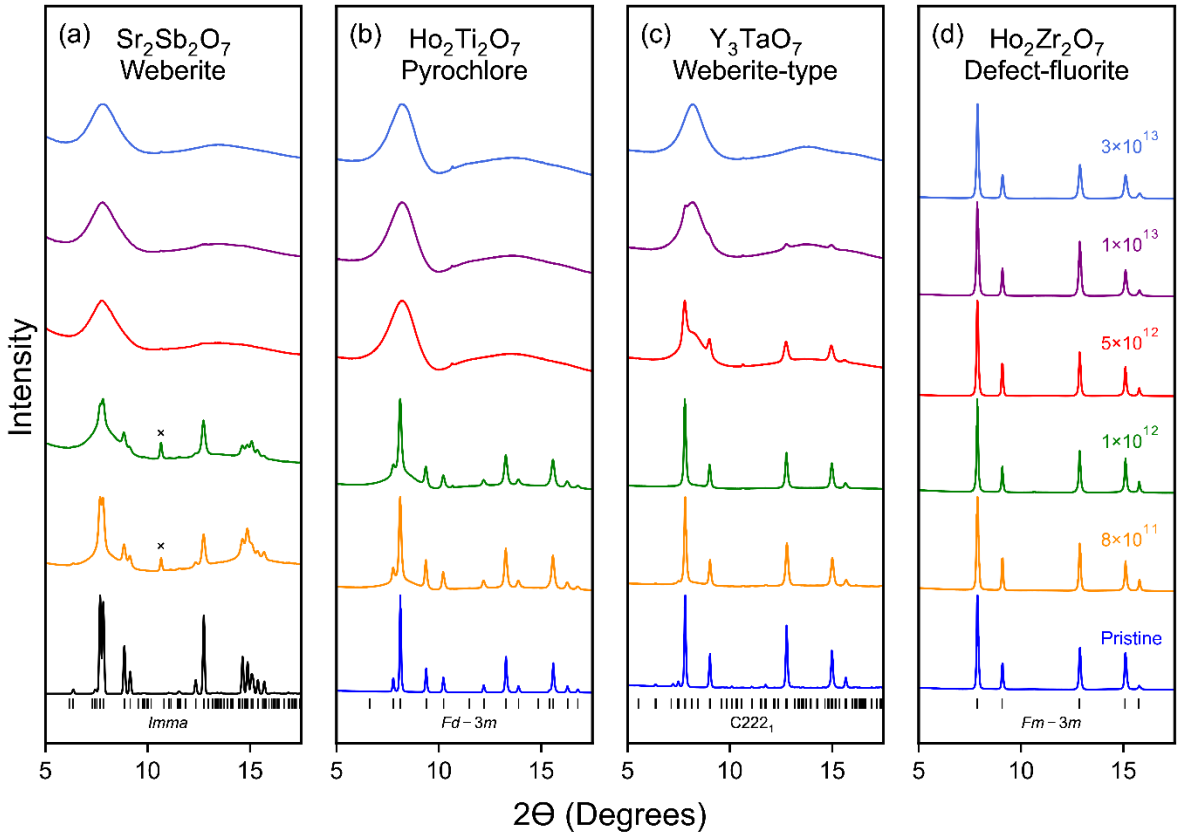

Figure 6.5: Stacked, normalized XRD patterns for (*a*) $Sr_2Sb_2O_7$ weberite (*b*) $Ho_2Ti_2O_7$ pyrochlore (*c*) Y_3TaO_7 weberite-type, and (d) $Ho_2Zr_2O_7$ fluorite oxides representing four distinct structural families. X-symbols in some measurements indicate diffraction maxima from the Mo sample chamber. The XRD pattern of the unirradiated $Sr_2Sb_2O_7$ weberite (black line in *a*) was simulated using Rietveld refinement of neutron diffraction data collected from the unirradiated $Sr_2Sb_2O_7$ weberite.

$Ho_2Ti_2O_7$ pyrochlore (**Figure 6.5a**) at a fluence of 5×10^{12} ions/cm^2 in agreement to previous work on similar pyrochlore compounds [19]. A qualitative comparison of SXRD patterns with the other weberite-type oxides (**Figures 6.1** and **6.3**) shows that the increase in amorphous phase with fluence is comparable to Tb_3NbO_7 (**Figure 6.3a**). The Y_3TaO_7 weberite-type sample is distinctly more resistant against amorphization than the other weberite-type tantalates (except Yb_3TaO_7 which shows evidence of an X-type crystalline phase) and it retains some level of crystallinity up to a fluence of 1×10^{13} ions/cm^2 (**Figure 6.5b**). The disordered fluorite $Ho_2Zr_2O_7$ is the only compound in the entire irradiation series that does not show any evidence of amorphization, and the crystalline Bragg peaks in the XRD patterns show only small peak broadening and reduction in intensities up to 5×10^{13} ions/cm^2 (**Figure 6.5c**). This agrees well with swift heavy ion irradiation studies of other disordered zirconate pyrochlores, such as $Gd_2Zr_2O_7$ [10]. The weberite-type Yb_3TaO_7 also has the same defect-fluorite structure, but shows evidence of amorphization under ion irradiation, suggesting that stoichiometry and/or chemical composition are critical components of amorphization resistance. The same peak deconvolution procedure was used as before to extract the amorphous phase fraction for $Sr_2Sb_2O_7$, Y_3TaO_7, and $Ho_2Ti_2O_7$ and the fluence-dependent evolution is well described by a single impact behavior (**Figure 6.6**). A summary of the amorphous phase fractions of all materials at each fluence step is shown in **Figure 6.7**, along with the fits based on the heterogeneous damage accumulation model for Yb_3TaO_7 and Tb_3SnO_7 as well as the single impact model for all other materials.

Irradiation with 946 MeV Au ions reveals a large variation in the radiation response of weberite-type oxides of different chemical composition. Each material shows single-impact amorphization (Eq. 3.5.) with only two compounds that exhibit additional evidence of crystalline to crystalline transformation and a more complex track morphology (Yb_3TaO_7 and Tb_3SnO_7). To

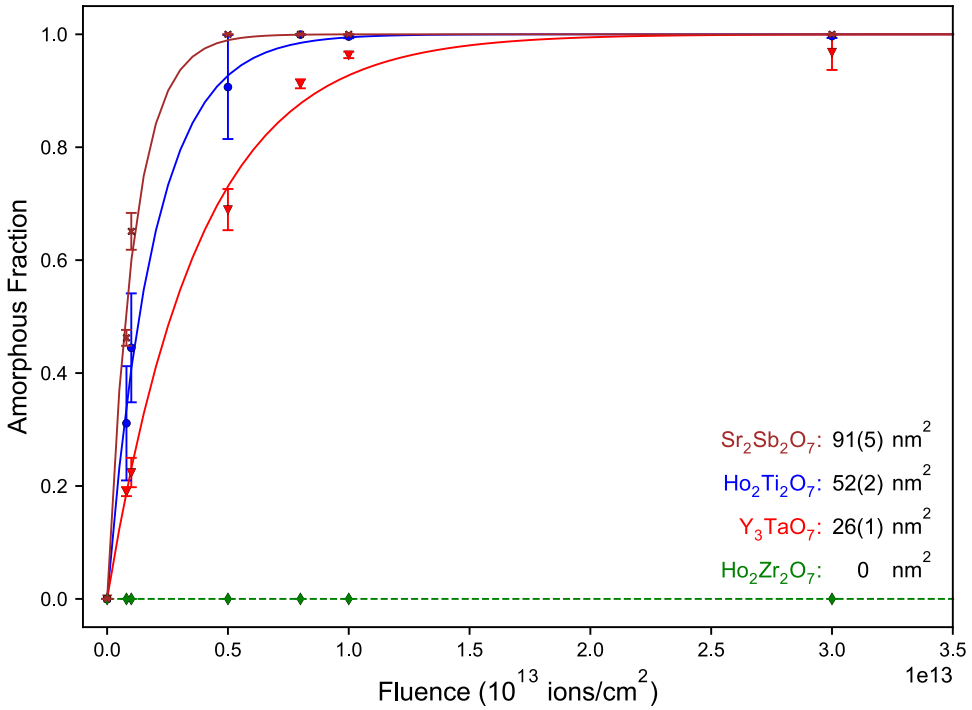

Figure 6.6: Fits of the single impact model (Eq. 3.5) to the ion-induced amorphous fractions for $Sr_2Sb_2O_7$, $Ho_2Ti_2O_7$, Y_3TaO_7, and $Ho_2Zr_2O_7$. Uncertainties in the amorphous fractions arise from the deconvolution of multiple XRD patterns, and uncertainties in the amorphous cross section arise from fitting of the models to the amorphous fractions.

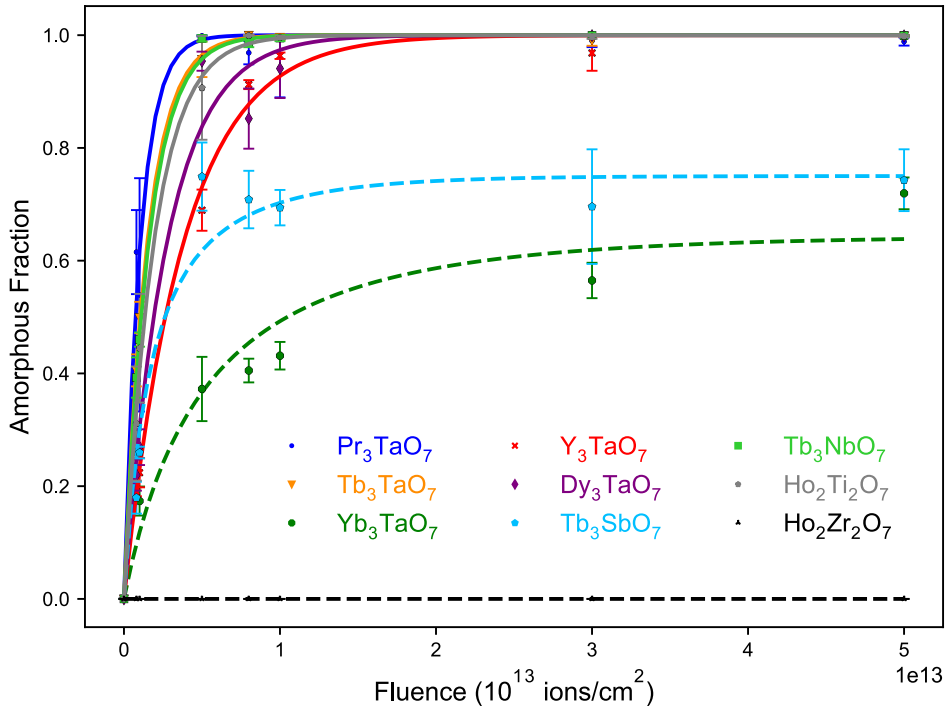

Figure 6.7: Summary of ion-induced amorphous fractions (f_a) in all compounds considered. For most compounds, the amorphous fraction is fit with the single impact model (Eq. 3.5) and shown with the solid line corresponding to the color of the dataset. For Tb_3SbO_7 and Yb_3TaO_7, the track overlap model (Eq. 3.6) was fit and shown with a dashed line in the color of the data set. The black dashed horizontal line at $f_a = 0$ represents $Ho_2Zr_2O_7$ which did not exhibit amorphization. Uncertainties in the amorphous fractions arise from the deconvolution of multiple XRD patterns, and uncertainties in the amorphous cross section arise from fitting of the models to the amorphous fractions.

better understand the influence of chemical composition on the radiation response of all weberite-type and pyrochlore oxides studied here, the amorphous cross section of each compound was considered against relative sizes of the two cations (**Figure 6.8**). In pyrochlore oxides, the ratio of A and B cation radii (r_A/r_B) has been shown to correlate inversely with the tolerance to amorphization [7], [113]; this property cannot be directly compared with those of weberite-types due to the difference in stoichiometry ($A_2B_2O_7$ *versus* A_3BO_7). However, the statistical variance of the cation sizes ($\sigma^2 = \langle r^2 \rangle - \langle r \rangle^2$) [114], which has been previously shown to be highly correlated with the expression of physical properties in complex oxides [115]–[117], is generalizable to all ionic chemical compounds. The smallest cross section for all weberite-type compounds irradiated in this study is observed for family III compound Yb_3TaO_7, which exhibits the smallest cation size variance, and the largest amorphous cross section is observed for the family I compound Pr_3TaO_7, which exhibits the largest cation size variance, with a monotonic increase in-between. This suggests that the relative size difference of the two cations (cation size variance) is an important parameter to consider in evaluating the resistance of weberite-type oxides to amorphization.

Due to their nuclear applications, complex oxides have been the focus of many studies cataloging their response to radiation exposure for use in radiological environments [4]. For example, pyrochlore oxides are among the most studied complex oxides with respect to ion irradiation for the purpose of evaluating their use as actinide-immobilizing nuclear wasteform [95]. It is, therefore, of interest to benchmark the radiation response of weberite-type oxides, which have never been irradiated before, to those structurally related materials (both are different super structures of the parent fluorite). If Pu and "minor" actinides [95] are incorporated as A-site cations in the weberite-type structure, these ceramics may offer much higher flexibility than pyrochlores

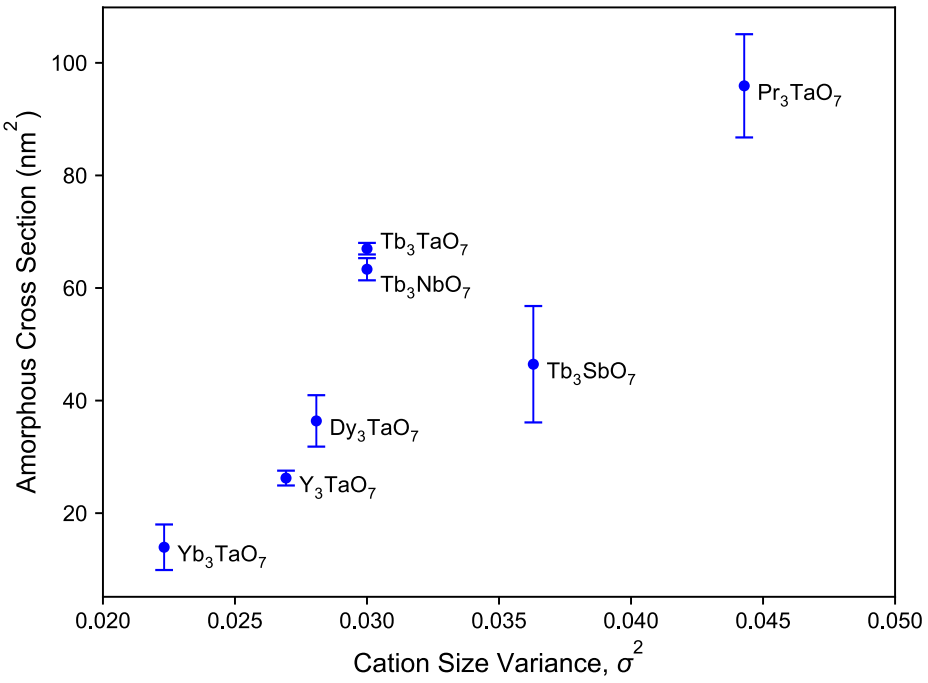

Figure 6.8: Amorphous cross sections of each weberite-type compound considered in this study, extracted from either the single impact (Eq. 3.5.) or track overlap (Eq. 3.6.) models, *versus* cation size variance.

because they exhibit a greater variety of atomic environments that are certainly more adapted to the specific chemical requirements of each different minor actinide; however, radiation resistance is an important factor for waste forms that requires further investigations.

Qualitatively, the increase in amorphous area with the increase in ionic radius for the weberite-types is in agreement with the findings of previous swift heavy ion irradiation studies on other complex oxides. For example, Shamblin *et al.* [19] and Tracy *et al.* [63], [118] reported that the mean diameter of the amorphous tracks in titanate ($A_2Ti_2O_7$) and stannate ($A_2Sn_2O_7$) pyrochlores, induced by 2.2 GeV Au ions, increases with the ratio of the ionic radius of both cations, r_A/r_{Ti} and r_A/r_{Sn}, respectively. The same overall radiation behavior is observed for ion-beam experiments that used lower ion energies damaging the target materials through ballistic interactions within the nuclear energy loss regime (*e.g.*, 1 MeV Kr^+ ions [119]). However, when comparing the weberite-type results of this study with previous work on pyrochlores based only on the $Ho_2Ti_2O_7$ and $Ho_2Zr_2O_7$ pyrochlore reference materials that were simultaneously irradiated with all weberite-type samples, the comparison is not straightforward, given the difference in mass density and resulting lineal ion energy loss, or dE/dx. Therefore, we have expanded on a previous study of a series of swift heavy ion (2.2 GeV Au) irradiated $A_2Ti_2O_7$ series [19] and plotted the amorphous track diameters, normalized with the electronic energy loss (dE/dx) in each sample, as a function of the cation size variance (**Figure 6.9a**) [19]. There is a clear evolution of the track diameter with the cation size in both series and weberite-type oxides, showing larger amorphous track diameters; however, the kinetic energy (and velocity) of the two-ion beam series is different (946 MeV Au *versus* 2200 MeV Au), which must also be considered for an accurate comparison. The lower kinetic energy used in this study will result in a higher energy density within the ion tracks, enhancing the effects of radiation damage effects, as previously reported [120], [121]. This

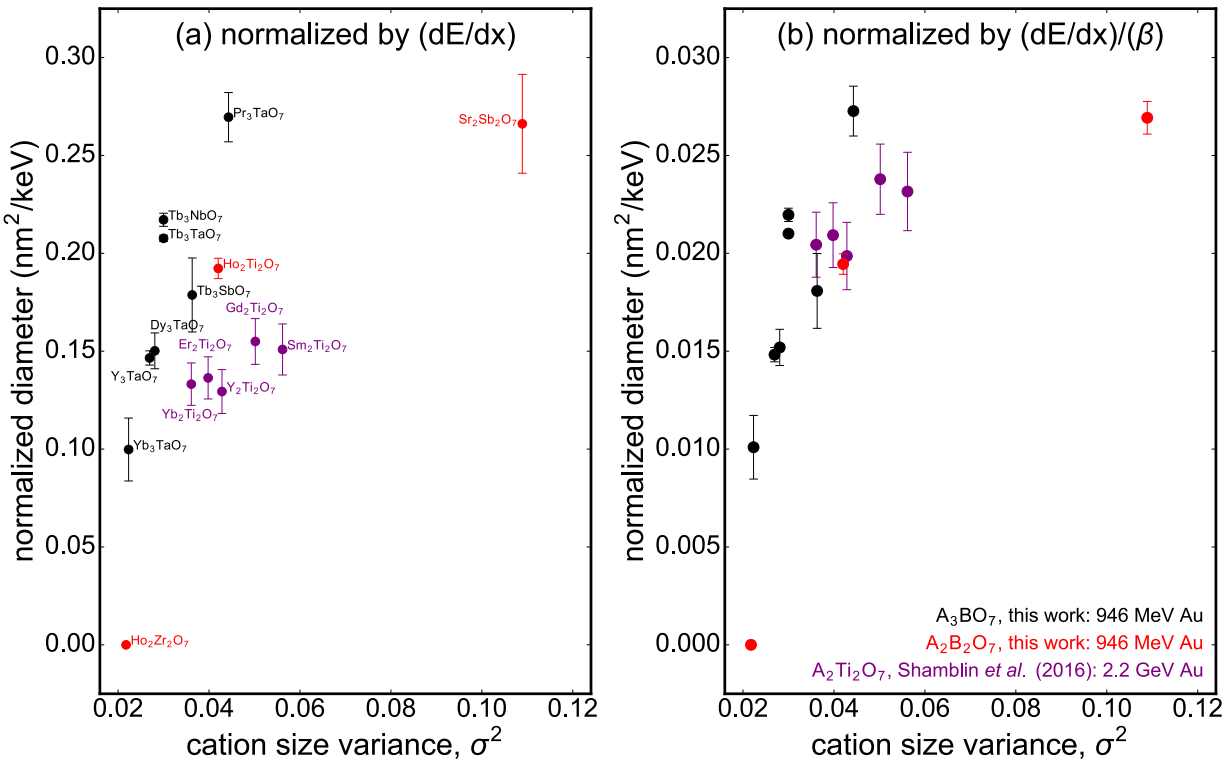

Figure 6.9: Diameter of the amorphous cross section for each compound considered in this study, along with data from [19], (*a*) normalized by the value of the electronic energy loss of ions and (*b*) normalized by both the energy loss and the ion velocity. Data for A_3BO_7 weberite-type oxides (black circles) are compared with the $A_2B_2O_7$ pyrochlore and weberite (red circles) from this study with previous irradiation of $A_2B_2O_7$ pyrochlore irradiated with 2.2 GeV Au ions (purple circles [19]). Vertical solid lines denote uncertainty calculated in the amorphous diameter, extracted from the fits of the two models.

can be clearly seen for the $Ho_2Ti_2O_7$ diameter, which is larger, after normalization by d*E*/d*x*, for the lower ion energy than in similar titanate pyrochlores irradiated with higher energy ions. Therefore, additional normalization beyond just energy loss is required to account for this so-called "velocity-effect," which accounts for the inverse relation between ion velocity and deposited energy density in the ion track, given comparable values of d*E*/d*x*. Recently, Wesch *et al.* [121] developed an approach to determine the diameter of the track of complex oxides irradiated with swift heavy ions and its relation to the electronic energy density induced based on an empirical parameter. We followed the same procedure and performed a second normalization of Figure 9*a* using the reduced ion velocity $\beta = v/c$, with v being the ion velocity at the sample surface and c the speed of light (we assumed a $k = 0.25$ in this approach, which was found to be a universal parameter for many target materials [121]). This secondary normalization reduced the discrepancy between the diameter data of both series (**Figure 6.9b**) and, therefore shows that the energy density must be considered (note, the behavior of $Ho_2Ti_2O_7$ irradiated in this study with 946 MeV Au now follows the general trend of other pyrochlores after this normalization). After normalization, several conclusions can be drawn by comparing and contrasting the diameters of these fluorite-derived complex oxides: (*i*) for a given cation-size variance, weberite-type compounds have larger amorphous tracks than pyrochlores, (*ii*) weberite-type materials can exhibit low values of cation-size variance and can be more resistant to amorphization by choosing small cation-size variance values, and (*iii*) the track-diameter evolution has a distinctly higher slope vs. cation variance for weberite-type oxides than for pyrochlore oxides. Previous studies have shown that the size of the cation is not the only parameter to consider, but also the character of the chemical bonding [122] or the amorphization energy [123] play an important role. However, the evolution of cross section *versus* cation size variance (**Figure 6.9**) shows that the chemical composition and the variability

of cation sizes are strongly correlated and can play a key role in the radiation response of these systems.

Recently Uberuaga *et al.* [7] succinctly stated, “In oxides…such as fluorite derivatives, amorphization resistance inversely correlates with the ability of the oxide to disorder.” Specifically, in pyrochlore oxides, it has been demonstrated [4] that the cost of cation antisite disorder, the basis for the order-disorder transformation, which is the alternative to amorphization, is directly correlated with the variance in sizes between the A- and B-site cations (cationic ratio r_A/r_B). Therefore, our results would suggest that the cation antisite energy for weberite-type oxides also correlates with the variance in cation sizes. However, other material properties also affect the response of these materials to swift heavy ions, with the conclusion (*iii*) above implying that weberite-type oxides are more sensitive to changes in the cation size than pyrochlores. The cation species in the pyrochlore and weberite types are different not only in size, but also in valence. In fact, the difference is greater in weberite-type (3+ and 5+) oxides than in pyrochlores (3+ and 4+) oxides and cation antisite defects should be greatly suppressed in weberite-types when considering Goldschmidt's rules (“*ions with charges different by one unit can readily substitute for each other, provided charge neutrality is maintained, while for ions whose charges differ by two units, substitution is limited”*) [124]. Therefore, while the variance in cation sizes is a good approximator for the general behavior of irradiated fluorite-derived oxides, the reason for this correlation may not be the same in pyrochlore and it is in weberite-types. The ion-irradiation structural compensation mechanism in pyrochlore, A- and B-site cation antisites is not as viable in weberite and weberite-type oxides because of the difference in charge states. Therefore, the cation size variance may be correlated with an additional compensation mechanism in weberite-type oxides, which is different from cation antisite defects.

Further studies are needed to better compare the radiation behavior of these ceramics. Irradiating the different sample series under identical ion-beam conditions will eliminate the need for energy-density corrections, which allows for a more direct comparison. Other characterization techniques must also be used to study in more detail the internal track structure of weberite-type materials. Like swift heavy-ion-irradiated pyrochlores, a core-shell track morphology may also be common in weberite-type oxides and present even in compositions for which XRD analysis only shows amorphization. The irradiation-induced crystalline phases in the XRD patterns of Tb_3SbO_7 and possibly Yb_3TaO_7 support this scenario. Amorphous track cores could also be embedded within shells of disordered fluorites in other weberite-type compounds. What is different in some weberite-type compositions (Tb_3SbO_7) is the formation of a new crystalline phase (X-type phase) as a result of ion irradiation distinct from the commonly observed disordered polymorph of the ordered matrix material (*i.e.*, defect fluorite shell in ordered pyrochlore). As mentioned above, this could point to an irradiation-induced decomposition of the complex oxide, which has not been reported before in pyrochlore oxides.

Characterization of long-range structures using X-rays is a powerful technique for investigating irradiation-induced amorphization or crystalline-to-crystalline phase transformations. However, SXRD experiments provide no information on atomic-scale structural configurations, particularly on oxygen sublattice, because of the limited sensitivity of X-ray probes to low-*Z* elements. Recent swift heavy ion beam studies have, instead, used neutron total scattering as a complementary approach to overcome these limitations in radiation effects characterizations [125]. These studies demonstrated that long-range structural changes are only a component of a larger picture, and irradiated materials exhibit atomic-scale phenomena that can be distinct and decoupled from longer-range behavior [14], [17]. Short-range weberite-type ordering was revealed

in ion-irradiated pyrochlore, regardless of whether the long-range structure was made amorphous or instead disordered to defect fluorite [18]. The complex core-shell track morphology, inferred from long-range techniques, consisting of an amorphous core, disordered fluorite shell, and defective pyrochlore halo was even shown to be described by the same weberite-type arrangement over the atomic-scale [13]. In fact, complex oxides with poor resistance to amorphization may actually be considered more structurally stable if short-range processes are considered [16]. This shows that multiscale characterization based on neutron probes with high sensitivity to both cations and oxygen sublattice is critical to better understanding the observed long-range structural changes in weberite-type materials. Such experiments are challenging due to the logistics necessary to produce the required homogeneously irradiated sample mass of ~100 mg [125], preventing detailed fluence series which require much higher incident ion energies. Therefore, we used deeply penetrating 1.46 GeV Au ions, with values of electronic energy loss *per* path length similar to that of the 946 MeV Au ions, to irradiate one member of each weberite-type structural family alongside reference weberite, pyrochlore, and fluorite materials for the purpose of conducting neutron total scattering experiments.

6.3.2 Multi-scale Structural Response: Irradiation with 1.46 GeV Au ions

Neutron and X-ray total scattering data was collected from Pr_3TaO_7, Tb_3TaO_7, and Yb_3TaO_7 before and after irradiation with 8×10^{12} 1.46 GeV Au ions/cm^2. Diffraction pattern analysis of the samples prior to radiation (black lines in **Figure 6.10**) confirms that the three samples represent the three structural families of rare-earth weberite-type tantalates: ordered *Cmcm* (**Figure 6.10a,d**), ordered *Ccmm* (**Figure 6.10b,e**), and disordered *Fm-3m* (**Figure 6.10c,f**). In addition to the sharp diffraction maxima, the diffraction patterns of the disordered fluorite-structured Yb_3TaO_7, particularly the neutron diffraction pattern, exhibit diffuse scattering alongside the crystalline

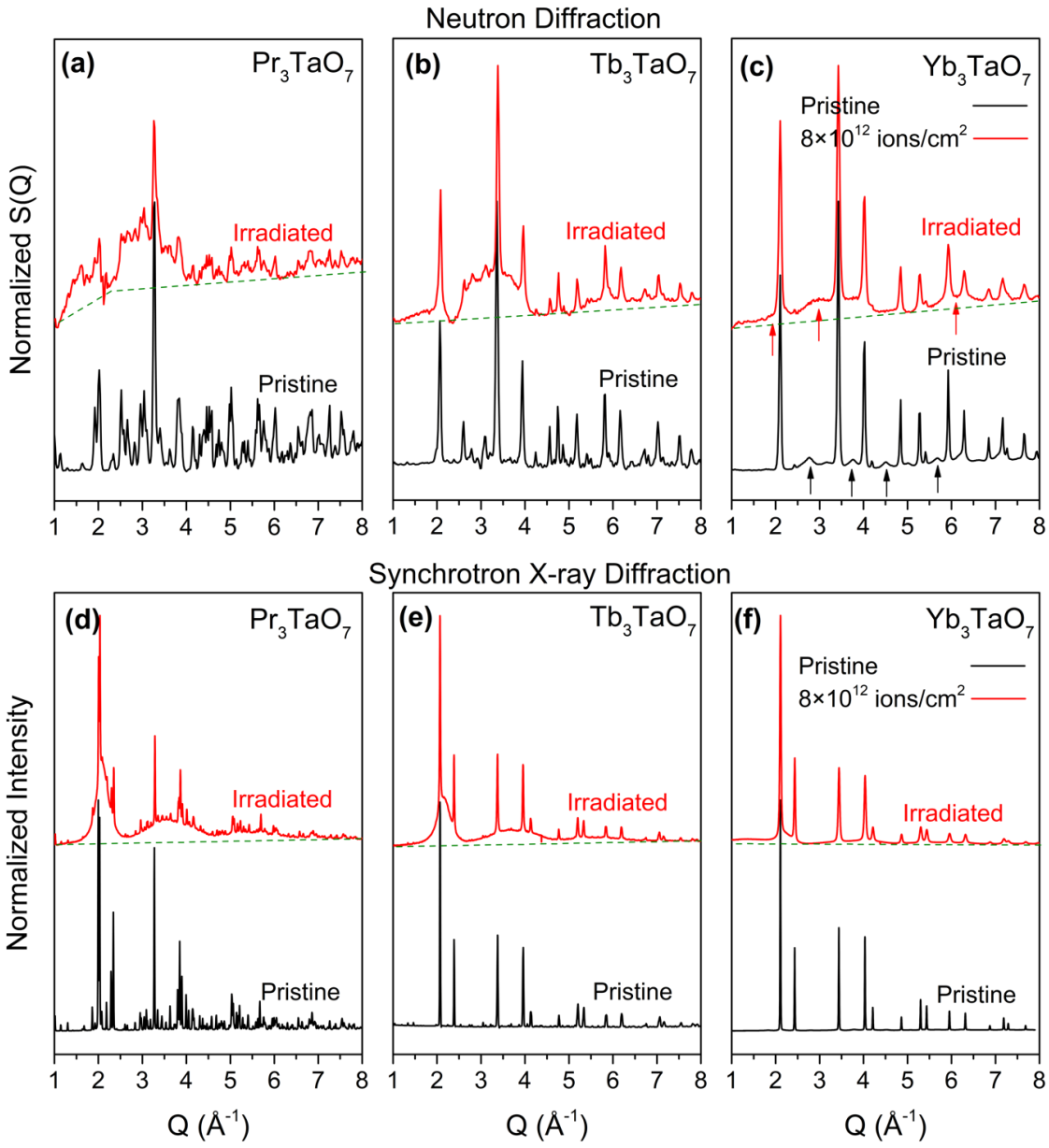

Figure 6.10: As collected, (0 to 1 normalized) synchrotron X-ray and neutron diffraction patterns of (*a*, *d*) Pr_3TaO_7, (*b*, *e*) Tb_3TaO_7, (*c*, *f*) Yb_3TaO_7 after ion irradiation with 1.46 GeV Au ions to a fluence of 8×10^{12} ions/cm^2 before (black) and after (red) ion irradiation with 1.46 GeV Au ions to a fluence of 8×10^{12} ions/cm^2. Pristine Pr_3TaO_7 (*a*) and Tb_3TaO_7 (*b*) samples are ordered weberite-type oxides with no diffuse scattering signal, while Yb_3TaO_7 (*c*), possessing long-range defect-fluorite structure shows a very prominent diffuse scattering signal, denoted by black arrows. All ion-irradiated samples demonstrate broad diffuse bands corresponding to amorphized regions. The black and red arrows in (*c*) denote the approximate positions of diffuse-scattering contributions. Structure factors are normalized to the intensity of the most intense peak within individual data, and the irradiated data are shifted vertically for ease of visualization. Diffuse scattering signal is not observed in SXRD of pristine Yb_3TaO_7.

peaks (denoted by black arrows in **Figure 6.10c**) characteristic of weberite-type short-range order (more details can be found elsewhere [45]). After irradiation, all diffraction patterns (red lines in Fig. 10) are characterized by two distinct characteristics: (*i*) sharp crystalline peaks that can be indexed using the same lattices of the corresponding pristine phases and (*ii*) intense, diffuse scattering signal with several broad contributions centered around 2.1, 3.6, and 5.5 $Å^{-1,}$ respectively. No other structural phase is observed in any diffraction pattern, which is in contrast to the Yb_3TaO_7 sample irradiated with 946 MeV Au ions in which an X-type phase was present. The crystalline peaks, while sharp, are distinct and broader than the corresponding peaks prior to irradiation. Broad, diffuse bands, indicative of amorphization, are the most intense, both in neutron and X-ray data, in the Pr_3TaO_7 diffraction pattern of Pr_3TaO_7, less so for $Tb_3TaO_{7,}$ and the least intense for Yb_3TaO_7. Furthermore, the specific characteristics of the diffuse scattering intensity of Yb_3TaO_7 are different after irradiation than before. Together, these two modifications to the diffraction patterns indicate that in the fluence evaluated (8×10^{12} ions/cm^2), all regions of the sample have been completely exposed to ions. In summary, the diffraction patterns of samples from the three weberite-type structural families before and after irradiation with 8×10^{12} 1.46 GeV Au ions/cm^2 reveal that all regions of the samples have been completely exposed to the ions and that the irradiated samples consist of a crystalline component with long- and short-range order and an amorphous component with only short-range order.

To comprehensively probe the structural response of these materials to radiation at the atomic-scale, neutron pair distribution functions (PDF) of Pr_3TaO_7, Tb_3TaO_7, and Yb_3TaO_7 weberite-type complex oxides were collected before and after irradiation with 8×10^{12} 1.46 GeV Au ions/cm^2 (**Figure 6.11**). Before irradiation (black curves in **Figure 6.11 a-c**), all samples are well-crystallized with a well-defined distribution of interatomic distances that are consistent with

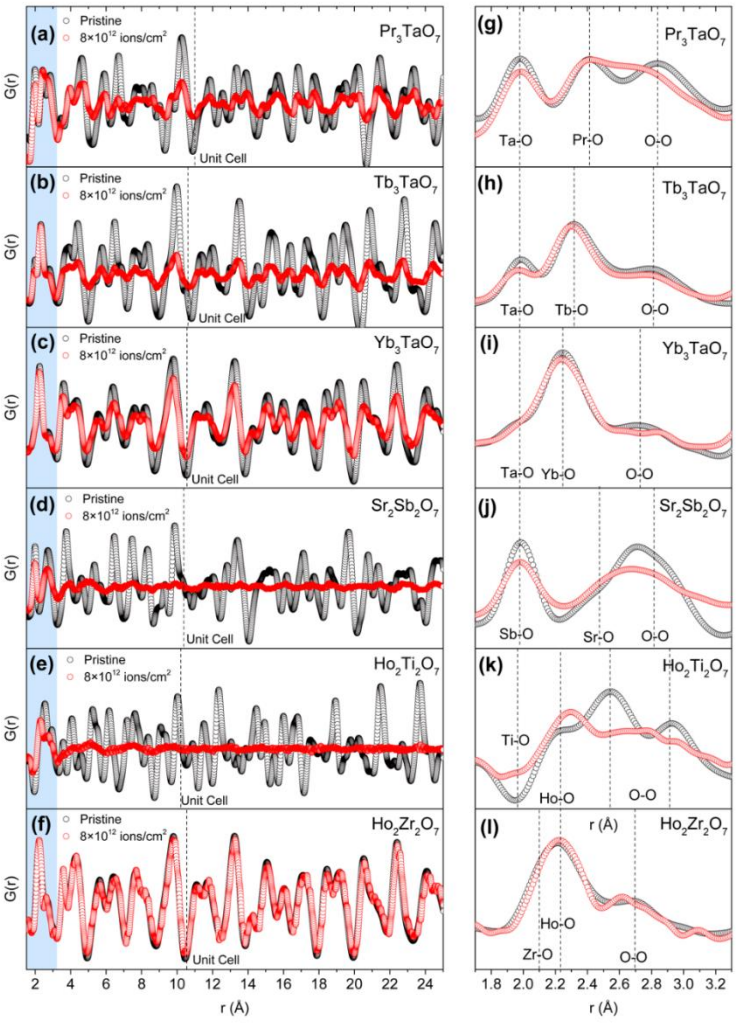

Figure 6.11: Neutron PDFs, $G(r)$ of Pr_3TaO_7 (*a*, *g*), Tb_3TaO_7 (*b*, *h*) weberite-type oxides, Yb_3TaO_7 (*c*, *i*) defect-fluorite weberite-type oxides, $Sr_2Sb_2O_7$ weberite (*d*, *j*), $Ho_2Ti_2O_7$ pyrochlore oxide (*e*, *k*) and $Ho_2Zr_2O_7$ defect-fluorite pyrochlore oxide (*f*, *l*) before (black circles) and after (red circles) irradiation with 1.46 GeV Au ions to a fluence of 8×10^{12} ions/cm^2 shown in a range of 1.5-25 Å (*a*-*e*) and 1.7 to 3.3 Å (*f*-*j*). The blue region from 1.7 to 3.3 Å in the left panel represents the nearest-neighbor distances characteristic of coordination polyhedra. Dashed lines in (*a*-*e*) represent the extent of the longest unit cell dimension (c-lattice in case of orthorhombic systems). The broadening and reduction in the intensity of the original weberite-type peaks indicate amorphization. In the right panel (*g*-*l*), vertical dashed lines denote the positions of A-O (A = Pr, Tb, Yb, Sr, Ho) and B-O (Ta-O, Sb-O, Ti-O, and Zr-O) as well as O-O nearest neighbor pairs in pristine samples. All weberite-type samples retain the original weberite-type peaks features; peaks become broader in irradiated samples, especially in (*a*). For Pr_3TaO_7 composition (*a*, *d*), the Q_{max} truncation value is set to 25Å^{-1} in both pristine and irradiated data for ease of comparison between the pristine and irradiated datasets. In all other cases, the Q_{max} truncation value is set to 31.4 Å^{-1}.

the weberite-type structural configurations (more detail can be found elsewhere [45]). After irradiation (red curves in **Figure 6.11 a-c**), the PDFs of all three samples exhibit a similar feature: the peaks corresponding to pair correlations are still present at the same radial positions, *r*, but with loss of peak area. This is consistent with loss of crystallinity [18]. Furthermore, among the samples evaluated here, the loss of crystallinity is most intense in the Pr_3TaO_7 sample, less intense in the Tb_3TaO_7 sample, and least intense in the Yb_3TaO_7 sample, a trend that agrees with the rate of development of the amorphous phase under 946 MeV Au irradiation. However, in the case of Yb_3TaO_7, no additional peaks are identified (**Figure 6.11*c***), whereas in the 946 MeV Au exposure, an X-type phase was observed. Therefore, as was the case for 946 MeV Au irradiation, 1.46 GeV Au amorphized weberite-type oxides from different structural families to different degrees; after 8×10^{12} ions/cm^2, each sample consists of an amorphous component and a damaged crystalline component.

The analysis of irradiated materials with PDF is a complex task. Even when the radiation fluence is sufficient to produce uniform overlap of the ion tracks, the system remains intrinsically heterogeneous: atoms from different regions of the sample are not expected to be well-aligned and will cease to form sequences of defined atomic coordination spheres. The immediate consequence is that the peaks in the atomic PDF experience a severe broadening with the effect of rendering the function featureless beyond the characteristic "glass-like" correlation length inherent to amorphous materials. Here, this effect is exacerbated by regions of remnant crystallinity that yield a sample with two phases: the amorphous regions that contribute signal to the PDF only at low-*r* and the crystalline regions that contribute signal to the PDF across all *r*-space. Therefore, from an analytical point of view, it is worth distinguishing the neutron PDFs into two regions: shorter-range (1.5 - 5 Å) and longer-range length scales (5 – 25 Å). The shorter-range scale contains

interatomic correlations up to the third neighbor, and it is particularly sensitive to the internal structure of the four polyhedral units and their arrangement, which constitute the elementary building block of the structure. The longer-range scale is more sensitive to the regularity of the stacking of these building blocks (tilt systems, deformations, etc.) and to the regions of the materials that still exhibit long-range order.

The very low-*r* region of the pair distribution function for crystalline weberite-type oxides (black curves in **Figure 6.11 d-f**) can be characterized by three distinct features: (*i*) the first peak ~ 2-0 Å arising from the Ta-O bonds, (*ii*) the second peak between ~2.2-2.4 Å arising from bonds between O and the A-cation, and (*iii*) the third peak around 2.7 Å arising from the nearest neighbor oxygen-oxygen distances. The relative intensity of these three peaks varies from sample to sample due to the change in the neutron scattering length of the A-site cation (4.6 femtometers for Pr, 7.4 for Tb, and 12.4 for Yb). A direct comparison of the PDFs of the samples before irradiation with the PDFs of the irradiated samples (red curves in **Figure 6.11 d-f**) reveals very little change in these three features. There is no evidence of new peaks forming in the PDFs of the three compounds after irradiation and very little modification to the positions and areas of the existing peaks, qualitatively indicating that the integrity of the four weberite-type polyhedra, and thus the basic weberite-type structural building block, is maintained in the irradiated samples. In the case of Pr_3TaO_7, peak areas and positions are maintained, but the peak intensities decrease and broaden more than for the other two samples, suggesting a more pronounced internal distortion of the polyhedra.

To contextualize this response of the three weberite-type oxides, their PDFs were compared with the PDFs of weberite $Sr_2Sb_2O_7$, pyrochlore $Ho_2Ti_2O_7$, and fluorite $Ho_2Zr_2O_7$ (**Figure 6.11 g-l**) irradiated under identical conditions. With respect to the three weberite-type oxides, analysis of

pair correlations at higher values of *r* indicates that the $A_2B_2O_7$ pyrochlore and weberite structures are less crystalline (*i.e.* little remnant peak areas from pair correlations). Interestingly, the very local structure of $Ho_2Ti_2O_7$ pyrochlore after irradiation is very different from prior to radiation, indicating a pronounced rearrangement of the atomic configuration within the amorphous phase. Previous work on compositionally- and topologically-related compounds [16]–[18], [126], [127] has indicated that this new distribution of pair correlations is actually similar to the A_3BO_7 weberite-type structure; this relation can be observed by comparing the PDF of irradiated $Ho_2Ti_2O_7$ (**Figure 6.11 k**) with the weberite-types (**Figure 6.11 d-f**) with the only difference arising from the negative dip corresponding to the Ti-O octahedra (caused by the negative neutron scattering length of Ti nuclei) replacing the peaks corresponding to the Ta-O octahedra.

The response of the $Sr_2Sb_2O_7$ weberite appears to be intermediate to that of the extreme cases of the weberite-types (retention of existing structural building blocks) and the pyrochlore (creation of new structural building blocks). The peaks corresponding to the Sb-O octahedra (~ 2Å) are largely maintained while the two peaks corresponding to the Sr-O and O-O distances merge and are severely broadened. Finally, for the samples that have a disordered fluorite structure before irradiation ($Ho_2Zr_2O_7$), the PDFs (**Figure 6.11 l**) are quite similar before and after radiation exposure. Interestingly, this for disordered fluorites such as $Ho_2Zr_2O_7$, it has been shown that the local structure is almost indistinguishable from the weberite-type configuration [14], [15], [17]; thus, swift heavy ion irradiation does not modify the structure of this compound over any material length scale. In summary, the compounds that exhibit weberite-type local structures prior to irradiation (A_3TaO_7, $Ho_2Zr_2O_7$) exhibit superior tolerance across the sub-nanoscale to structural modification by swift heavy ion exposure.

To further evaluate the response of the weberite-type compounds to swift heavy ions, small-box refinements were performed on the three weberite-type irradiated samples (**Figure 6.12**). In contrast to the more qualitative analysis above, small-box modeling provides a pathway for enforcing the rules of particular symmetries during PDF analysis (analogous to the Rietveld refinement of diffraction data). However, this task cannot be easily performed on the PDFs of irradiated samples using a single-phase model because there is no proper way to accurately describe the heterogeneous loss of coherence across the data range created by the track topology and their overlap. This spatial heterogeneity implies the operational need to distinguish and separate two ranges ($r < 5$Å and $r > 5$Å), where the effects of the correlation loss do not bear the same consequences. To achieve this, a model with two distinct components was developed: the first component has a glassy flavor, with spatial contributions not exceeding second- or third-neighbor distances. The second phase has a standard crystalline flavor: it describes pair correlations in both ranges, carrying information about both the polyhedra and their stacking within and above the unit cell. The results of these small-box refinements of PDF data of all three compounds are shown in **Figure 6.12**. These two-phase models reproduce the experimental PDF for the three irradiated compounds over the entire $r < 25$ Å data range. The longer-range correlations are consistent with the structural model of the weberite-type prior to irradiation. However, the fact that short-range correlations in each irradiated sample can be modeled using the same crystalline structure corroborates what can be seen visually in **Figure 6.11**: the weberite-type structural building blocks are largely left unperturbed by radiation, only their longer-range organization is affected.

In many fluorite-derived complex oxides, some cation species form networks of connected octahedra. This is true for all complex oxides considered in this study. In weberite-type structures,

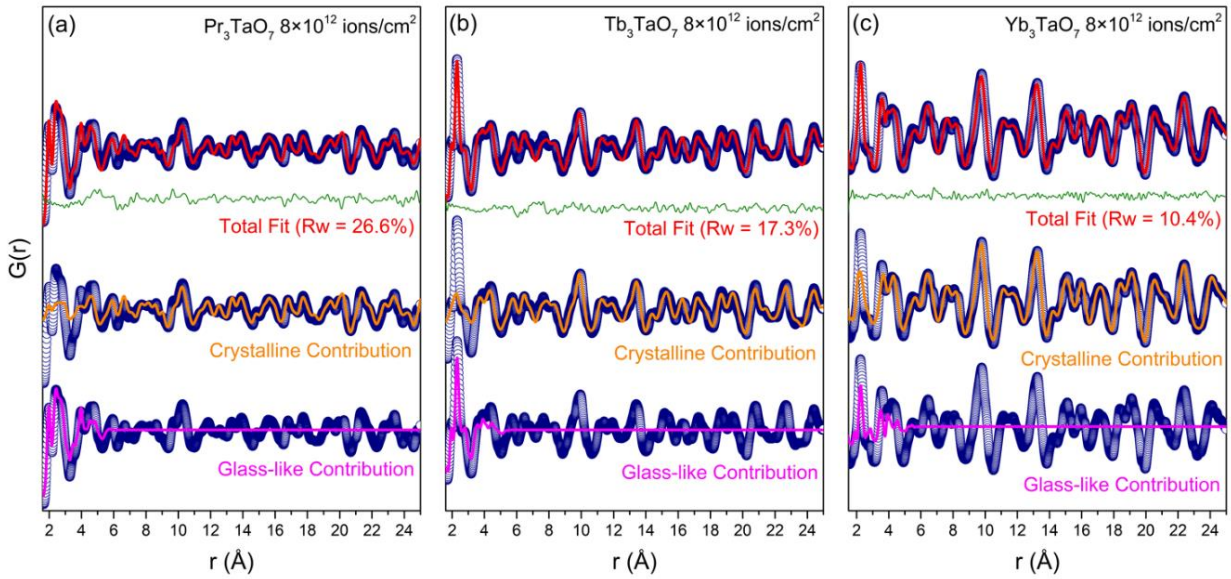

Figure 6.12: Small-box refinements of neutron PDFs for weberite-type oxides irradiated with 1.47 GeV Au ions, shown for (*a*) Pr_3TaO_7, (*b*) Tb_3TaO_7, and (*c*) Yb_3TaO_7. The analysis employs a 2-phase approach consisting of a crystalline weberite-type model and a separate short-range glass-like weberite-type model. The blue open circles represent the experimental neutron PDF, the red line represents the total fit to the data using both models, and the orange and magenta lines represent the individual contributions of the 2-phase approach. The solid green line represents the difference between the model and the fit.

the $B^{5+}O_6$ octahedra form one-dimensional octahedral 'chains' along [001]. This particular octahedral network in weberite-types permits a larger radius of A ions or, for smaller A ions, an increased displacive disorder. The tilt of these octahedral chains allows the possibility of an almost continuous adjustment of displacive disorder. This directly translates in many local configurations and in the presence of a large ground-state manifold, which may enhance the resistance to short-wavelength fluctuations of atomic displacements. Usually, stability is associated to periodicity and rigid rules. Instead, analysis of weberite-type oxides suggests that the most flexible displacement configurations, typical of the compounds lacking long-range order, are the least affected by the presence of short-range fluctuations and, therefore, outperform their more rigid counterparts under continuous radiation exposure.

This concept is illustrated in **Figure 6.13**, which compares the three-dimensional cation networks of weberite types (described above) with those of weberite (**Figure 6.13 b**), pyrochlore (**Figure 6.13 c**), and disordered fluorite (**Figure 6.13 d**). In weberite-type structures (**Figure 6.13 a**), there are layers composed of BO_6/AO_8 chains that stack along [100] alternating with layers made up of AO_7 polyhedra. In contrast to the one-dimensional octahedral chains' characteristic of weberite-types, the octahedral networks of the weberite oxides $A_2B_2O_7$ pyrochlore ($Ti^{4+}O_6$) and $A_2B_2O_7$ ($Sb^{5+}O_6$) weberite oxides are three-dimensional and all layers that stack along [100] consist of BO_6 and AO_8 polyhedra. Therefore, when considering the most rigid units (octahedra containing high-valence cations) in the three structures, the independence and one-dimensionality of the BO_6 octahedra in weberite-types provide a degree of displacive flexibility not available in the structures with three-dimensional octahedral networks. Under irradiation, the one-dimensional chains can tilt independently of each other, with knock-on consequences manifesting only in the flexible nearest-neighbor AO_7 layers. On the contrary, under irradiation, the distortions of the

(a) Weberite-type Pr_3TaO_7 **(b)** Weberite $Sr_2Sb_2O_7$

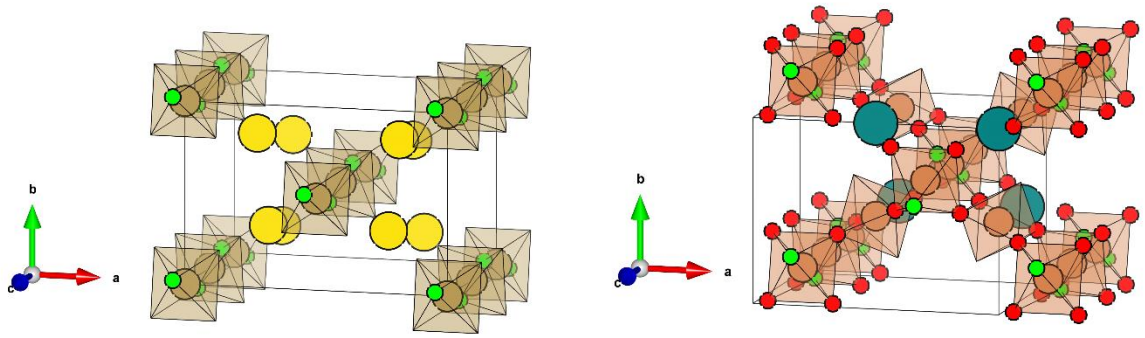

(c) Pyrochlore $Ho_2Ti_2O_7$ **(d)** Defect-fluorite $Ho_2Zr_2O_7$

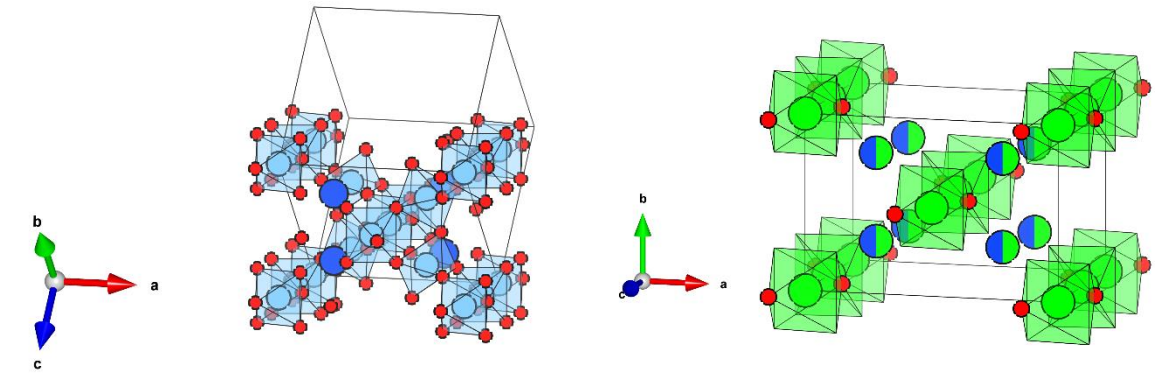

Figure 6.13: Structures and cation network of pristine (*a*) Pr_3TaO_7 *Cmcm* weberite-type oxides, (*b*) $Sr_2Sb_2O_7$ *Imma* weberite, (*c*) $Ho_2Ti_2O_7$ *Fd-3m* pyrochlore and (*d*) $Ho_2Zr_2O_7$ defect-fluorite with *Ccmm* local structure. In (*a*), brown spheres are Ta^{5+} cations, while yellow spheres are Pr^{3+} cations in PrO_7 polyhedra. Pr cations forming chains along [001] are not shown. Oxygen atomic sites participating in connectivity of TaO_6 polyhedra chains are shown as green spheres. In (*b*), brick orange spheres represent Sb^{5+} cations, while cyan spheres represent Sr^{2+} cations in SrO_8 polyhedra. Sr cations forming chains along [001] are not shown. Oxygen atomic sites participating in connectivity of SbO_6 cation network are shown as red and green spheres. In (*c*), light blue spheres are Ti^{4+} cations, while dark blue spheres are Ho^{3+} cations in HoO_6 polyhedra. Ho cations forming chains along [011] are not shown. Oxygen atomic sites participating in connectivity of TaO_6 polyhedra chains are shown as green spheres. In (*d*), green spheres are Zr^{4+} cations, while dark blue spheres are Ho^{3+} cations. Mixed green/ blue sphere represents mixed $(Zr_{0.5}Ho_{0.5})O_7$ polyhedra. Ho cations forming chains along [001] are not shown. Oxygen atomic sites participating in the connectivity of ZrO_6 polyhedra chains are shown as red spheres. In all figures, solid black lines are respective unit cells.

octahedra in the pyrochlore $A_2B_2O_7$ will have knock-on effects that propagate throughout the entire three-dimensional octahedral network, necessitating a fundamental reorganization of the structure, peculiarly into a weberite-type configuration [126]. Finally, the defect-fluorite $Ho_2Zr_2O_7$ exhibits a local weberite-type structure prior to irradiation [15], [17] which also has one-dimensional octahedral chains, but also has the most flexible interlayer arrangement since it possesses (A^{3+}, B^{4+})O_7 planes that have a random distribution of A^{3+} and B^{4+} cations, in this case Ho and Zr. Under irradiation, the combination of the one-dimensional octahedral chains along with the most flexible seven-coordinated interlayer yields no discernible modification to either the long- or short-range structures.

These considerations provide a theoretical framework for understanding the local stability of weberite-type local configurations. The ground state manifold available in the weberite-type structures can play the role of a structural attractor for other structure types, like ordered $A_2B_2O_7$ pyrochlores, that allow only minor departures from more rigid rules. This same mechanism is also observed in solid solutions of pyrochlore structures (such as in $Ho_2Ti_{2-x}Zr_xO_7$ [15]) where flexible local weberite-type arrangements successfully compete with the long-range rigid pyrochlore order under the introduction of compositional disorder. Cation antisite defects in A_3BO_7 weberite-type oxides are greatly suppressed due to stoichiometry and valence considerations; the displacive component remains the most viable option for the system to compensate for irradiation-induced structural modifications. Therefore, the ability of specific weberite-type oxides to displacively disorder may play a major role in determining the ultimate radiation response. To test this correlation, we considered (**Figure 6.14**) the level of preexisting distortion of BO_6 octahedra of weberite-type oxides (extracted from PDF analysis) along with the amorphous cross sections of weberite-type oxides (extracted from deconvolution of XRD patterns of weberite-types irradiated

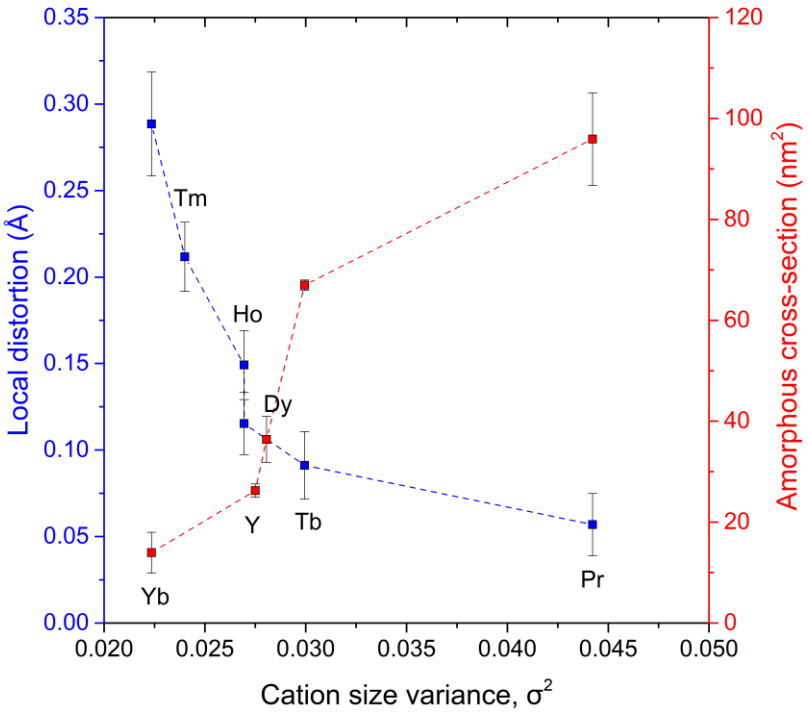

Figure 6.14: Quantified local distortion parameter for the pristine A_3BO_7 (blue datapoints, data reproduced from [45]) overlayed against the amorphous cross-section for irradiated compounds (red datapoints). Colored lines serve as guides for the eyes.

with 946 MeV Au ions). This suggests that Yb_3TaO_7 composition with the largest pre-existing local distortions, indicating an ability to accommodate displacive disorder, displays the smallest amorphous cross-section. The opposite is true for compositions with the smallest pre-existing local distortion. Within the A_3TaO_7 weberite-type oxide system, the displacive component must play a crucial role in improving radiation resistance in the chemical series. Therefore, the statement made by Uberuaga *et al.* [7] "…amorphization resistance inversely correlates with the ability of the oxide to disorder," is also true for the weberite-type oxides, but it is not due the ability of the compound to *compositionally* disorder, but instead, *displacively* disorder. Further, we show here that the variance in cation sizes, while inversely correlated with the propensity to *compositionally* disorder, is also inversely correlated with the propensity to *displacively* disorder, making it a predictor for the resilience of short-range atomic building blocks.

6.4 Conclusion

The response of weberite-type oxides to swift heavy ion irradiation, studied here for the first time, is complex and heterogeneous across the different length scales. Systematic irradiation with 946 MeV Au across a range of ion fluences reveals that weberite-type compounds are amorphizable; the development of the amorphous phase correlates directly with the variance in cation sizes. This development is consistent with other $A_2B_2O_7$ oxides irradiated under identical conditions. However, this relation for weberite-type oxides cannot be wholly attributable to cation antisite defects, as it can be in pyrochlore oxides. In contrast to their long-range structural response, the short-range structures of weberite-type oxides irradiated with 1.46 GeV Au ions still exhibit the characteristic polyhedra and stacking of their pristine counterparts. This is also in contrast to the behavior of $A_2B_2O_7$ pyrochlore, which, while also amorphizable, additionally undergoes a local

reorganization to a weberite-type configuration. The short-range organization of weberite-type oxides is shown to be highly flexible and accommodating of displacive disorder. The propensity to accommodate displacive disorder among the different weberite-type compounds appears to explain the variance in their resistance to amorphization. This effect can be considered alongside previous work that correlated the propensity for accommodating compositional disorder with the resistance to amorphization in pyrochlore oxides. These findings shed light on the structural response of weberite-type oxides to ionizing radiation, advancing our understanding of fundamental ion-matter interactions across various spatial length scales within the family of fluorite-derived materials.

6.5 Supplemental materials

6.5.1 *Diffuse scattering analysis in Q-space*

As previously stated in sections 6.3.1 and 6.3.2, two separate contributions (crystalline and amorphous) can be identified within ion-irradiated weberite-type oxides' diffraction (Q-space) data. This allows for a significant simplification of defining the microdomain correlations that must be described when setting up Neder's model [84]. The results of the Rietveld refinements, using Neder's microdomain approach to handle simultaneously the long-range and medium-range correlations, are shown in **Figure 6.15**. The long-range correlations in the irradiated samples can be modeled using the corresponding pristine long-range structural models (*Cmcm* for Pr_3TaO_7, *Ccmm* for Tb_3TaO_7, and *Fm-3m* for Yb_3TaO_7 respectively) [45]. The medium-range correlations are embodied by a correlated difference phase between the proper long-range higher symmetry pristine model and an average fluorite structure, consisting of cations and O vacancies randomly distributed onto their respective cation and anion real-space sublattice sites. The Rietveld

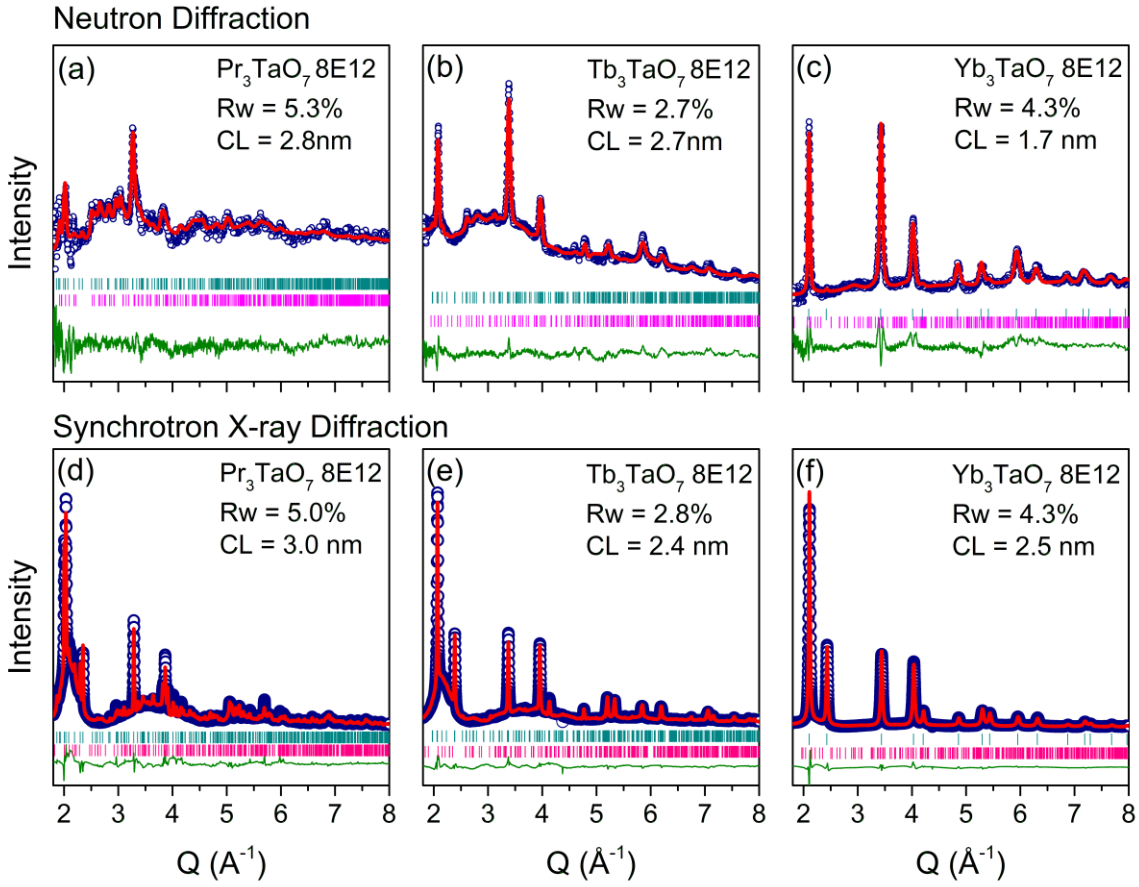

Figure 6.15: Rietveld refinement contributions to neutron (*a-c*) and SXRD (*d-f*) diffraction signal (NOMAD detector bank 3) of (*a*, *d*) Pr_3TaO_7, (*b*, *e*) Tb_3TaO_7, and (*c*, *f*) Yb_3TaO_7 after ion irradiation with 1.47 GeV Au ions to a fluence of 8×10^{12} ions/cm^2. The hollow blue circles represent the experimental data, the red lines represent the total fits of the diffraction data (using Neder's microdomain diffraction approach). The green lines represent the differences between the data and the model, while cyan and magenta ticks are expected diffraction maxima of the crystalline and diffuse contributions.

refinement of the diffraction patterns of these three irradiated samples yields good fit qualities, with low *Rw* reliability factors of 5.013, 2.754, and 4.271%, respectively. The estimated correlation lengths for the medium-range order produced by the irradiation are within a somewhat narrow interval: 3.0(2) nm (Pr_3TaO_7), 2.4(3) nm (Tb_3TaO_7) and 1.7(5) nm (Yb_3TaO_7).

The same kind of analysis can be repeated using neutron scattering data. The exercise has some advantages because the coherent bound scattering lengths for neutron scattering have different behaviors. In contrast to X-ray atomic form factors, which increase monotonically with the atomic number and decrease with increasing Q, the coherent bound scattering lengths are constant and not a simple function of the atomic number, resulting in different contrasts between the elements and, in the current case of compositional correlations, the diffuse scattering is no longer going to be a decreasing function with increasing Q. Ta's bound coherent scattering length is 6.91 fm, while it is 4.58 fm for Pr, 7.38 fm for Tb, and 12.43 for Yb. Also, the coherent bound scattering length of O is 5.803, implying that the cation sublattice no longer dominates the scattering signal. The most prominent cation contrast using neutron scattering is in Yb_3TaO_7, which was the weakest in X-ray experiments; it is followed by Pr_3TaO_7, while Tb_3TaO_7 has the smallest cation contrast. This compound is an interesting case as it allows to study correlations originating mainly from the oxygen sublattice.

A diffuse scattering contribution exists in pristine Yb_3TaO_7, (a long-range disordered defect fluorite system, **Figure 6.16**): the medium-range order in this system is characterized by a correlation length of about 5.8(1) nm. In agreement with the results published on the pristine phases, Pr_3TaO_7 and Tb_3TaO_7 do not exhibit any significant diffuse scattering contributions, and therefore these systems are just characterized by a long-range correlation length that equates or exceeds the coherence volume of the impinging beam. After irradiation, the three compounds

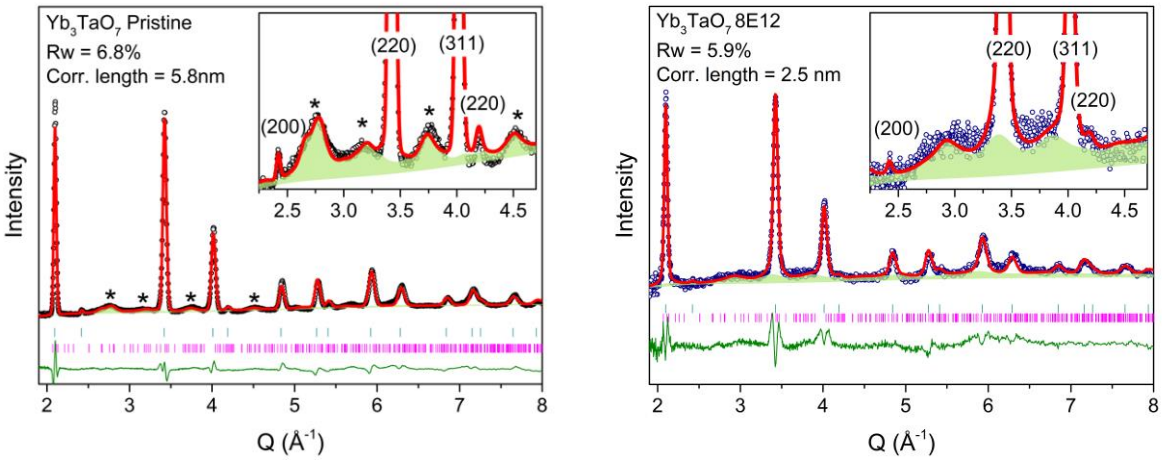

Figure 6.16: The long-range and medium-range neutron scattering contributions (NOMAD detector bank 3) of pristine (left) and irradiated (right) Yb_3TaO_7. The hollow black and dark blue circles represent the experimental data, the red lines represent the total fits of the diffraction data (Neder's microdomain approach), and the green-shaded regions represent the diffuse scattering contribution. The dark green line represents the difference between the data and the model, while cyan and magenta ticks are expected diffraction maxima from crystalline and amorphous contributions, respectively. An inset shows a magnified 2.2 - 4.6 $Å^{-1}$ region from the diffraction data. Asterisks indicate the locations of the most intense diffuse scattering features. The *hkl* indices label the diffraction maxima of the long-range *Fm-3m* defect-fluorite structure.

display (**Figure 6.15**) several diffuse scattering contributions, centered around 1.9, 3.6, and 5.5 $Å^{-1}$. **Figure 6.15** (*a*-*c*) summarizes the results of the Rietveld refinements performed according to the same models already used during the analysis of the synchrotron data. The final *Rw* reliability factors are 5.3% (Pr_3TaO_7), 2.7% (Tb_3TaO_7), and 5.9% (Yb_3TaO_7), with similar estimated medium-range correlation lengths of 2.8(2) nm, 2.7(2) nm, and 2.5(2) nm, respectively, that compare favorably with the previous estimates obtained by SXRD. The correlation lengths are summarized in **Figure 6.17** for both SXRD (NSLS-II, APS) and neutron diffraction experiments.

This provides reasonable evidence that ion irradiation, regardless of the initial long-range order, always creates a medium-range response. It also provides irrefutable proof that the irradiation response of these compounds is not a simple antisite mechanism, but an emergent and cooperative one that spans a longer lengthscale. This behavior is not unique to weberite-type oxides and occurs in a few other fluorite-related structures [114], and it is characteristic of dissipative systems that develop patterns, structures, and behaviors that they did not have when first formed.

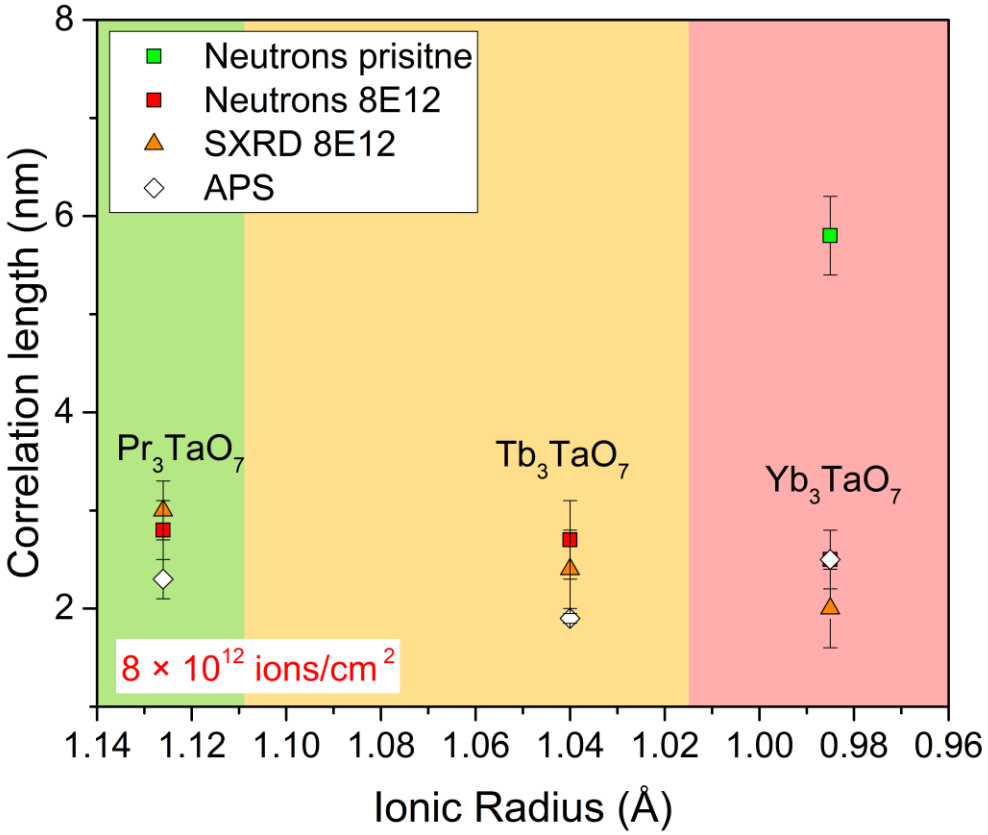

Figure 6.17: The estimated correlation lengths from diffuse scattering for Pr_3TaO_7, Tb_3TaO_7, and Yb_3TaO_7 irradiated compositions, estimated from neutron diffraction (red squares) and synchrotron X-ray diffraction (red triangles and white rhomboids) data. The green square denotes the characteristic correlation length estimated from the neutron diffuse scattering experiment on pristine Yb_3TaO_7. Pristine Pr_3TaO_7 and Tb_3TaO_7 are ordered long-range structures and do not display any detectable diffuse scattering signal. The error bars provide the uncertainties related to the refined values.

Chapter 7: Conclusions

Weberite-type A_3BO_7 (A = trivalent rare earth, B = pentavalent Ta, Nb, Sb, and others) oxides have recently attracted increased attention after the weberite-type local atomic arrangement was discovered in out-of-equilibrium weberite-type and pyrochlore ceramics possessing a long-range defect-fluorite structure. Being an extreme stochiometric variant of $A_2B_2O_7$ weberite structure and being able to accommodate a large variety of cations, weberite-type oxides are of interest, with most studies being focused on characterizing long-range structures by diffraction experiments; thus, little was known prior to this thesis on the short-range atomic behavior in ordered and disordered weberite-type compounds. This thesis has expanded on previous work and represents the first comprehensive structural investigations on a wide range of weberite-type tantalates across all structural correlation lengths.

The long-range structure of medium-sized A_3TaO_7 rare earth tantalate oxides was debated in the literature, and whether their structures are defined by centrosymmetric or noncentrosymmetric spacegroups. The first study of this thesis [46], shown in Chapter 4, was a starting point to solve the existing discrepancy and develop the required analytical tools to precisely characterize the local atomic configuration and long-range structure. It was shown that Y_3TaO_7, a composition that has been previously used to define the structural "family" of medium-sized weberite-type oxides, is rather an outlier, with a structure that is distinct from other medium-sized Ln_3TaO_7 oxides, most likely due to the absence of f-shell electrons in Y. Detailed neutron total scattering coupled with DFT calculations showed that the structure of Y_3TaO_7 is best represented by the $C222_1$ spacegroup for both local- and long-range structures. This means that the structure of this compound is *invariant* across all structural correlation lengths.

Approximately ten years ago, neutron total scattering was first used to reveal that a disordered A_3BO_7 weberite-type oxide with defect-fluorite long-range structure is not isomorphous with the local structural organization; King *et al.* [20] showed that the local structure of disordered defect-fluorite Yb_3TaO_7 differs from the long-range structure and that the local structure possesses a high degree of local order and resembles the orthorhombic lattice configuration with a specific placement of cations and oxygen sites, resulting in polyhedra configurations that are similar to the ones observed in the ordered polymorphs: AO_8, AO_7, and BO_6. Later, Shamblin *et al.* [17] demonstrated that this specific local configuration can be adapted to successfully describe the disordered $A_2B_2O_7$ pyrochlore oxides with a long-range defect-fluorite structure, thus possessing a similar structural heterogeneity. O'Quinn *et al*. [14] formulated the necessity of such constrained, ordered local atomic arrangements in disordered pyrochlore and spinel oxides by extending the fundamental chemical rules for ordered ionic compounds previously formulated by Pauling [128]. The original study of the local structure of defect-fluorite weberite-type oxides was limited to only one chemical composition, namely Yb_3TaO_7 [20]; however, it set the stage for further systematic studies.

The second study included of this dissertation, shown in Chapter 5, [45] greatly expands these efforts and presents a detailed systematic structural study on the chemical series of Ln_3TaO_7 weberite-type oxides covering all three structural families (Pr, Dy, Tb, Ho, Tm, and Yb). Coupled neutron- and X-ray total scattering experiments revealed that: (*i*) the appropriate structural models for the short-range structures are best described by noncentrosymmetric space groups: *C2cm* (family 1), *C222$_1$* (family 2) and *C2mm* (family 3); (*ii*) these ground states configurations accurately capture all atomic relaxations, tilts, and distortions; (*iii*) the corresponding long-range structures, namely *Cmcm* (family 1), *Ccmm* (family 2), *Fm-3m* (family 3) are results of

configurational averaging of local crystallographic domains with distinct translations and orientations; (*iv*) all compounds display various degree of local distortions that increase monotonically across the chemical series, eventually producing the complete long-range disordering of the system. This systematic study [45] shows that weberite-type tantalates are much more complex than previously thought and establishes the relations between short- and long-range order. All of the distortions of local organization increase monotonically with the decreasing ionic radius of Ln cation and are correlated with an increased local dipolar polarization of TaO_6 octahedron: the initial loss of inversion center, promoting the noncentrosymmetric local organization, leads to specific distortions of the characteristic polyhedra. When the critical quantity of local distortions is too large, the system experiences frustration, triggering the long-range structural transformation. This occurs as a change of tilt system at the boundary between family 1 and 2, and as an ensemble domain average to a defect-fluorite structure when crossing the frontier between family 2 and 3. This new picture of progressing short-range distortions and competition with long-range organizations is a step forward from the simple previous picture of weberite-type complex oxides as three distinct long-range structures.

The analyses described above are impossible without an experimental framework with a specific aim to precisely model and discriminate among different local configurations. This was achieved by using (*i*) a total scattering experiment in which effects of thermal vibrations are reduced to yield a *localized* atomic configuration, (*ii*) an approach to rationalize and explore candidates for various local symmetries, and (*iii*) a method to efficiently discriminate among different structural models. As an initial step, all measurements were performed at 100K in a low-background sample container to reduce thermal smearing and accurately access displacive components of the structures. Then, compatibility relations from group theory were employed to

define a prototype structure and derive daughter structures based on phonon mode analysis of the dynamic structure, which helped to produce local structural models for each compound. As a final step, a new correlated reliability factor calculation approach (*Gs*) was introduced to test the proposed structures against the as-collected data and to identify correlated regions within the PDF data characteristic of systematic inaccuracies of the small box models. The best candidate structures and corresponding fit qualities were also compared against the conventional reliability factor (*Rw*) calculation approach to determine the statistically appropriate local organization and spacegroup definition.

While the structural information presented in this thesis is of interest from a fundamental science point of view, the acquired structural knowledge may assist in better understanding of related physical properties in these materials. Many weberite-type compounds have interesting magnetic, photocatalytic, optical, and thermomechanical properties, and future studies should focus on how these properties are linked with the atomic-scale order that could be tuned eventually to achieve improved properties. For example, the occurrence of a second harmonic generation reported in the literature for Gd_3NbO_7 [40] can only be understood when displacements away from the ideal B^{5+} (Ta, Nb) octahedron site are considered, as second harmonic generation is allowed only in a noncentrosymmetric system.

Following the structural knowledge obtained with this thesis's first two publications, weberite-type tantalates' response to swift heavy ions was tested and presented in Chapter 6. Weberite-type materials have never been studied under any type of radiation prior to this work, in sharp contrast to the well-studied pyrochlore oxides. This thesis addresses this knowledge gap and produces a set of irradiation data of weberite-type tantalates, evaluates their general radiation resistance, and correlates compositional changes to induced amorphization.

Two approaches were used: (*i*) a systematic study on a wide range of compounds with changes in both A- and B-site cations using 950 MeV Au ions and high-throughput synchrotron XRD analysis and (*ii*) a short-range neutron PDF analysis coupled with neutron and high-resolution X-ray diffraction on a few selected compounds irradiated using 1640 MeV Au ions. While in (*i*) the relative amorphization resistance and determination of amorphous cross section was the primary deliverable, the (*ii*) provided detailed insight into the atomic scale changes induced by swift heavy ions. In both approaches, the results were compared with $A_2B_2O_7$ pyrochlore and weberite oxides.

A systematic irradiation study reveals that the long-range structure of weberite-type oxides behaves similarly to the pyrochlore oxides. All the weberite-type tantalates, niobates, and antimonates tested become amorphous, but the resistance to amorphization increases with decreasing cation size variance among the A- and B-site cations, same behavior previously reported for pyrochlore oxides [4] that is in term associated with an increasing level of local distortions. The amorphization cross section follows a consistent trend: amorphous cross-sectional area per ion track increases with increasing cation variance. Due to their three distinct polyhedra, a much broader range of cations can be fit in weberite-type oxides than in pyrochlore oxides, eventually enabling to synthesize compounds that are overall more amorphization resistant; however, no weberite-type compounds tested (and in particular those displaying a long-range defect fluorite structure) outdistance the unique radiation resistance of defect-fluorite $Ho_2Zr_2O_7$, only material that does not amorphize at measured fluences.

An in-depth neutron total scattering study on selected irradiated weberite-type oxides revealed minimal changes within the local atomic configuration across all three structural families. The observed short-range atomic arrangement after irradiation is similar to that observed in pristine

systems. This is in stark contrast to pyrochlore oxides that undergo a local structural transformation after ion irradiation from pyrochlore to weberite-type (cubic-to-orthorhombic). Thus, this study highlights an important point: the commonly used binary long-range description of amorphization does not provide a totally accurate metric for the complex changes occurring within the short-range order. While certain $A_2B_2O_7$ pyrochlore compounds might appear to be more resistant than some weberite-type compounds when monitoring long-range behavior (indicated by smaller amorphous fraction at the same ion fluence), the short-range organization of weberites displays a lesser change. The latter is true for an $A_2B_2O_7$ weberite compound: while it is the least radiation-resistant compound of all tested in the study, owing to its largest cation variance parameter, its local order shows no major changes and rearrangements.

The swift heavy ion irradiation studies on weberite-type oxides performed in this thesis, are the first of their kind and should be expanded to other ion-beam conditions (including the regime of nuclear energy losses). Besides XRD and neutron total scattering, high-resolution TEM imaging should be included in future studies to clarify whether ion tracks in weberite-type materials have the core-shell morphology observed in many pyrochlores. This thesis showed that radiation resistance is complex and even in compounds that have fully lost their crystallinity, local atomic configurations possess a high degree of order. It may be concluded that the stacking or medium-range arrangements of local building blocks plays a key role in the amorphization process. The future work should incorporate reverse Monte Carlo (RMC) coupled with molecular dynamics (MD) modeling to address short- and medium-range organization lengths of amorphous compounds, similarly to a framework designed for waste glass materials and shown the appendix of the thesis.

The knowledge and methodology accumulated in this thesis can be extended to other complex oxides, addressing specific effects at different correlation lengths (short-, medium-, and long-range) that are still not well understood: this can be applied to other RE_3BO_7 weberite-type oxides (B = Nb, Sb, Re, Os, and others) and more broadly to other fluorite-related oxides, such as $A_2B_2O_7$ weberites, pyrochlores, etc. The methods developed in this thesis (PDF measurement technique performed at low temperature, *Gs* correlated-error analysis, and phonon mode analysis) are generic and can be easily implemented in other research fields, and they can be useful to set up constraints for Reverse Monte Carlo (RMC) modeling.

References:

[1] S. J. Zinkle and G. S. Was, "Materials challenges in nuclear energy," *Acta Mater.*, vol. 61, no. 3, pp. 735–758, 2013, doi: 10.1016/j.actamat.2012.11.004.

[2] S. J. Zinkle and L. L. Snead, "Designing radiation resistance in materials for fusion energy," *Annu. Rev. Mater. Res.*, vol. 44, pp. 241–267, 2014, doi: 10.1146/annurev-matsci-070813-113627.

[3] T. Allen, J. Busby, M. Meyer, and D. Petti, "Materials challenges for nuclear systems," *Mater. Today*, vol. 13, no. 12, pp. 14–23, 2010, doi: 10.1016/S1369-7021(10)70220-0.

[4] K. E. Sickafus *et al.*, "Radiation tolerance of complex oxides," *Science (80-.).*, vol. 289, no. 5480, pp. 748–751, 2000, doi: 10.1126/science.289.5480.748.

[5] M. Wakeshima, H. Nishimine, and Y. Hinatsu, "Crystal structures and magnetic properties of rare earth tantalates RE 3TaO7 (Re = rare earths)," *J. Phys. Condens. Matter*, vol. 16, no. 23, pp. 4103–4120, 2004, doi: 10.1088/0953-8984/16/23/025.

[6] F. P. Marlton, Z. Zhang, Y. Zhang, T. E. Proffen, C. D. Ling, and B. J. Kennedy, "Lattice Disorder and Oxygen Migration Pathways in Pyrochlore and Defect-Fluorite Oxides," *Chem. Mater.*, vol. 33, no. 4, pp. 1407–1415, 2021, doi: 10.1021/acs.chemmater.0c04515.

[7] B. P. Uberuaga *et al.*, "Opposite correlations between cation disordering and amorphization resistance in spinels versus pyrochlores," *Nat. Commun.*, vol. 6, 2015, doi: 10.1038/ncomms9750.

[8] T. Linda Francis, P. Prabhakar Rao, S. K. Mahesh, T. S. Sreena, and S. Parvathi Babu, "Effect of host structure on the photoluminescence properties of Ln3TaO7:Eu3+ red phosphors," *Opt. Mater. (Amst).*, vol. 52, pp. 134–143, 2016, doi: 10.1016/j.optmat.2015.12.028.

[9] L. Cai and J. C. Nino, "Complex ceramic structures. I. Weberites," *Acta Crystallogr. Sect. B Struct. Sci.*, vol. 65, no. 3, pp. 269–290, 2009, doi: 10.1107/S0108768109011355.

[10] M. Lang, F. X. Zhang, R. C. Ewing, J. Lian, C. Trautmann, and Z. Wang, "Structural

modifications of Gd 2Zr 2-xTi xO 7 pyrochlore induced by swift heavy ions: Disordering and amorphization," *J. Mater. Res.*, vol. 24, no. 4, pp. 1322–1334, 2009, doi: 10.1557/jmr.2009.0151.

[11] M. Lang *et al.*, "Single-ion tracks in Gd2Zr(2−x)Ti(x)O7 pyrochlores irradiated with swift heavy ions," *Phys. Rev. B*, vol. 79, no. 22, p. 224105, 2009, doi: 10.1103/PhysRevB.79.224105.

[12] K. E. Sickafus *et al.*, "Radiation-induced amorphization resistance and radiation tolerance in structurally related oxides," *Nat. Mater.*, vol. 6, no. 3, pp. 217–223, 2007, doi: 10.1038/nmat1842.

[13] E. C. O'Quinn *et al.*, "Multi-scale investigation of heterogeneous swift heavy ion tracks in stannate pyrochlore," *J. Mater. Chem. A*, vol. 9, no. 31, pp. 16982–16997, 2021, doi: 10.1039/d1ta04924k.

[14] E. C. O'Quinn *et al.*, "Predicting short-range order and correlated phenomena in disordered crystalline materials," *Sci. Adv.*, vol. 6, no. 35, 2020, doi: 10.1126/sciadv.abc2758.

[15] D. L. Drey *et al.*, "Disorder in Ho2Ti2−xZrxO7: pyrochlore to defect fluorite solid solution series," *RSC Adv.*, vol. 10, no. 57, pp. 34632–34650, 2020, doi: 10.1039/d0ra07118h.

[16] R. Sherrod, E. C. O. Quinn, J. Neuefeind, I. Gussev, and M. Lang, "Comparison of Short-Range Order in Irradiated Dysprosium Titanates," *npj Mater. Degrad.*, pp. 1–7, 2021, doi: 10.1038/s41529-021-00165-6.

[17] J. Shamblin *et al.*, "Probing disorder in isometric pyrochlore and related complex oxides," *Nat. Mater.*, vol. 15, no. 5, pp. 507–511, 2016, doi: 10.1038/nmat4581.

[18] J. Shamblin *et al.*, "Similar local order in disordered fluorite and aperiodic pyrochlore structures," *Acta Mater.*, vol. 144, pp. 60–67, 2018, doi: 10.1016/j.actamat.2017.10.044.

[19] J. Shamblin *et al.*, "Structural response of titanate pyrochlores to swift heavy ion irradiation," *Acta Mater.*, vol. 117, pp. 207–215, 2016, doi: 10.1016/j.actamat.2016.07.017.

[20] G. King, C. M. Thompson, J. E. Greedan, and A. Llobet, "Local structure of the vacancy disordered fluorite Yb3TaO 7 from neutron total scattering," *J. Mater. Chem. A*, vol. 1, no.

35, pp. 10487–10494, 2013, doi: 10.1039/c3ta12100c.

[21] A. Byström, “X-Ray analysis of Ca 2 Sb 2 O 7 and compounds of similar composition,” *Ark. för Kemi, Mineral. O. Gelogi*, vol. 18, no. 21, pp. 1–8, 1944.

[22] O. Yakubovich, V. Urusuv, W. Massa, and D. Babel, “Structure of Na2Fe2F7, and Structural Relations in the Family of Weberites Na2M"M"’F7,” *Z. anorg. allg. C’hcm*, vol. 619, pp. 1909–191, 1993.

[23] N. Ruchaud, J. G. P. Gravereau, P. Nuiiez, and A. Tressaud, “Copper Weberites : Crystal Structure and Magnetic Investigation of Na , CuGaF , and Na , CuInF ,” vol. 610, pp. 67–74, 1992.

[24] R. Abe, M. Higashi, K. Sayama, Y. Abe, and H. Sugihara, “Photocatalytic activity of R3MO7 and R 2Ti2O7 (R = Y, Gd, La; M = Nb, Ta) for water splitting into H2 and O2,” *J. Phys. Chem. B*, vol. 110, no. 5, pp. 2219–2226, 2006, doi: 10.1021/jp0552933.

[25] Y. Du, Y. Zhang, K. Huang, S. Wang, L. Yuan, and S. Feng, “Hydrothermal synthesis and photoluminescence properties of rare-earth niobate and tantalate nanophosphors,” *Dalt. Trans.*, vol. 42, no. 22, pp. 8041–8048, 2013, doi: 10.1039/c3dt50141h.

[26] N. Preux *et al.*, “La3TaO7 derivatives with Weberite structure type: Possible electrolytes for solid oxide fuel cells and high temperature electrolysers,” *Comptes Rendus Chim.*, vol. 13, no. 11, pp. 1351–1358, 2010, doi: 10.1016/j.crci.2010.07.009.

[27] Y. Hinatsu, Y. Doi, and M. Wakeshima, “Magnetic Studies on Eu3MO7 (M = Nb, Ta, Ir) with Fluorite-related Structure by 151Eu Mössbauer Spectroscopy and Magnetic Susceptibility Measurements,” *J. Solid State Chem.*, vol. 262, no. February, pp. 224–228, 2018, doi: 10.1016/j.jssc.2018.03.024.

[28] M. Wakeshima and Y. Hinatsu, “Magnetic properties and structural transitions of orthorhombic fluorite-related compounds Ln3MO7 (Ln=rare earths, M=transition metals),” *J. Solid State Chem.*, vol. 183, no. 11, pp. 2681–2688, 2010, doi: 10.1016/j.jssc.2010.09.005.

[29] H. Sugihara, Y. Abe, M. Higashi, R. Abe, and K. Sayama, “ Photocatalytic Activity of R 3 MO 7 and R 2 Ti 2 O 7 (R = Y, Gd, La; M = Nb, Ta) for Water Splitting into H 2 and O 2

," *J. Phys. Chem. B*, vol. 110, no. 5, pp. 2219–2226, 2006, doi: 10.1021/jp0552933.

[30] F. H. Borges, F. J. Caixeta, R. R. Pereira, S. R. de Oliveira, and R. R. Gonçalves, "Yttrium tantalate containing high concentrations of Eu3+ as dopant: Synthesis and structural and luminescence features," *J. Lumin.*, vol. 199, no. March, pp. 143–153, 2018, doi: 10.1016/j.jlumin.2018.03.017.

[31] M. Qin *et al.*, "21-Component compositionally complex ceramics: Discovery of ultrahigh-entropy weberite and fergusonite phases and a pyrochlore-weberite transition," *J. Adv. Ceram.*, vol. 11, no. 4, pp. 641–655, 2022, doi: 10.1007/s40145-022-0575-5.

[32] A. J. Wright *et al.*, "Short-range order and origin of the low thermal conductivity in compositionally complex rare-earth niobates and tantalates," *Acta Mater.*, vol. 235, p. 118056, 2022, doi: 10.1016/j.actamat.2022.118056.

[33] F. Brisse, D. J. Stewart, V. Seidl, and O. Knop, "Pyrochlores. VIII. Studies of some 2–5 Pyrochlores and Related Compounds and Minerals," *Can. J. Chem.*, vol. 50, no. 22, pp. 3648–3666, 1972, doi: 10.1139/v72-580.

[34] M. A. Aia, R. W. Mooney, and C. W. W. Hoffman, "An X-Ray Study of Pyrochlore Fluoantimonates of Calcium, Cadmium, and Manganese," *J. Electrochem. Soc.*, vol. 110, no. 10, p. 1048, 1963, doi: 10.1149/1.2425581.

[35] E. ALESHIN and R. ROY, "Crystal Chemistry of Pyrochlore," *J. Am. Ceram. Soc.*, vol. 45, no. 1, pp. 18–25, 1962, doi: 10.1111/j.1151-2916.1962.tb11022.x.

[36] J. G. Allpress and H. J. Rossell, "Fluorite-related phases Ln3MO7, Ln = rare earth, Y, or Sc, M = Nb, Sb, or Ta. I. Crystal chemistry," *J. Solid State Chem.*, vol. 27, no. 1, pp. 105–114, 1979, doi: 10.1016/0022-4596(79)90149-X.

[37] H. J. Rossell, "Fluorite-Related Sb , or Ta II . Structure Phases LnMO7, Ln = Rare Earth , Y or SC , M = Nb , Sb, or Ta," *J. Solid State Chem.*, vol. 122, pp. 115–122, 1979.

[38] H. J. Rossell, "Fluorite-Related Phases Ln_3MO_7 , Ln = Rare Earth , Y , or SC , M = Nb . Sb , or Ta III. Structure of non-stoichiometric Y_3TaO_7 phase," *J. Solid State Chem.*, vol. 27, pp. 287–292, 1979.

[39] W. T. Fu and D. J. W. IJdo, “On the crystal structures of Ln3MO7 (Ln=Nd, Sm, Y and M=Sb, Ta)-Rietveld refinement using X-ray powder diffraction data,” *J. Solid State Chem.*, vol. 182, no. 9, pp. 2451–2455, 2009, doi: 10.1016/j.jssc.2009.06.028.

[40] L. Cai, S. Denev, V. Gopalan, and J. C. Nino, “Phase transition in weberite-type Gd3NbO7,” *J. Am. Ceram. Soc.*, vol. 93, no. 3, pp. 875–880, 2010, doi: 10.1111/j.1551-2916.2009.03494.x.

[41] A. V Astaph’ev, V. P. Sirotinkin, and S. Y. Stephanovich, “Phase transitions in the compounds Ln3NbO7(Ln=Sm-Gd) with fluorite-like structure,” *Kristallografiya*, vol. 30, no. 3, pp. 603–604, 1985.

[42] K. P. F. Siqueira *et al.*, “Synchrotron X-ray diffraction and Raman spectroscopy of Ln 3NbO7 (Ln=La, Pr, Nd, Sm-Lu) ceramics obtained by molten-salt synthesis,” *J. Solid State Chem.*, vol. 209, pp. 63–68, 2014, doi: 10.1016/j.jssc.2013.10.015.

[43] D. Shi *et al.*, “Highly efficient thermal insulation in crystalline weberites RE3NbO7 (RE=La, Nd, Sm, Eu, Gd) with glass-like thermal conductivity,” *Ceram. Int.*, vol. 48, no. 2, pp. 2686–2692, 2021, doi: 10.1016/j.ceramint.2021.10.053.

[44] P. Winiarz *et al.*, “Conductivity, structure, and thermodynamics of Y2Ti2O7-Y3NbO7solid solutions,” *Dalt. Trans.*, vol. 49, no. 31, pp. 10839–10850, 2020, doi: 10.1039/d0dt02156c.

[45] I. M. Gussev *et al.*, “Systematic study of short- and long-range correlations in RE3TaO7 weberite-type compounds by neutron total scattering and X-ray diffraction,” *J. Mater. Chem. A*, pp. 8886–8903, 2023, doi: 10.1039/d3ta01042b.

[46] I. M. Gussev *et al.*, “Local order of orthorhombic weberite-type Y3TaO7 as determined by neutron total scattering and density functional theory calculations☆,” *Acta Mater.*, vol. 196, pp. 704–709, 2020, doi: 10.1016/j.actamat.2020.07.005.

[47] R. I. Palomares *et al.*, “Defect accumulation in swift heavy ion-irradiated CeO 2 and ThO 2,” *J. Mater. Chem. A*, vol. 5, no. 24, pp. 12193–12201, 2017, doi: 10.1039/c7ta02640d.

[48] M. Lang *et al.*, “Swift heavy ion-induced phase transformation in Gd2O3,” *Nucl. Instruments Methods Phys. Res. Sect. B Beam Interact. with Mater. Atoms*, vol. 326, pp. 121–125, 2014, doi: 10.1016/j.nimb.2013.10.073.

[49] J. F. Ziegler, M. D. Ziegler, and J. P. Biersack, “SRIM - The stopping and range of ions in matter (2010),” *Nucl. Instruments Methods Phys. Res. Sect. B Beam Interact. with Mater. Atoms*, vol. 268, no. 11–12, pp. 1818–1823, 2010, doi: 10.1016/j.nimb.2010.02.091.

[50] M. Lang *et al.*, “Characterization of ion-induced radiation effects in nuclear materials using synchrotron x-ray techniques,” *J. Mater. Res.*, vol. 30, no. 9, pp. 1366–1379, 2015, doi: 10.1557/jmr.2015.6.

[51] C. Prescher and V. B. Prakapenka, “DIOPTAS: a program for reduction of two-dimensional X-ray diffraction data and data exploration,” *High Press. Res.*, vol. 35, no. 3, pp. 223–230, Jul. 2015, doi: 10.1080/08957959.2015.1059835.

[52] J. Neuefeind, M. Feygenson, J. Carruth, R. Hoffmann, and K. K. Chipley, “The Nanoscale Ordered Materials Diffractometer NOMAD at the Spallation Neutron Source SNS,” *Nucl. Instruments Methods Phys. Res. Sect. B Beam Interact. with Mater. Atoms*, vol. 287, pp. 68–75, 2012, doi: 10.1016/j.nimb.2012.05.037.

[53] A. Huq *et al.*, “POWGEN: Rebuild of a third-generation powder diffractometer at the Spallation Neutron Source,” *J. Appl. Crystallogr.*, vol. 52, pp. 1189–1201, 2019, doi: 10.1107/S160057671901121X.

[54] J. P. Perdew, K. Burke, and M. Ernzerhof, “Generalized gradient approximation made simple,” *Phys. Rev. Lett.*, vol. 77, no. 18, pp. 3865–3868, 1996, doi: 10.1103/PhysRevLett.77.3865.

[55] G. Kresse and J. Furthmüller, “Efficiency of ab-initio total energy calculations for metals and semiconductors using a plane-wave basis set,” *Comput. Mater. Sci.*, vol. 6, no. 1, pp. 15–50, 1996, doi: 10.1016/0927-0256(96)00008-0.

[56] B. H. Toby, “EXPGUI, a graphical user interface for GSAS,” *J. Appl. Crystallogr.*, vol. 34, no. 2, pp. 210–213, Apr. 2001, doi: 10.1107/S0021889801002242.

[57] B. H. Toby and R. B. Von Dreele, “GSAS-II: The genesis of a modern open-source all purpose crystallography software package,” *J. Appl. Crystallogr.*, vol. 46, no. 2, pp. 544–549, 2013, doi: 10.1107/S0021889813003531.

[58] E. S. Božin *et al.*, “PDFfit2 and PDFgui: computer programs for studying nanostructure in

crystals," *J. Phys. Condens. Matter*, vol. 19, no. 33, p. 335219, 2007, doi: 10.1088/0953-8984/19/33/335219.

[59] K. Momma and F. Izumi, "VESTA 3 for three-dimensional visualization of crystal, volumetric and morphology data," *J. Appl. Crystallogr.*, vol. 44, no. 6, pp. 1272–1276, 2011, doi: 10.1107/S0021889811038970.

[60] J. F. Berar and P. Lelann, "E.S.D.'s and estimated probable error obtained in rietveld refinements with local correlations," *J. Appl. Crystallogr.*, vol. 24, no. pt 1, pp. 1–5, 1991, doi: 10.1107/S0021889890008391.

[61] M. Wojdyr, "Fityk: A general-purpose peak fitting program," *J. Appl. Crystallogr.*, vol. 43, no. 5 PART 1, pp. 1126–1128, 2010, doi: 10.1107/S0021889810030499.

[62] W. J. Weber, "Models and mechanisms of irradiation-induced amorphization in ceramics," *Nucl. Instruments Methods Phys. Res. Sect. B Beam Interact. with Mater. Atoms*, vol. 166, pp. 98–106, 2000, doi: 10.1016/S0168-583X(99)00643-6.

[63] C. L. Tracy *et al.*, "Role of composition, bond covalency, and short-range order in the disordering of stannate pyrochlores by swift heavy ion irradiation," *Phys. Rev. B*, vol. 94, no. 6, pp. 1–11, 2016, doi: 10.1103/PhysRevB.94.064102.

[64] S. J. Zinkle and G. S. Was, "Materials challenges in nuclear energy," *Acta Mater.*, vol. 61, no. 3, pp. 735–758, 2013, doi: 10.1016/j.actamat.2012.11.004.

[65] J. Lian, R. C. Ewing, F. Zhang, M. Lang, F. Lu, and J. Zhang, "Ion-irradiation-induced structural transitions in orthorhombic Ln2TiO5," *Acta Mater.*, vol. 61, no. 11, pp. 4191–4199, 2013, doi: 10.1016/j.actamat.2013.03.045.

[66] J. Lian, L. M. Wang, K. Sun, and R. C. Ewing, "In situ TEM of radiation effects in complex ceramics," *Microsc. Res. Tech.*, vol. 72, no. 3, pp. 165–181, 2009, doi: 10.1002/jemt.20669.

[67] M. Lang *et al.*, "Review of A2B2O7 pyrochlore response to irradiation and pressure," *Nucl. Instruments Methods Phys. Res. Sect. B Beam Interact. with Mater. Atoms*, vol. 268, no. 19, pp. 2951–2959, 2010, doi: 10.1016/j.nimb.2010.05.016.

[68] L. Thomé *et al.*, "Radiation effects in nuclear materials: Role of nuclear and electronic

energy losses and their synergy," *Nucl. Instruments Methods Phys. Res. Sect. B Beam Interact. with Mater. Atoms*, vol. 307, pp. 43–48, 2013, doi: 10.1016/j.nimb.2012.11.077.

[69] E. C. O'Quinn *et al.*, "Advanced characterization technique for mechanochemically synthesized materials: neutron total scattering analysis," *J. Mater. Sci.*, vol. 53, no. 19, pp. 13400–13410, 2018, doi: 10.1007/s10853-018-2212-9.

[70] T. Subramani and A. Navrotsky, "Energetics of Formation and Disordering in Rare Earth Weberite RE3TaO7 Materials," *Inorg. Chem.*, vol. 58, no. 23, pp. 16126–16133, 2019, doi: 10.1021/acs.inorgchem.9b02675.

[71] T. Tanaka, N. Ishizawa, M. Yoshimura, F. Marumo, and H. Oyanagi, "Exafs analysis and reinvestigation of the structure of a defect-fluorite-type compound, y3tao7," *J. Solid State Chem.*, vol. 114, no. 1, pp. 79–87, 1995, doi: 10.1006/jssc.1995.1012.

[72] W. C. Hamilton, "Significance tests on the crystallographic R factor," *Acta Crystallogr.*, vol. 18, no. 3, pp. 502–510, May 1965, doi: 10.1107/S0365110X65001081.

[73] J. F. Gómez-García, L. Bucio, and G. Tavizon, "Dy3TaO7 A stoichiometric spin glass and the effect of disorder via chemical substitution in the Dy3−xYxTaO7 ($0 \leq x \leq 3$) solid solution," *J. Solid State Chem.*, vol. 257, no. 2017, pp. 49–57, 2018, doi: 10.1016/j.jssc.2017.09.026.

[74] J. F. Gomez-Garcia, R. Escudero, and G. Tavizon, "Spin glass behavior in the Dy3-xY xTaO7 ($0 \leq x \leq 1$) system," *J. Solid State Chem.*, vol. 217, pp. 42–49, 2014, doi: 10.1016/j.jssc.2014.04.029.

[75] R. Abe, M. Higashi, Z. Zou, K. Sayama, Y. Abe, and H. Arakawa, "Photocatalytic water splitting into H2 and O2 over R3TaO7 and R3NbO7 (R = Y, Yb, Gd, La): Effect of crystal structure on photocatalytic activity," *J. Phys. Chem. B*, vol. 108, no. 3, pp. 811–814, 2004, doi: 10.1021/jp036300v.

[76] F. Wu, P. Wu, R. Zong, and J. Feng, "Investigation on thermo-physical and mechanical properties of Dy3(Ta1-xNbx)O7 ceramics with order-disorder transition," *Ceram. Int.*, vol. 45, no. 12, pp. 15705–15710, 2019, doi: 10.1016/j.ceramint.2019.04.207.

[77] F. Wu, P. Wu, L. Chen, and J. Feng, "Structure and thermal properties of Al 2 O 3 -doped

Gd 3 TaO 7 as potential thermal barrier coating," *J. Eur. Ceram. Soc.*, vol. 39, no. 6, pp. 2210–2214, 2019, doi: 10.1016/j.jeurceramsoc.2019.02.002.

[78] J. F. Vente, R. B. Helmholdt, and D. J. W. Ijdo, "The structure and magnetic properties of Pr3MO7 with M = Nb, Ta, and Sb," *Journal of Solid State Chemistry*, vol. 108, no. 1. pp. 18–23, 1994. doi: 10.1006/jssc.1994.1003.

[79] H. P. Rooksby and E. A. D. White, "Rare-Earth Niobates and TantaIates of Defect Fluorite- and Weberite-Type Structures," *J. Am. Ceram. Soc.*, vol. 47, no. 2, pp. 94–96, 1964, doi: 10.1111/j.1151-2916.1964.tb15663.x.

[80] D. K. Nath, "Synthesis of Rare Earth Antimonate Pyrochlores and Cathodoluminescence of Europium(3+) in 3Gd2O3 Sb2O5," *Inorg. Chem.*, vol. 9, no. 12, pp. 2714–2718, 1970, doi: 10.1021/ic50094a019.

[81] R. P. H. Robinson K., Gibbs G. V., "Quadratic Elongation: A Quantitative Measure of Distortion in Coordination Polyhedra," *Science (80-.).*, vol. 172, p. 567, 1971.

[82] N. A. Spaldin, "Multiferroics: Past, present, and future," *MRS Bull.*, vol. 42, no. 5, pp. 385–389, 2017, doi: 10.1557/mrs.2017.86.

[83] K. Aizu, "Possible species of ferromagnetic, ferroelectric, and ferroelastic crystals," *Phys. Rev. B*, vol. 2, no. 3, pp. 754–772, 1970, doi: 10.1103/PhysRevB.2.754.

[84] R. B. Neder, F. Frey, and H. Schulz, "Diffraction theory for diffuse scattering by correlated microdomains in materials with several atoms per unit cell," *Acta Crystallogr. Sect. A*, vol. 46, no. 10, pp. 792–798, 1990, doi: 10.1107/S0108767390006602.

[85] C. K. Jorgensen, "Absorption Spectra and Chemical Bonding in Complexes," *Pergamon Press*, vol. 147, no. 360, pp. 310–312, 1962, doi: 10.1524/zpch.1963.36.3_4.251.

[86] G. Blasse, "Qualitative approach to the structural differences between some mixed metal oxides containing Sb5+, Nb5+ and Ta5+," *J. Inorg. Nucl. Chem.*, vol. 26, no. 7, pp. 1191–1199, 1964, doi: 10.1016/0022-1902(64)80199-8.

[87] E. C. O'Quinn *et al.*, "Inversion in Mg 1– x Ni x Al 2 O 4 Spinel: New Insight into Local Structure," *J. Am. Chem. Soc.*, vol. 139, no. 30, pp. 10395–10402, 2017, doi:

10.1021/jacs.7b04370.

[88] M. K. et al. Baldinozzi, G., Casillas-Trujillo, L., Patel, “Structural complexity of Y6BO12 fluorite-related ternary oxides.,” *MRS Adv.*, vol. 6, pp. 107–111, 2021.

[89] L. Cai and J. C. Nino, “Structure and dielectric properties of Ln3NbO7 (Ln = Nd, Gd, Dy, Er, Yb and Y),” *J. Eur. Ceram. Soc.*, vol. 27, no. 13–15, pp. 3971–3976, 2007, doi: 10.1016/j.jeurceramsoc.2007.02.077.

[90] H. Euchner, O. Clemens, and M. A. Reddy, “Unlocking the potential of weberite-type metal fluorides in electrochemical energy storage,” *npj Comput. Mater.*, vol. 5, no. 1, pp. 1–10, 2019, doi: 10.1038/s41524-019-0166-3.

[91] H. J. Rossell, “Fluorite-related phases Ln3MO7, Ln = Rare-earth, Y or Sc, M = Nb, Sb or Ta. III. Structure of the non-stoichiometric Y3TaO7 phase,” *J. Solid State Chem.*, vol. 27, no. 3, pp. 287–292, 1979, doi: 10.1016/0022-4596(79)90169-5.

[92] R. C. Ewing, “Nuclear waste forms for actinides,” *Proc. Natl. Acad. Sci.*, vol. 96, no. 7, pp. 3432–3439, 1999, doi: 10.1073/pnas.96.7.3432.

[93] W. J. Weber, J. W. Wald, and H. Matzke, “Self-radiation damage in Gd2Ti2O7,” *Mater. Lett.*, vol. 3, no. 4, pp. 173–180, 1985, doi: 10.1016/0167-577X(85)90154-5.

[94] S. X. Wang, B. D. Begg, L. M. Wang, R. C. Ewing, W. J. Weber, and K. V. Govidan Kutty, “Radiation stability of gadolinium zirconate: A waste form for plutonium disposition,” *J. Mater. Res.*, vol. 14, no. 12, pp. 4470–4473, 1999, doi: 10.1557/JMR.1999.0606.

[95] R. C. Ewing, W. J. Weber, and J. Lian, “Nuclear waste disposal—pyrochlore (A2B2O7): Nuclear waste form for the immobilization of plutonium and ‘minor’ actinides,” *J. Appl. Phys.*, vol. 95, no. 11, pp. 5949–5971, May 2004, doi: 10.1063/1.1707213.

[96] M. Lang *et al.*, “Single-ion tracks in Gd2 Zr2-x Tix O7 pyrochlores irradiated with swift heavy ions,” *Phys. Rev. B - Condens. Matter Mater. Phys.*, vol. 79, no. 22, pp. 1–9, 2009, doi: 10.1103/PhysRevB.79.224105.

[97] M. A. Subramanian, G. Aravamudan, and G. V. Subba Rao, “Oxide pyrochlores - A review,” *Prog. Solid State Chem.*, vol. 15, no. 2, pp. 55–143, 1983, doi: 10.1016/0079-

6786(83)90001-8.

[98] W. A. Groen and D. J. W. IJdo, “Distrontium diantimonate(V). A Rietveld refinement of neutron powder diffraction data,” *Acta Crystallogr. Sect. C Cryst. Struct. Commun.*, vol. 44, no. 5, pp. 782–784, 1988, doi: 10.1107/s0108270188000204.

[99] M. Lang, F. X. Zhang, R. C. Ewing, J. Lian, C. Trautmann, and Z. Wang, “Structural modifications of Gd2Zr2- xTi xO7 pyrochlore induced by swift heavy ions: Disordering and amorphization,” *J. Mater. Res.*, vol. 24, no. 04, pp. 1322–1334, 2009, doi: 10.1557/jmr.2009.0151.

[100] J. F. Gibbons, “Ion implantation in semiconductors—Part II: Damage production and annealing,” *Proc. IEEE*, vol. 60, no. 9, pp. 1062–1096, 1972, doi: 10.1109/PROC.1972.8854.

[101] J. Zhang, M. Toulemonde, M. Lang, J. M. Costantini, S. Della-Negra, and R. C. Ewing, “C60 and U ion irradiation of Gd2TixZr2-xO7 pyrochlore,” *J. Mater. Res.*, vol. 30, no. 16, pp. 2456–2466, 2015, doi: 10.1557/jmr.2015.230.

[102] J. Zhang, M. Lang, R. C. Ewing, R. Devanathan, W. J. Weber, and M. Toulemonde, “Nanoscale phase transitions under extreme conditions within an ion track,” *J. Mater. Res.*, vol. 25, no. 7, pp. 1344–1351, 2010, doi: 10.1557/jmr.2010.0180.

[103] J. Wang, M. Lang, R. C. Ewing, and U. Becker, “Multi-scale simulation of structural heterogeneity of swift-heavy ion tracks in complex oxides,” *J. Phys. Condens. Matter*, vol. 25, no. 13, 2013, doi: 10.1088/0953-8984/25/13/135001.

[104] M. Toulemonde, E. Paumier, and C. Dufour, “Thermal spike model in the electronic stopping power regime,” *Radiat. Eff. Defects Solids*, vol. 126, no. 1–4, pp. 201–206, Mar. 1993, doi: 10.1080/10420159308219709.

[105] G. Sattonnay, C. Grygiel, I. Monnet, C. Legros, M. Herbst-Ghysel, and L. Thomé, “Phenomenological model for the formation of heterogeneous tracks in pyrochlores irradiated with swift heavy ions,” *Acta Mater.*, vol. 60, no. 1, pp. 22–34, 2012, doi: 10.1016/j.actamat.2011.09.017.

[106] C. L. Tracy, M. Lang, F. Zhang, C. Trautmann, and R. C. Ewing, “Phase transformations in

Ln2 O3 materials irradiated with swift heavy ions," *Phys. Rev. B - Condens. Matter Mater. Phys.*, vol. 92, no. 17, pp. 1–14, 2015, doi: 10.1103/PhysRevB.92.174101.

[107] M. Lang *et al.*, "Nanoscale manipulation of the properties of solids at high pressure with relativistic heavy ions," *Nat. Mater.*, vol. 8, no. 10, pp. 793–797, 2009, doi: 10.1038/nmat2528.

[108] S. C. Bart, "What is the 'Lanthanide Contraction'?," *Inorg. Chem.*, vol. 62, no. 9, pp. 3713–3714, 2023, doi: 10.1021/acs.inorgchem.3c00440.

[109] M. Zinkevich, "Thermodynamics of rare earth sesquioxides," *Prog. Mater. Sci.*, vol. 52, no. 4, pp. 597–647, 2007, doi: 10.1016/j.pmatsci.2006.09.002.

[110] A. P. Solomon, C. L. Tracy, E. C. O'Quinn, D. Severin, and M. K. Lang, "Transformations to amorphous and X-type phases in swift heavy ion-irradiated Ln2O3 and Mn2O3," *J. Appl. Phys.*, vol. 129, no. 22, 2021, doi: 10.1063/5.0050028.

[111] A. B. Cusick *et al.*, "Amorphization of Ta2O5 under swift heavy ion irradiation," *Nucl. Instruments Methods Phys. Res. Sect. B Beam Interact. with Mater. Atoms*, vol. 407, pp. 25–33, 2017, doi: 10.1016/j.nimb.2017.05.036.

[112] A. B. Cusick, M. Lang, F. Zhang, J. Zhang, C. Trautmann, and R. C. Ewing, "Swift Heavy Ion-Induced Decomposition and Phase Transformation in Nanocrystalline SnO2," *MRS Online Proc. Libr.*, vol. 1715, no. 1, pp. 13–20, 2014, doi: 10.1557/opl.2014.733.

[113] K. E. Sickafus, "Radiation Tolerance of Complex Oxides," *Science (80-.).*, vol. 289, no. 5480, pp. 748–751, 2000, doi: 10.1126/science.289.5480.748.

[114] M. Patel, J. Aguiar, K. Sickafus, and G. Baldinozzi, "Structure and radiation response of anion excess bixbyite Formula Presented," *Phys. Rev. Mater.*, vol. 6, no. 1, p. 13610, 2022, doi: 10.1103/PhysRevMaterials.6.013610.

[115] L. M. Daniels, R. J. Kashtiban, D. Kepaptsoglou, Q. M. Ramasse, J. Sloan, and R. I. Walton, "Local A-Site Layering in Rare-Earth Orthochromite Perovskites by Solution Synthesis," *Chem. - A Eur. J.*, vol. 22, no. 51, pp. 18362–18367, 2016, doi: 10.1002/chem.201604766.

[116] T. Karthik, T. D. Rao, A. Srinivas, and S. Asthana, "A-Site Cation disorder and Size

variance effects on the physical properties of multiferroic Bi0.9RE0.1FeO3 Ceramics (RE =Gd3+,Tb3+,Dy3+),” pp. 1–12, 2012, [Online]. Available: http://arxiv.org/abs/1206.5606

[117] L. M. Rodŕiguez-Martínez and J. P. Attfield, “Structural effects of cation size variance in magnetoresistive manganese oxide perovskites,” *Chem. Mater.*, vol. 11, no. 6, pp. 1504–1509, 1999, doi: 10.1021/cm980759y.

[118] C. L. Tracy, M. Lang, J. Zhang, F. Zhang, Z. Wang, and R. C. Ewing, “Structural response of A 2TiO 5 (A = La, Nd, Sm, Gd) to swift heavy ion irradiation,” *Acta Mater.*, vol. 60, no. 11, pp. 4477–4486, 2012, doi: 10.1016/j.actamat.2012.05.005.

[119] J. Lian *et al.*, “Radiation-Induced amorphization of rare-Earth titanate pyrochlores,” *Phys. Rev. B - Condens. Matter Mater. Phys.*, vol. 68, no. 13, pp. 1–9, 2003, doi: 10.1103/PhysRevB.68.134107.

[120] A. Meftah *et al.*, “Swift heavy ions in magnetic insulators: A damage-cross-section velocity effect,” *Phys. Rev. B*, vol. 48, no. 2, pp. 920–925, Jul. 1993, doi: 10.1103/PhysRevB.48.920.

[121] W. Wesch, J. Rensberg, T. Bierschenk, B. Afra, P. Kluth, and E. Wendler, “Determination of track radii and relation to the electronic energy density deposited in swift heavy ion irradiated LiNbO3,” *Nucl. Instruments Methods Phys. Res. Sect. B Beam Interact. with Mater. Atoms*, vol. 485, no. August, pp. 50–56, 2020, doi: 10.1016/j.nimb.2020.10.015.

[122] H. M. Naguib and R. Kelly, “Criteria for bombardment-induced structural changes in non-metallic solids,” *Radiat. Eff.*, vol. 25, no. 1, pp. 1–12, Jan. 1975, doi: 10.1080/00337577508242047.

[123] G. Pilania *et al.*, “Using Machine Learning to Identify Factors That Govern Amorphization of Irradiated Pyrochlores,” *Chem. Mater.*, vol. 29, no. 6, pp. 2574–2583, 2017, doi: 10.1021/acs.chemmater.6b04666.

[124] V. M. Goldschmidt, “The laws of crystal chemistry,” *Naturwissenschaften*, vol. 14, no. 21, pp. 477–485, 1926.

[125] M. Lang, E. O’Quinn, J. Neuefeind, and C. Trautmann, “Characterization of Radiation Effects and Ion Tracks with Spallation Neutron Probes,” *Nucl. Phys. News*, vol. 30, no. 1, pp. 16–19, 2020, doi: 10.1080/10619127.2019.1676120.

[126] C. K. Chung *et al.*, “Thermodynamic and structural evolution of Dy2Ti2O7 pyrochlore after swift heavy ion irradiation,” *Acta Mater.*, vol. 145, pp. 227–234, 2018, doi: 10.1016/j.actamat.2017.12.044.

[127] C. K. Chung *et al.*, “Thermodynamic and structural evolution of mechanically milled and swift heavy ion irradiated Er2Ti2O7 pyrochlore,” *Acta Mater.*, vol. 181, pp. 309–317, 2019, doi: 10.1016/j.actamat.2019.09.022.

[128] L. Pauling and G. W. Wheland, “The Nature of the Chemical Bond. V,” *J. Chem. Phys.*, vol. 2, no. 8, p. 482, 1934, doi: 10.1063/1.1749514.

[129] V. I. Malkovsky, S. V. Yudintsev, M. I. Ojovan, and V. A. Petrov, “The Influence of Radiation on Confinement Properties of Nuclear Waste Glasses,” *Sci. Technol. Nucl. Install.*, vol. 2020, 2020, doi: 10.1155/2020/8875723.

[130] I. T. Todorov, W. Smith, K. Trachenko, and M. T. Dove, “DL_POLY_3: New dimensions in molecular dynamics simulations via massive parallelism,” *J. Mater. Chem.*, vol. 16, no. 20, pp. 1911–1918, 2006, doi: 10.1039/b517931a.

[131] L. Deng and J. Du, “Development of boron oxide potentials for computer simulations of multicomponent oxide glasses,” *J. Am. Ceram. Soc.*, vol. 102, no. 5, pp. 2482–2505, 2019, doi: 10.1111/jace.16082.

[132] M. Wang, N. M. A. Krishnan, B. Wang, M. M. Smedskjaer, and J. C. Mauro, “A new transferable interatomic potential for molecular dynamics simulations of borosilicate glasses,” *J. Non. Cryst. Solids*, vol. 498, no. April, pp. 294–304, 2018, doi: 10.1016/j.jnoncrysol.2018.04.063.

[133] D. A. Keen, “A comparison of various commonly used correlation functions for describing total scattering,” *J. Appl. Crystallogr.*, vol. 34, no. 2, pp. 172–177, 2001, doi: 10.1107/S0021889800019993.

[134] W. J. Dell, P. J. Bray, and S. Z. Xiao, “11B NMR studies and structural modeling of Na2OB2O3SiO2 glasses of high soda content,” *J. Non. Cryst. Solids*, vol. 58, no. 1, pp. 1–16, 1983, doi: 10.1016/0022-3093(83)90097-2.

[135] X. Lu, L. Deng, J. Du, and J. D. Vienna, “Predicting boron coordination in multicomponent

borate and borosilicate glasses using analytical models and machine learning," *J. Non. Cryst. Solids*, vol. 553, no. August 2020, p. 120490, 2021, doi: 10.1016/j.jnoncrysol.2020.120490.

Appendix: The structure of aluminaborosilicate glasses for nuclear waste encapsulation characterized by neutron diffraction, reverse Monte Carlo methods and molecular dynamics

This appendix contains text presented in the unpublished manuscript "The structure of aluminaborosilicate glasses for nuclear waste encapsulation characterized by neutron diffraction, reverse Monte Carlo methods and molecular dynamics" by Oliver A. Dicks, Igor Gussev, Xiaonan Lu, Maik Lang, Kostya Trachenko. Parts of this manuscript are published in the following project report: Maik Lang, Alexandra Navrotsky, Joseph Ryan, Jarrod Crum, Igor Gussev, *et al.*, "*Project 17-13125: The Thermodynamics of Crystallization and Phase-Separation in Melt-Derived Nuclear Waste Forms (Technical report),* pp. 1–161, (2021).

For this unpublished work: M.L. conceived the experiment, X.L. provided the samples, I.G. performed the neutron total scattering experiments and RMC modeling, O.D. and K.T. performed MD modeling and RMC boxes assessment, O.D. and I.G. wrote the manuscript with input from all the authors.

This research was performed using funding received from the DOE Office of Nuclear Energy's Nuclear Energy University Program under US-DOE, contract DE-NE0008694. The research at ORNL's Spallation Neutron Source was sponsored by the Scientific User Facilities Division, Office of Basic Energy Sciences, U.S. Department of Energy. The NMR measurements were supported by the Center for Performance and Design of Nuclear Waste Forms and Containers, an Energy Frontier Research Center funded by the U.S. Department of Energy, Office of Science, Basic Energy Sciences (BES) under Award # DE-SC0016584. Computational resources were provided by UNT's High Performance Computing Services, a division of the University

Information Technology with additional support from UNT Office of Research and Economic Development. NMR measurements were performed using facilities at the Environmental Molecular Science Laboratory (EMSL, grid.436923.9), a DOE Office of Science User Facility sponsored by the Office of Biological and Environmental Research at Pacific Northwest National Laboratory (PNNL). I.M.G. also acknowledges support from the U.S. Department of Energy, Office of Science, Office of Workforce Development for Teachers and Scientists, Office of Science Graduate Student Research (SCGSR) program. The SCGSR program is administered by the Oak Ridge Institute for Science and Education (ORISE) for the DOE. ORISE is managed by ORAU under contract number DE-SC0014664.

1. Introduction

The long-term safe storage of highly radioactive nuclear waste is a long standing societal and economic issue. It requires the development of a radiation resistant encapsulation matrix that can remain leach resistant for over 10’000 years. Aluminoborosilicate (ABS) glasses are a candidate for this encapsulation matrix, with many countries already using ABS glasses to store high level waste (HLW) [129]. However, due to the constraint that experiments cannot test the effects of radiation damage from nuclear isotopes over a time period longer than the extent of human civilization, very accurate models and experiments must be developed to simulate and recreate the effects of varying levels of radiation damage on the material’s properties. A crucial foundation for these models is understanding the atomistic, micro- and macroscopic structure of these glasses. To this endeavor we have applied advanced experimental and computational techniques to accurately characterize the structural properties of series’ of aluminoborosilicate glasses. In this paper neutron diffraction and nuclear magnetic resonance (NMR) experiments have been analyzed using a

combination of molecular dynamics (MD) simulations and Reverse Monte Carlo (RMC) methods to generate atomistic models of glasses inaccessible to any single technique.

2. Methodology

2.1 Glass fabrication

For this study the baseline glass composition, given in **Table A.1**, was based on the CSLNTM-C-1.5 composition which was previously developed and characterized for a hypnotical high-level waste stream generated by aqueous reprocessing. This composition was simplified by maintaining the original ratios of the five main glass components (Al_2O_3, B_2O_3, CaO, Na_2O and SiO_2), excluding lanthanides, MoO_3, ZrO_2, and others, and representing all alkalis by Na_2O and all alkaline earths by CaO. From this base composition, a system of compositions was defined such that the concentrations of Na_2O and Al_2O_3 were varied at the expense of all remaining components, modifying the number of non-bridging oxygens per tetrahedra (NBO-t) in the glass. The ratio of $Al_2O_3/(Na_2O+CaO)$ was varied from 0.25 to 0.79, and the fraction of non-bridging oxygen per tetrahedra is calculated to vary from 52 % (high Na_2O) down to 0 % (high Al_2O_3). The variations of Na_2O and Al_2O_3 are broad enough that they are expected to impact the glass structure and thermodynamic properties. All glass compositions were synthesized at the Pacific Northwest National Laboratory using Boron-11 enriched B_2O_3 to minimize absorption of neutrons during structural investigations. Each glass composition was batched from oxides, carbonates, and boric acid, and weighed out to within ± 0.02 grams. The chemicals were then combined together and milled for 4 minutes inside an agate milling chamber using an Angstrom shaker mill. The milled batch were placed into a Pt-10% Rh crucible, covered with a lid, and melted for 1 h at the respective melting temperatures. The liquids were subsequently poured and quench onto a stainless-steel plate

Table A.1: The expected composition of each glass compared to the simplified CSLNTM-C-1.5 (C-1.5) glass

Component	C-1.5	Base	Na-1	Na-2	Na-3	Al-1	Al-2	Al-3
Na_2O	0.18	0.18	0.13	0.23	0.255	0.1897	0.1703	0.1606
CaO	0.07	0.06	0.0637	0.0563	0.0545	0.0632	0.0568	0.0535
Al_2O_3	0.06	0.07	0.0743	0.0657	0.0636	0.02	0.12	0.17
B_2O_3	0.09	0.09	0.0955	0.0845	0.0818	0.0948	0.0852	0.0803
SiO_2	0.6	0.6	0.6366	0.5634	0.5451	0.6323	0.5677	0.5355

and broken into small pieces to minimize any bulk inhomogeneity. The glass samples were subsequently re-melted for an additional 1 h and quenched on the stainless-steel plate. The stress caused by quenching was annealed out prior to structural and thermal analysis measurements by placing pieces of quenched glass into a muffle furnace where the samples were ramp heated at 2 °C/min from room temperature up to either 530 °C (Na-series) or 580 °C (Al-series), held for a 1 hour soak at temperature, and ramp cooled at 1 °C/min back down to room temperature. Following annealing, the samples were examined under cross-polarized light to observe the removal of strain.

2.2 Neutron total scattering

All glass samples were measured at ambient temperature using the Nanoscale-Ordered Materials Diffractometer (NOMAD) at the Spallation Neutron Source (SNS) at Oak Ridge National Laboratory (ORNL). The neutron flux was on the order of 1×10^8 neutrons/cm^{2}s with a neutron wavelength band of 0.1-3Å, covering a wide range of momentum transfers suitable for high-resolution pair distribution function analysis. Prior to measuring the samples on NOMAD, several diamond calibration reference runs were performed in conditions identical to the measurement setup to calibrate the conversion of time-of-flight to momentum transfer for each individual pixel of the detector. The as-collected scattering intensity of samples was normalized using the scattering intensity of a solid vanadium rod to correctly scale the as-collected structure factor S(Q). An "empty position" on the shifter sample holder was measured first without a sample in the neutron beam to account for the background associated with the instrument itself. An empty sample container (quartz capillary) was measured on the same shifter prior to measuring the sample in order to perform the adequate sample background subtraction. The sample container was a 3 mm diameter quartz capillary, with wall thickness of 0.1 mm. Glass powders were sieved to ensure

uniform particle distribution in the neutron beam. Each glass composition was measured for approximately 100 minutes to obtain the total scattering structure functions, S(Q). The pair distribution functions, g(r), were obtained using a Fourier transform of S(Q). The minimum Q-value was chosen to be 0.32 $Å^{-1}$, and pair distribution functions (PDFs) were generated with maximum Q-values of 42-25 $Å^{-1}$ using simple Fourier transform method using STOG subroutine available within RMC package with the scale factor manually adjusted by the user.

2.3 Reverse Monte Carlo (RMC) modeling

The RMCprofile software package version 6.7.8. has been used to structurally relax the glass models to better fit the experimental neutron total scattering data. The initial box of atom coordinates was taken from the REVCON files generated by the MD procedure described below, with comparisons also being made to samples run from initially randomized atomic configurations. Both S(Q) and g(r) neutron total scattering data were fitted simultaneously with identical data weights in the RMC software. The cation-oxygen window constraints were defined individually for the B-O, Si-O and Al-O cation-oxygen pairs. Remaining Na-O, Ca-O and O-O atom pairs, as well as the rest of cation-cation were constrained by a minimum interatomic distance of 2.0 Å. The RMC simulations were run from an identical starting configuration for a set of run times (varying from 1 minute - 5 hours) to determine the configuration that provides the most adequate fit for the experimental data and provides a reasonable configuration environment. Resultant RMC boxes were further converted back into REVCON format and then tested using user-written glass network analysis codes.

2.4 Molecular dynamics (MD) modeling

In order to create atomistic structural models of Al- and Na-rich glasses, model systems have been generated using a molecular dynamics (MD) melt-quench method. These simulations were performed using the massively parallelized MD code DL_POLY2 [130] and a recently developed composition dependent potential developed by Deng and Du [131]. This potential has been specifically parameterized to recreate the correct boron coordination distribution in borosilicate glasses. In initial simulations of this glass series the potential developed by Wang et al. [132] was used, but despite structures from this potential [132] fitting the structure factors measured from neutron diffraction, it failed to recreate the boron coordination distribution measured experimentally or predicted using the Bernstein equation. A melt-quench method was used to generate the glass structures. A box of 5,000 atoms, corresponding to the chemical composition of each glass, was randomized and then melted at 3,000 K until the average root mean square displacement of the atoms was on the order of half the cell length parameter. The liquid structure was then cooled at a rate of 10 K/ps to 300 K with the nvt ensemble. The cell was then relaxed at 300 K and zero pressure using the npt ensemble for 100 ps. Final statistics were then taken at constant volume using the nvt ensemble for 100 ps. The Deng and Du potential [131] was used for all calculations. The B-coordination number used to calculate the *AB−O3* Buckingham potential parameter was taken from the results of the NMR experiments rather than from the Bernstein equation as used in the qualitative characterization paper.

3. Results

3.1 Neutron data analysis

The processed neutron S(Q) data as well as respective g(r) data can be seen in Figure A.1. All S(Q) structure factors share the same general shape with 4 separate broad features before 9 $Å^{-1}$, indicating that all glass compositions have similar overall densities. The g(r) data has been processed from S(Q) data with very high Q-values between 42-45$Å^{-1}$, but the resolution of the real space data proves to be superb compared to previous studies, allowing more precise determination of the real space peak positions. The use of high Q-values is necessary to obtain this level of resolution; however, it does lead to a small fraction of Fourier noise in the form of sinusoidal-type oscillations. The Base glass sample provides the least amount of noise, making it the most attractive dataset to perform initial analysis on. Although some Fourier noise is present in the region above 3Å in g(r) data, its contribution to the data is minimal as there are no significant correlations beyond 3 Å. Similarly, the intensity of the first-neighbor peaks is much more significant than the amplitude of the noise, which makes the much-improved resolution from including high Q-values a good trade-off. Here g(r) is defined in the formalism described by Keen [133]. We can easily observe the flat g(r) contribution before the r-cutoff value of approximately 1.2Å for all glasses. There should also be no real space peak contributions below the ’zero’ value if there are no negative scatterers. However, the Al-3 sample demonstrates a significant negative ’peak’ around 1.7Å, right at the edge of the first B-O cumulative peak. This observation indicates that this particular sample was most likely prepared with some fraction of natural boron oxide, which is a disadvantage in this case. This leads to an observable negative correlation in real space data, which makes it harder to estimate where the ’zero’ is in the sample by adjusting the scale factor and also leads to the degradation of as-collected neutron data since natural boron is a good

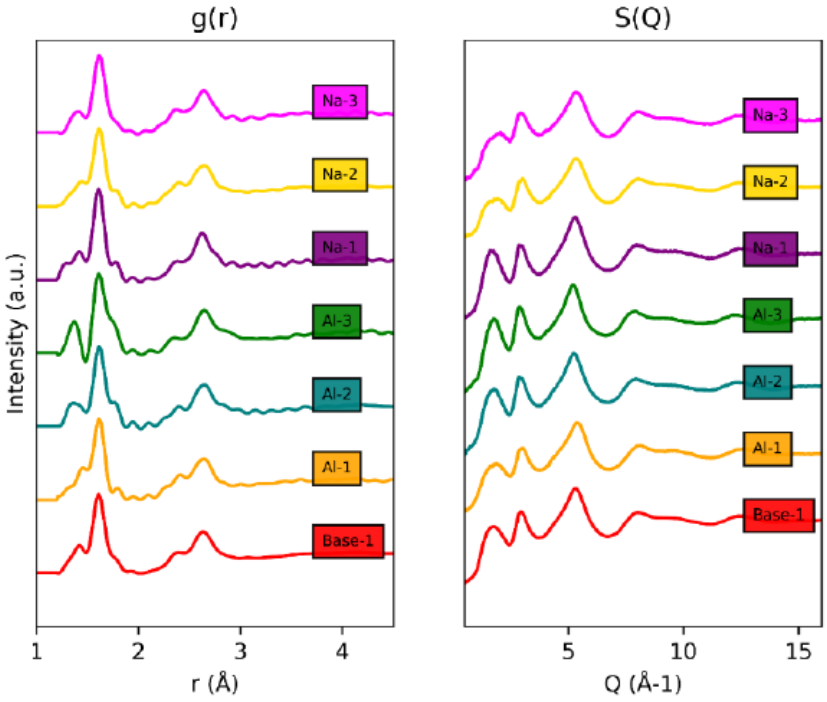

Figure A.1: Pair distribution functions g(r) and structure functions S(Q) of the entire glass series processed from as-collected neutron total scattering data.

neutron observer. Despite that, the data is perfectly usable, and Al-3 sample is adequately comparable to the rest of the glass series.

3.2 MD generated structures and improvements in prediction of network structure

In order to accurately model the structure of nuclear waste glasses the connectivity and topology of the glass network must be correctly recreated. Otherwise, if the overall topology of the glass is incorrect, RMC alone will struggle to recreate the correct structure from the neutron data. It also has important consequences when it comes to the diffusion of ions, such as radioactive waste elements, within the glass, and its resilience to radiation damage. A key part of modelling the connectivity is ensuring that the ratio of 3- to 4- coordinated boron ions ([3]B to [4]B) generated in the MD melt-quench model represents that measured experimentally using NMR. In **Table A.2** it can be seen that the Deng et al. [131] potential we used accurately reproduces the B coordination distribution as measured by NMR within 5 %. This is an improvement on the potential initially tested, where MD simulations incorrectly predicted the boron coordination in the Al series of glasses. It is worth noting that in this study the N4 values measured via NMR were used as an input to determine the A$_{B-O}$ parameter, rather than a prediction via the DBX model [134] as used in the original paper. **Table A.3** also shows the Bernstein model overestimates the N4 value for the Al-3 glass and underestimates it for the BASE glass. By using the NMR-measured values of N4, the potential is able to very accurately recreate the target B coordination ratio. In the absence of experimental data, accurate predictions of the N4 values are therefore essential to accurately modelling the structure. The DBX and Bernstein models still act as a good estimate for N4, and recently other analytical methods and machine learning techniques have been used to predict boron coordination ratios purely from glass stoichiometry [135], though it still proves difficult to

Table A.2: The fraction of 4-coordinated B ions (N4 in each glass generated using MD compared with the experimental NMR data.

	N4 (MD)	N4 (NMR)
Base	60.14	61
Na-1	54.11	49
Na-2	55.38	59
Na-3	57.94	55
Al-1	73.67	72
Al-2	33.46	36
Al-3	11.54	14

Table A.3: The fraction of 4-coordinated B ions (N4) in each glass calculated using the Bernstein model compared with the experimental NMR data and the B-O Buckingham potential AB-O parameter.

	N4 (Bernstein)	N4 (NMR)	AB-O
BASE	52	61	14304.31
Na-1	41	49	14625.27
Na-2	55	59	13790.51
Na-3	55	55	13557.5
Al-1	71	72	14619.67
Al-2	35	36	13572.92
Al-3	25	14	12931

accurately predict for the full range of glass compositions. Although the MD model performs well in reproducing the connectivity of the glass network, there are small inaccuracies in the prediction of some inter-atomic bond distances. This is due to the difficulty in fitting transferable 2-body potentials that can recreate all behaviors of multi-component glasses. However, minimizing this final error can be achieved by applying RMC to these MD melt-quench generated structures.

3.3 Shortcomings of pure RMC fitting of neutron data

RMC can be used to predict the structure of glasses measured by neutron diffraction. Conventionally a randomized box of atoms is used as the initial configuration of atoms. This can be seen by the lack of peaks in **Figure A.2** which is due to the lack of pair correlations in the initial box. As we will discuss below, this leads to issues in modelling complex multi-component amorphous systems. As shown in **Figure A.2**, RMC is able recreate some of the features of the experimental structure factor, S(Q) and radial distribution function, g(r). However, as well as being unable to reproduce the first peak at low Q in S(Q) and introducing a peak at approximately 2 Å in g(r), a large flaw in random seed RMC is its lack of chemical knowledge. This leads to the generation of unphysical structures that take little notice of the expected coordination numbers and bond lengths of the various elemental species. **Figure A.2** shows the RMC generated pair correlation functions ($g(r)$). Although it does correctly order the B-O, Si-O and Al-O first neighbour peaks distances, there are significant overlaps between the B-O and Si-O peaks which we know is not chemically correct. The RMC procedure also generates spurious peaks at low distances which are entirely unphysical. Even more problematical, the analysis of the atomic structure of the generated systems shows wide coordination number distributions for all the glass formers, with RMC predicting average cation-oxygen coordination numbers of less than 3 for B-

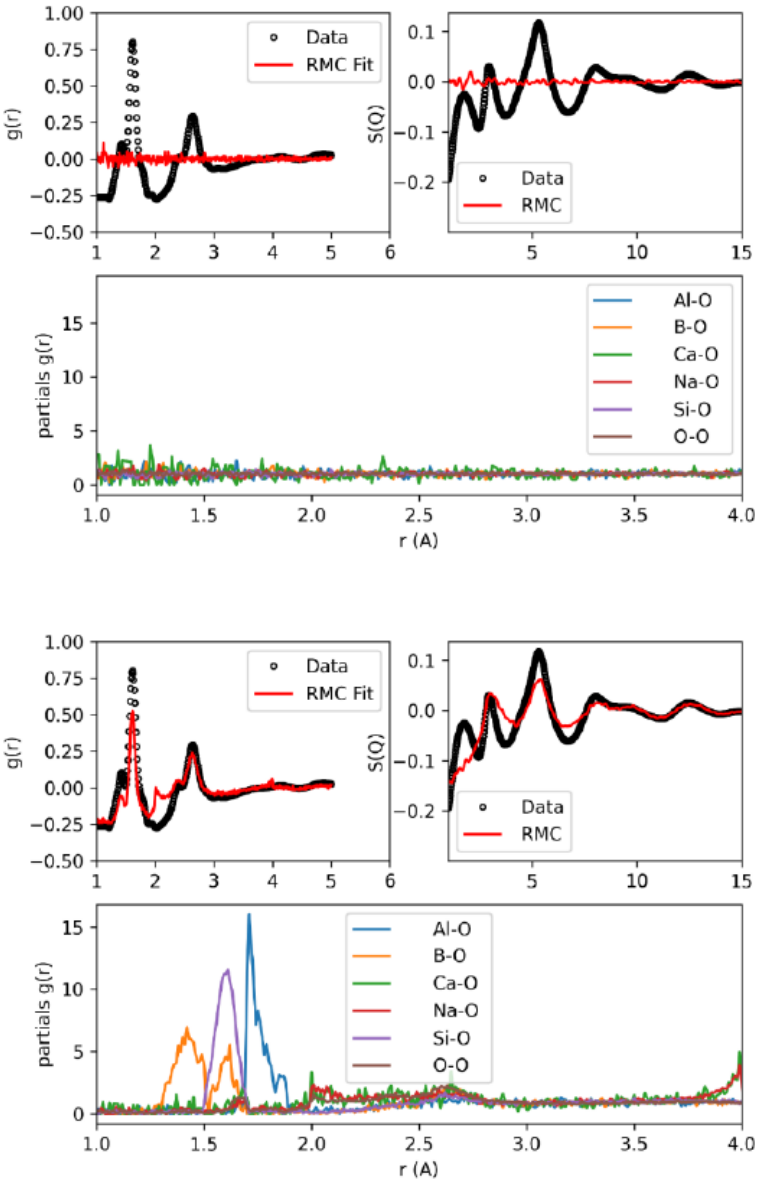

Figure A.2: (Top) initial and (bottom) RMC-relaxed pair distribution functions and structure factors, S(Q), of the base glass measured with neutron total scattering, and calculated using random seed RMC. The partial PDF distribution functions of the cations with oxygen resulting from the RMC procedure of the base glass are also shown.

O, Si-O and Al-O. This is contrary to the known behavior of Si and Al, which will almost entirely form oxygen tetrahedral units, and B, which forms trigonal and tetrahedral units with oxygen. This is likely a consequence of the relatively close values of the coherent neutron scattering lengths of the elements in the glass. This means that without external chemical intuition it is difficult for pure RMC approach to distinguish the correct pair distribution functions and to let alone generate the correct glass network connectivity.

3.4 RMC fits from MD seed structures

RMC performs much better at predicting atomistic configurations of multi-component glasses when using MD melt-quench structures to initialize the procedure, leading to much faster convergence of the total χ^2 error when fitting to S(Q) and g(r) (**Figure A.3**). This improvement to the fit can be seen in Figure A.4, where peak amplitudes, as well as positions, are accurately reproduced. For the RMC procedure to improve the fit to the neutron data from the MD structure whilst staying consistent with the NMR measurements, it must adjust the bond lengths of the glass formers without changing the local topology and coordination distributions. Analysis of the final structures of all 7 glasses predicted by MD-RMC (MD seeded RMC) show that the final N4 values vary by less than 0.5% from the initial MD structures, even after 5 hour runs (approximately a million accepted adjustments) of RMC. Although the coordination of the glass formers remains unchanged from that predicted by MD, there are large changes to the relative peak positions of O-O, Ca-O and Na-O, with RMC homogenizing the 3 quite distinct peaks predicted by MD (**Figure A.4**) into on peak. The combined use of MD and RMC leads to a great improvement in the fit of both the neutron and NMR experimental data and accurate predictions of the true glass structure over naive RMC using a random seed or pure MD modelling.

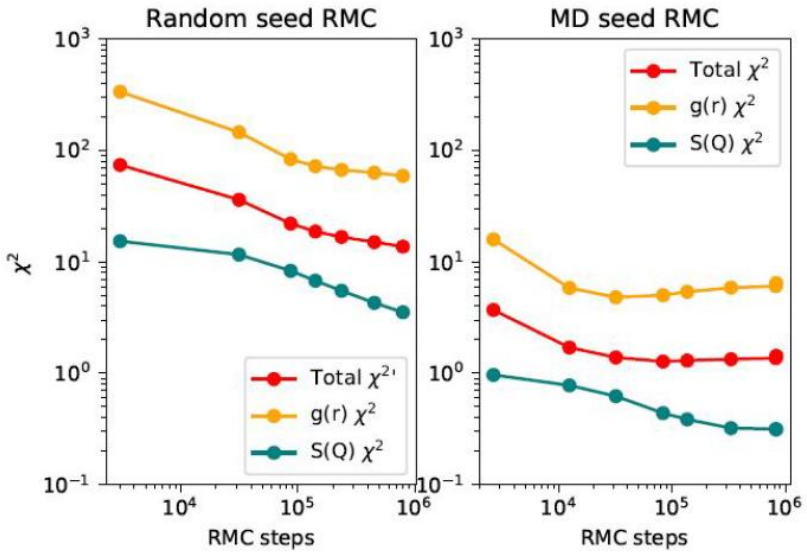

Figure A.3: A comparison of the χ^2 values vs number of accepted RMC steps for both the random seed and MD seed RMC refinement of the base glass structure.

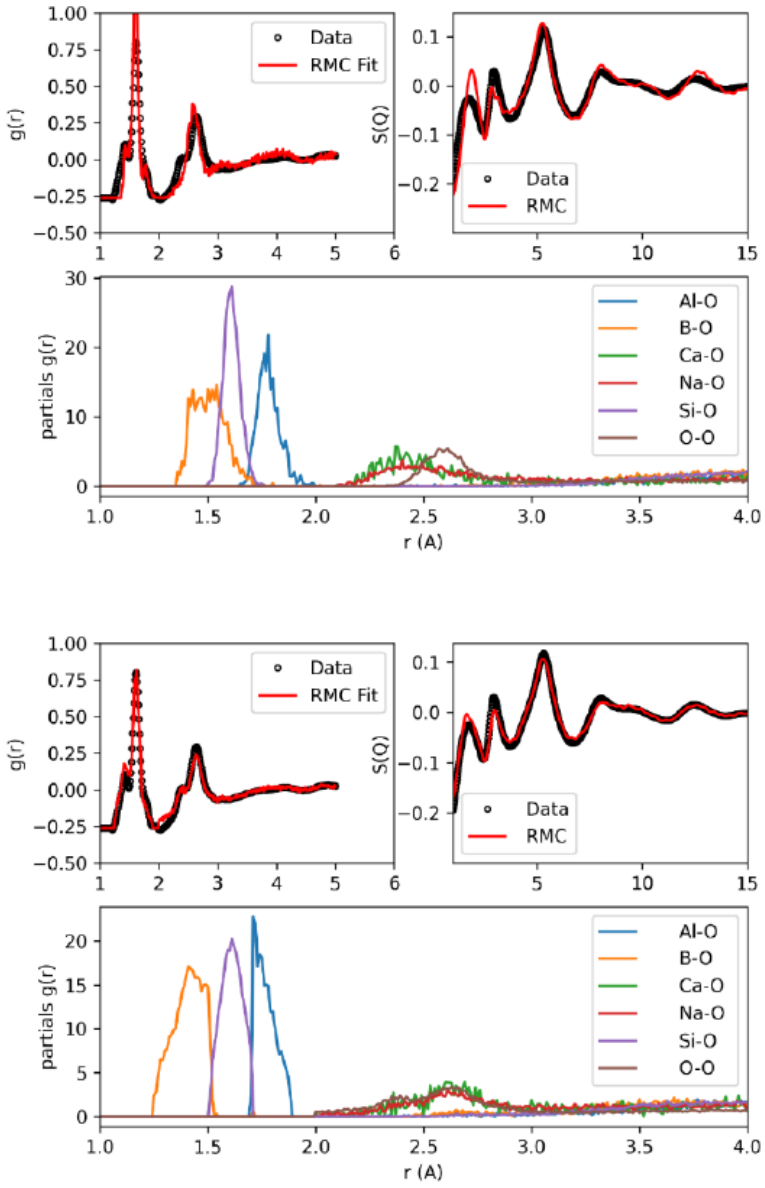

Figure A.4: (Top) an initial and (bottom) RMC-processed pair distribution functions g(r) and structure functions S(Q) of the Base glass measured using neutron total scattering and processed using improved MD potential box as the initial seed.

Vita

Igor Maximovich Gussev was born on November 4, 1994, in Almaty, Kazakhstan, where he grew up and attended high school (lyceum). He began undergraduate studies in 2013 at the Pellissippi State Community College in Knoxville, Tennessee, and later transferred to the Department of Nuclear Engineering at the University of Tennessee, Knoxville. He joined Dr. Lang's DISMAT research group in 2016 as an undergraduate research assistant. He graduated with a Bachelor of Science (B.S.) degree in Nuclear Engineering in May 2017. He later graduated with a Master of Science (M.S.) degree in Nuclear Engineering in August 2019. He participated in a joint Ph.D. (cotutelle) program at the Université Paris-Saclay, France, from April 2022 to May 2023 under the supervision of Dr. Baldinozzi. His undergraduate and graduate work has resulted in three first-author peer-reviewed journal articles and several other peer-reviewed journal articles as a co-author.